Abstract

Title of Dissertation: The Star Formation History of Low Surface Brightness Galaxies

Ji Hoon Kim, Doctor of Philosophy, 2007

Dissertation directed by: Professor Stacy S. McGaugh
Department of Astronomy

The star formation histories of low surface brightness galaxies are interesting but poorly constrained. These objects tend to be rather blue, contradicting the initial impression that they may simply be faded remnants of higher surface brightness galaxies whose star formation has finished. Other scenarios span a broad range: a young mean age, less dust, a lower metallicity, perhaps even a variable IMF. Distinguishing between these scenarios requires sufficient information to build stellar population synthesis models which, if not unique, at least exclude certain possibilities.

The total stellar mass (M_*) of a galaxy is most closely traced with the K_s-band light. Considering that this mass must form over a Hubble time, this in effect gives a measure of the time averaged star formation rate ($< \dot{M} > \approx M_* H_0$). H$\alpha$ emission traces the location of star formation, and also provides a fairly robust quantitative measure of its current rate ($\dot{M}_*$). We have obtained near-infrared broadband photometry and Hα photometry of a large sample of low surface brightness galaxies to measure the current and the time-averaged star formation rate in order to constrain their star formation histories.

The current star formation rates of LSBGs generally are higher than their past star formation rate, suggesting that the mean age of their stellar population is relatively young. This may stem from either a late epoch of formation or a sluggish

evolution. In the latter case, the star formation efficiency may be an increasing function of time, perhaps due in part to the slow build up of metals and dust. Nevertheless, star formation remains sporadic and is generally not well organized across the disk.

We find a strong correlation between the ratio of current to past average star formation rate and the gas mass fraction. Galaxies with large reservoirs of gas have relatively high current SFRs. There is a conspicuous absence of high gas mass fraction, low SFR galaxies, suggesting that the observed trend is not driven by bursts of star formation with short duty cycles.

The Star Formation History of Low Surface Brightness Galaxies

by

Ji Hoon Kim

Dissertation submitted to the Faculty of the Graduate School of the
University of Maryland at College Park in partial fulfillment
of the requirements for the degree of
Doctor of Philosophy
2007

Advisory Committee:

Professor Stacy S. McGaugh, chair
Professor Sylvain Veilleux
Professor Stuart Vogel
Professor Michael Regan
Professor Sung-Won Lee

To my parents and Chil Sook for having endured so long, and Ethan,

for being with us.

Acknowledgements

Looking back at my life as a graduate student, there have been many people who helped me grow as a Ph.D student and as a person. I am blessed to have so many of them and it is quite difficult to mention everyone. Still I will try to do so in order to reflect on past nine years.

First of all, I am so grateful to my advisor, Stacy McGaugh, for everything he provided for me. He has been an inspiring and patient advisor for a student who did not know how to think and write scientifically. His wide range of knowledge and intuition always awed me. In particular, his keen eyes as a physicist made me admire him. He also allowed me to learn at my own pace and to grow as an independent scientist. In such fast-paced times, I was lucky to have such an opportunity to become being able to perform independent research as a graduate student. More importantly, Stacy was fun to talk to, have a drink over with, and spend time at observatories with. I feel tremendously fortunate and honored to have Stacy as my mentor. As I said before, I am your man, through and through, Stacy.

I am also grateful to Stuart Vogel and Sylvain Veilleux who were on my thesis committee and have been patient with many things. Stuart was always kind and quick to offer help. Sylvain was precise and always offered good suggestions for improvement. I really appreciate both of them.

I am also grateful to have had many wonderful mentors at my alma mater, Seoul National University. In particular, Prof. Myung Gyoon Lee nurtured me with a great care while I was just an ignorant undergradute.

My nine years of graduate life left me many memories with graduate students who enjoyed and suffered together. First, I can not forego the "usual suspects". Without them, I probably would not survive through the rigors of the first year as a graduate student in the states. Particularly, Jocco, you were great and I have really missed your presence since you left. I should mention everyone's name from the Dirty Snowballs basketball crew, but it is easy to skip one. Therefore I will just thank all of them. Without balling with you, it should have been miserable. I have to thank Rahul Shetty and David Garofalo for pushing me get through these struggling times with them. I can not forget many late-night chats and cups of coffee I had with them.

Korean graduate students helped me survive this life as a graduate student in a foreign country. I enjoyed playing tennis and basketball with many KGSA members and am grateful for having them. However, no one made my life easier than Woong-Tae Kim and Jong-Won Kim. As a house mate, or as a mentor, they really helped me go through enduring times. I really wish them good luck wherever they will be.

And my family. I can not thank my parents too much. They always have been supportive and patient throughout my life. I would not have been where I am without their endless love and belief in me. Finally, my wife, Chilsook and our first son, Ethan, your presence just made me finish this thesis and move on to the next stage of my life. I can not appreciate you too much for being with me. I love you.

Contents

List of Tables

List of Figures

Chapter 1

Introduction

1.1 Emergence of Low Surface Brightness Galaxies

The study of low surface brightness galaxies (LSBGs) has been one of the fastest growing fields in astronomy during the past decade. Generally unknown as recently as three decades ago due to their intrinsic low surface brightness characteristic, LSBGs have many interesting physical properties, which potentially play important roles in revealing the formation and evolution of galaxies. Galaxies, which are diffuse objects, can be overwhelmed by the brightness of the night sky. In order for a galaxy to be detected, it must be above a certain percentage of the night sky brightness. And it still must have a large enough angular size lest it be confused with stars.

Although this censorship due to surface brightness was discussed by Zwicky (1957) and Arp (1965) first, it was Disney (1976) who investigated observational bias against galaxies with low surface brightness quantitatively. Before Disney (1976), the distribution of galaxy central surface brightness was believed to peak (Freeman 1970). The earliest work by Freeman (1970), using a sample of 36 disk galaxies,

showed that 28 of the 36 sample galaxies have approximately the same central surface brightness at $\mu_0 = 21.65 \pm 0.35$ mag arcsec^{-2} in B for their exponential surface brightness profiles given by

$$\mu(r) = \mu_0 + 1.086\frac{r}{\alpha} \tag{1.1}$$

where μ_0 is the central surface brightness and α is the scale length of the disk. This is known as "Freeman's law", which, if correct, would imply that galaxy formation processes must lead to a certain central mass surface density.

By deriving an equation for the apparent radius of galaxies in terms of the limiting and central surface brightnesses, Disney (1976) showed that the distribution of spiral galaxies is strongly peaked around the Freeman value while ellipticals show a similar, but broader peak around the Fish value (Fish 1964), considering that the limiting surface brightness must be close to 24 mag arcsec^{-2} in B for most plate material. With this analysis, Disney (1976) concluded that galaxies of all luminosities with the central surface brightness different from the Fish-Freeman values will be under-represented.

While Disney & Phillipps (1983) followed the reasoning of Disney (1976) by quantifying the volume sampled by galaxy surveys as a function of central surface brightness, Allen & Shu (1979) suggested that the selection effects involved were not likely to function as described by Disney (1976), and stated that the lack of large galaxies must be real. However, Allen & Shu (1979) still agreed that there is a bias against the faint end of the distribution of central surface brightness.

McGaugh et al. (1995a) were the first to confirm that the night sky selection effects are real and significant. They determined the space density of galaxies as a function of disk central surface brightness and found this distribution to be roughly flat toward the fainter side of the Freeman value with the assumption that central

surface brightness is independent of disk scale length. They also found a sharp decline in the distribution toward the brighter side of the Freeman value. McGaugh et al. (1995a) completely ruled out "Freeman's law" and stated that low surface brightness galaxies (those with central surface brightness fainter than 22 mag arcsec^{-2} in the B-band) comprise half the general galaxy population.

Many studies showed that LSBGs are really under-represented since Disney (1976). Notable early works, such as Schombert & Bothun (1988), Schombert et al. (1992), Impey et al. (1996), discovered and catalogued a large number of LSBGs.

1.2 Characteristics of Low Surface Brightness Galaxies

1.2.1 Colors and Star Forming Rates

Compared to their high surface brightness counterparts, little is known about the star formation properties of LSBGs. These galaxies are generally blue in the optical broad-bands (de Blok et al. 1995; McGaugh & Bothun 1994). Mean colors from these studies range from $U-B = -0.17\pm0.05$, $B-V = 0.49\pm0.04$, and $V-I = 0.89\pm0.04$ (McGaugh & Bothun 1994) to $U - B = -0.14 \pm 0.05$, $B - V = 0.52 \pm 0.05$, $B - R = 0.78 \pm 0.1$, and $V - I = 0.69 \pm 0.1$ (de Blok et al. 1995). By comparison, a high surface brightness galaxy (HSBG) sample from de Jong & van der Kruit (1994) has mean values of $B-V = 0.75\pm0.03$ and $V-R = 0.53\pm0.02$. However, it should be noted that giant LSB galaxies from Sprayberry et al. (1995) have indistinguishable mean values in both colors ($B - V = 0.73 \pm 0.05$, and $V - R = 0.50 \pm 0.04$) from HSBGs.

Several studies claimed that the bluer trend stays true in the near-infrared (NIR)

wavelength regime by combining NIR broad-band photometry with optical broad-band photometry. Tully et al. (1996) performed a photometry study on the Ursa Major cluster using B, R, I, and K'bands. They claimed that there exists bimodality of the central surface brightness distribution using their surface photometry result. For their LSBG subsample, the mean colors are $B - R = 0.96 \pm 0.5$ and $B - K' = 2.98 \pm 0.7$.

Another study with a large sample, Bell et al. (2000), has similar results. They tracked stellar populations of 26 LSBG sample galaxies using optical and NIR photometry of these galaxies, which were selected from three subsets of LSBGs; blue selected LSBGs, red selected LSBGs, and giant LSBGs. Their sample galaxies have mean colors of $B - V = 0.67 \pm 0.17$, $B - R = 1.00 \pm 0.26$, and $B - K' = 3.2 \pm 0.6$. With a smaller sample with 14 LSBGs, Bergvall et al. (1999) showed mean colors of $V - I = 0.65 \pm 0.1$ and $V - J = 1.1 \pm 0.1$ for their blue selected samples. Two $B - K'$ colors which they obtained are $B - K' = 2.0$ and 2.4.

Galaz et al. (2002) tried to obtain NIR photometry for the largest sample of LSBGs so far using a LSBG catalog from Impey et al. (1996), although there are no optical broad-band colors available. They divided their sample into two subsets, one of which is a high HI mass sample with log $(M_{HI}/M_{\odot}) > 9.5$ and the other is a low HI mass sample with log $(M_{HI}/M_{\odot}) < 9$. Mean $J - K'$ color values for these subsets are $J - K' = 0.84 \pm 0.19$ for the high HI mass sample and $J - K' = 0.62 \pm 0.17$ for the low HI mass sample.

There have not been many studies which try to measure star formation rates (SFRs) of LSBGs using star formation indicators, such as Hα photometry, ultraviolet photometry and far-infrared photometry. However, since the emission equivalent widths of HII regions in LSBGs are lower than those in HSBGs (McGaugh 1994; cf. Phillipps & Disney 1985) and these LSBGs have fewer HII regions than HSBGs

(McGaugh et al. 1995a), the average SFRs were known to be lower than those of HSBGs by at least an order of magnitude (Bothun et al. 1997).

Since then, a couple of studies have shown that LSBGs truly have very low star formation rates ($\sim 0.1 M_{\odot}$ per year). While mainly concentrating on dwarf galaxies, van Zee (2001) has several LSBGs in her sample. These LSBGs have SFRs lower than $0.1 M_{\odot}$ per year. Recently, O'Neil et al. (2007a) measured SFRs for 15 large LSBGs and found that they also have lower SFRs than HSBGs with similar sizes. The average value is 1.91 $M_{\odot}$ per year for these LSBGs with mean $B-R = 1.1 \pm 0.4$.

1.2.2 Metallicity, Gas and Dust

LSBGs are generally low metallicity systems. Their HII region metallicity is about the same or lower than 1/3 solar abundances (de Blok & van der Hulst 1998a; de Naray et al. 2004; McGaugh 1994). McGaugh (1994) did the first study of this subject and measured oxygen abundances in 22 LSB disk galaxies using optical spectra of 71 HII regions in these galaxies. He found that these galaxies have generally log (O/H) < -3.6, or metallicity, $Z < 0.3 Z_{\odot}$. With spectra of 62 HII regions in 12 LSBGs, de Blok & van der Hulst (1998a) also showed that most sample LSBGs have oxygen abundances of $Z \sim 0.1$ to 0.5 $Z_{\odot}$. de Naray et al. (2004) reconfirmed these results by measuring oxygen abundances of HII regions of six LSBGs comparing them with those values from McGaugh (1994). However, unlike McGaugh (1994), de Naray et al. (2004) reported that, with newly added samples, LSBGs also follow the metallicity-luminosity relationship. This is what Boissier et al. (2003) found based on their "homogeneous" data set which is constructed by combining several literature samples. A step further, Bergmann et al. (2003) even reported that four of their 19 LSB sample galaxies have a range of abundances from less than 1/2 solar to two times solar metallicity.

LSBGs are deficient in molecular clouds, or the formation of molecular clouds, although they are highly rich in neutral hydrogen gas. It was not until a couple years ago that any attempt to detect CO emission from LSBGs turned out successful. Schombert et al. (1990) tried to detect the CO J = 1 - 0 line from six LSBGs and did not have any detection. They explained this deficiency by reduced metal abundance. de Blok & van der Hulst (1998b) also tried to detect the cold, molecular interstellar medium (ISM) using the CO J = 2 - 1 line. They also failed to detect it from three late-type LSBGs.

Matthews et al. (2005) is the very first study to claim such detection. Using the IRAM 30 m telescope, they obtained CO J = 1 - 0 and 2 - 1 lines from four of 15 late-type edge-on, LSB spiral galaxies, although every detection was made around nuclear regions. Concentrating more on a relatively high metallicity LSBG sample, Das et al. (2006) detected CO J = 1 - 0 emission in the disks of two giant LSBGs among their seven LSBGs . They also reported that they detected a millimeter continuum source in the center of UGC 6614, which they suspected is active galactic nucleus (AGN) activity.

Unlike the heavier counterparts, neutral hydrogen is relatively abundant in LSBGs, although its surface density in LSBGs is quite low (de Blok et al. 1996; van der Hulst et al. 1993a). van der Hulst et al. (1993b) observed eight LSBGs using the Very Large Array (VLA) and found they have extended HI features beyond their optical extent and have average surface densities which are about a factor two lower than HSBGs. Following van der Hulst et al. (1993b), de Blok et al. (1996) obtained HI maps of 21 late-type LSBGs with VLA and Westerbork Synthesis Radio Telescope (WSRT). They found that these late-type galaxies have very low HI surface densities which are about a factor of 3 lower than late-type HSBGs. They also reported that their sample LSBGs have higher gas fractions than HSBGs.

These high gas fractions and high mass-to-light (M/L) ratios for LSBGs have been known and discussed for a long while (de Blok et al. 1996; Matthews et al. 2001; Romanishin et al. 1982; Schombert et al. 2001). Gas mass fractions of LSBGs sometimes approach unity (de Blok et al. 1996; Schombert et al. 2001). The M/L ratio, which is ratio of dynamical mass to luminosity, typically is a factor of two higher than in HSBGs, sometimes reaching a factor of three for LSB dwarf galaxies (Matthews et al. 2001; Romanishin et al. 1982; Schombert et al. 2001).

Not only do LSBGs have higher gas mass fractions and higher M/L ratios, their gas components also have a similar distribution to those of higher surface brightness counterparts, albeit LSB dwarf galaxies. Schombert et al. (1992) found that the distribution of HI masses for their sample is not significantly different from the Uppsala General Catalogue of Galaxies (Nilson 1973; hereafter UGC). Other large HI surveys of LSBGs (Impey et al. 2001; O'Neil et al. 2004) also had similar findings.

LSBGs have been suspected to be dust-poor (Bell et al. 2000; Bothun et al. 1997). Recent studies based upon *Spitzer Space Telescope* observations, revealed that this is approximately true. Using the Infrared Array Camera (IRAC; Fazio et al. 2004) and Multiband Imaging Photometer (MIPS; Rieke et al. 2004) mounted on *Spitzer*, Hinz et al. (2007) and Rahman et al. (2007) found that their LSBG samples, which consist of five LSBGs and three giant LSBGs respectively, are at best modest in terms of their dust components.

1.2.3 Stellar Populations, Star Formation History and Age

As mentioned, most LSBGs have optical colors which indicate rather young stellar populations (Bell et al. 1999; de Blok et al. 1995). Based on bluer optical colors (not only $U-B$ and $B-V$, but also $B-R$ and $V-I$) of LSBGs, de Blok et al. (1995) ruled out various scenarios such as a disc-fading, an initial starburst, an exponentially

declining star formation rate (SFR) and a constant SFR. Especially with $V - I$ which is an indicator of the position and degree of development of the giant branch in the Hertzsprung-Russell diagram (hereafter HR-diagram) (Bothun et al. 1984), the bluer $V - I$ colors of LSBGs suggest low metallicity and no early enrichment of ISM, which suggest a lack of major star formation in the past. Although Bell et al. (1999) advocated roughly constant sporadic star formation histories (SFHs) and did rule out very low metallicity for LSBGs, they agreed that blue LSBGs have experienced very different SFHs from HSBGs.

However, comparing optical broad-band colors with model color grids by Bruzual & Charlot (1993), van Zee et al. (1997a) argued that their LSB dwarf galaxies underwent decreasing SFHs and their typical age is at least $2 \sim 4$ Gyr. Similarly, van den Hoek et al. (2000) claimed that LSBGs not only have exponentially decreasing SFRs, but also do follow the same evolutionary history as HSBGs, albeit at a much slower rate. They insisted that it only requires small star formation bursts to explain bluer colors of LSBGs.

Recently, using optical and NIR photometry along with Hα emission line data, Zackrisson et al. (2005) found their sample LSBGs do not appear to have formed stars over cosmological time scales even with either constant or increasing SFRs. They also claimed that, even with NIR photometry available, the ages of these galaxies are poorly constrained.

Although there has not been a consensus on the SFHs of LSBGs, there is a common proposition. The current low gas surface density of LSBGs is the key factor in suppressing their star formation activity. O'Neil et al. (1998) ran simulations to investigate the effect of localized starburst on the color and surface brightness of LSBGs. They found that it is impossible to change the galaxy's central surface brightness without placing a high threshold criterion for the gas, while large amounts

of induced star formation result in centralized core components, namely bulges. These simulations suggested that star formation in LSBGs is intrinsically smaller than that in HSBGs, with fewer massive stars per HII region and that LSBGs have fundamentally different star formation processes from those of HSBGs, not just scaled-down versions.

However, Gerritsen & de Blok (1999) claimed that it requires more than low surface density to explain the slow evolution of LSBGs. They argued that a low metal content of the gas is essential and showed that a SFH model with a SFR which is low, but fluctuates, fits best. With models developed to derive the physical and chemical structure of the ISM, Mihos et al. (1999) suggested that the different evolutionary tracks of HSBGs and LSBGS are due to differences in their disk surface densities and in the conditions of their ISMs. With a smaller fraction of molecular mass and lower surface density, it is difficult for LSBGs to trigger star formation, or form a multiphase ISM and maintain it.

Bell et al. (2000) insisted that in LSBGs it is surface density which correlates with age and SFH, while metallicity correlates with both mass and surface density. They showed that there are strong correlations between an LSBG's SFH and its K-band surface brightness, K-band luminosity and gas mass fraction. Still, the aforementioned Zackrisson et al. (2005) argued that LSBG formation epochs are too ambiguous to decide even with these correlations.

1.3 The Goal of This Study

As described in the previous section, the characteristics of LSBGs raise questions regarding their formation and star formation histories which are short, but not simple:

1. When did LSBGs form? Did they form early as hierarchical galaxy formation models predict, or did they form late?

2. Why do LSBGs have such low star formation efficiencies even with large amounts of gas? Do they have a fundamentally different star formation process?

3. What do the SFHs of LSBGs look like? Have they been decreasing, constant, or increasing?

Studies of the SFHs and stellar populations of LSBGs have been mainly done using optical broad-band photometry. Obviously, as much as the use of broad-band colors is one well-established technique for probing the SFH of stellar populations, it has been difficult to quantify systematic trends in the SFH and relate them to observable physical properties. Color variation depends on many variables, such as the ages of galaxies (epoch of the formation of the first stars), the ages of stars (the luminosity weighted mean age of the stellar populations), metallicity, dust, and the initial mass function (IMF) , which results in many degeneracies when trying to constrain SFHs of galaxies.

The age-metallicity degeneracy has in particular been known to make it difficult to interpret colors. The spectra of composite stellar populations are virtually indistinguishable if the change in age or metallicity follows $\Delta\mathrm{age}/\Delta\mathrm{Z} \sim 3/2$ (Worthey 1994). This age-metallicity degeneracy is especially important in understanding the SFHs of LSBGs. Generally blue in their colors, LSBGs are dominated by young stellar components, even if they are not young. If indeed LSBGs formed as recently as $2 \sim 4$ Gyrs ago, their presence challenge current models of hierarchical galaxy formation in the λCDM cosmology (Zackrisson et al. 2005). Based on the hydrodynamic galaxy formation models of Nagamine et al. (2000), only a small fraction of

galaxies with present stellar mass lower than $10^{10} M_{\odot}$ should have formed that late in this cosmology.

However, there exist giant LSBGs (an extreme example of which is Malin 1) whose central colors are similar to those of old stellar populations. There also exists a substantial population of red LSBGs (O'Neil et al. 1997) which does not fit into the picture developed to explain blue LSBGs. Although the red colors could result either from age or metallicity, the existence of old or metal-rich LSBGs is hard to understand if LSBGs are expected to be unevolved because of their low surface densities.

This age-metallicity degeneracy is only broken by certain combinations of spectral-line indices or limited combinations of broad-band colors (de Jong 1996). Bell et al. (2000) applied this methodology to avoid the age-metallicity degeneracy and to investigate the SFHs of LSBGs using a combination of optical and NIR colors available. However they assumed an absolute age of the galaxies, 12 Gyrs. Zackrisson et al. (2005) showed that certain colors of a galaxy may well be represented by multiple combinations of absolute ages, average ages of stars and different SFHs.

While it still looks like a complicated task, we can put more constraints on the SFHs of LSBGs by adding more observable physical parameters. First of all, we can put more constraints on the normalization of the SFHs with the current star formation rates and the time averaged star formation rates.

It is also known that for continuously star forming galaxies, the near-IR colors are better indicators of the total stellar mass than the bluer optical bands. With the current star formation rates, $\dot{M}$ from Hα and the time averaged star formation rates, $\langle \dot{M} \rangle$ from the total stellar mass over the Hubble time, we can put more constraints on the normalization of the SFHs. If we consider SFHs of galaxies as functions of time, these two parameters, total stellar masses and current star

formation rates determine the "amplitudes" of SFHs, while the gas mass fraction determines "shapes" of the SFHs. Since the total mass of consumed gas is the total stellar mass which is formed by the gas consumption assuming "closed-box", the dependence of gas mass fractions on time determines how the SFHs of galaxies vary. On the other hand, while combined colors of optical and near-IR bands help break the age-metallicity degeneracy, these colors provide star formation time scales. Therefore, with this study, we hope to construct the overall SFHs using $\dot{M}$, $\langle\dot{M}\rangle$, and gas fraction.

In Chapter 2, we present our data and analysis of optical and near-infrared broadband photometry of a large sample of LSBGs. We perform surface photometry on these data and analyze their disk and bulge structure. We also discuss LSBG colors and the correlation of color with other physical properties.

In Chapter 3, we present Hα photometry of sample low surface brightness galaxies as well as current star formation rates for these sample galaxies and discuss dependence on other parameters. We also discuss the composite HII region luminosity function.

In Chapter 4, we illustrate our methods for calculating the mass of the stellar component masses of our sample galaxies based on broadband colors. Based on these results, we also derived gas mass fraction. With multiple data sets, namely gas and stellar components and their masses, current star formation rates, colors and structural parameters from broadband photometry, we analyze their correlations and impact on star formation histories of low surface brightness galaxies. We construct the normalized star formation rate, which is the ratio between current star formation rates and past star formation rates, and their correlations with other physical properties. We then discuss what these correlations mean.

In Chapter 5, we summarize our results and discuss prospects for future research.

Chapter 2

Optical and Near-infrared Broadband Photometry of Low Surface Brightness Galaxies

2.1 Overview

Tracing the star formation history (SFH) of galaxies is fundamental to understanding the evolution of galaxies. However, it is a hard task to analyze generations of stellar populations in galaxies which have continuing stellar formation with various physical conditions. Especially, it is impossible to resolve young individual stars in galaxies beyond the Local group, so we are limited to the statistical study of large scale star formation events for most galaxies, one of which is the use of broadband colors.

Color variation depends on the ages of galaxies (epoch of the formation of the first stars), the ages of stars (the luminosity weighted mean age of the stellar populations), metallicity, dust, and the IMF. The age-metallicity degeneracy in particular

makes it difficult to discern integrated spectra of composite stellar populations. The spectra of composite stellar populations are virtually identical if the change in age or metallicity (Z) follows $\Delta\text{age}/\Delta Z \sim 3/2$ (Worthey 1994). This age-metallicity degeneracy is only broken for certain combinations of spectral-line indices or for limited combinations of broadband colors (de Jong 1996).

Compared to their high surface brightness counterparts, little is known about the star formation properties of low surface brightness galaxies (LSBGs ; galaxies usually with B-band central surface brightness fainter than 23 mag arcsec^{-2}). Most LSBGs have optical colors which indicate rather young stellar populations (Bell et al. 1999; de Blok et al. 1995). Most observations (low current massive star formation rates, high gas mass fraction and low metallicity) are consistent with a scenario in which LSBGs are unevolved, low-metallicity, low mass surface density systems, with constant or increasing SFRs (de Blok et al. 1996).

However, there have been various difficulties for this scenario. The existence of giant LSBGs (an extreme example of which is Malin 1) whose central colors are similar to those of old stellar populations, is one example of the difficulties. There also exists a substantial population of red LSBGs (O'Neil et al. 2007a) which does not fit into the picture developed to explain blue LSBGs. The red colors, however, could result either from age or metallicity. Still, the existence of old or metal-rich LSBGs is hard to understand if LSBGs are expected to be unevolved because of their low surface densities. Using a combination of optical and near-IR colors, it is possible to avoid the age-metallicity degeneracy and to learn more about SFH for stellar populations with ongoing star formation (Bell et al. 2000).

In this chapter, we present our optical and near-infrared observations and data in order to investigate stellar populations of LSBGs. In section 2.2, we describe our observations and data reduction in detail. In section 2.3, we present optical and

near-infrared images which we obtained from observations and describe our sample galaxies. In section 2.4, we present our surface photometry and describe results. We talk about structural parameters which measure from our surface photometry. In section 2.5, we discuss results.

2.2 Observations and Data Reduction

2.2.1 Sample Selection

We select about 50 sample galaxies which already have some target observations. These galaxies have been selected for previous studies since their central surface brightnesses are known to be low, at least lower than 22.0 mag arcsec^{-2}, which is one sigma below Freeman's value ($\mu_0(B) = 21.65 \pm 0.30$ mag arcsec^{-2}). The cutoff in central surface brightness is not firmly fixed to define low surface brightness galaxies. Certainly, however, our sample galaxies have central surface brightnesses fainter than 22.0 mag arcsec^{-2}.

Among previous studies on LSBGs, de Blok et al. (1996) provides good sample LSB galaxies which have neutral hydrogen maps and optical broadband photometry. The Second Palomar Sky Survey (SPSS) sample provided by Pildis et al. (1997) and Schombert et al. (1997) are gas-rich ($f_{gas} > 0.3$; in some cases $f_{gas} > 0.9$; McGaugh & de Blok 1997; Schombert et al. 2001) dwarf galaxies ($V_{flat} < 90$ km s^{-1}; $M_* < 10^9 M_\odot$; McGaugh 2005) with optical broadband photometry. de Blok et al. (2001) and McGaugh et al. (2001) have UGC and ESO-LV galaxy samples with high resolution rotation curves. We randomly picked our sample galaxies from these two studies.

By no means, is our sample complete. Defining a complete sample of LSBGs is virtually impossible since the most extreme cases by definition reside in the margins

of survey completeness. However, our sample LSBGs does have a wide range of physical parameters. We randomly select galaxies from multiple previous studies, thereby we should at least obtain a fair sampling of the properties of known LSBGs. Basic properties of our sample galaxies are provided in Table 2.1.

2.2.2 Near-Infrared Data

Observations

All observing runs for NIR broadbands were obtained with the Mayall 4-m telescope at Kitt Peak National Observatory using the Florida Multi-object Imaging Near-IR Grism Observational Spectrometer (hereafter FLAMINGOS; http://www.noao.edu/kpno/manuals/flmn/). FLAMINGOS has a single 2k $\times$ 2k HgCdTe array, which has a pixel scale of $0.''316$ pixel^{-1} at the Mayall 4-m telescope. The field of view is $10.'8 \times 10.'8$.

There were 3 runs of four to seven nights, the first of which started on October 10, 2003 and finished on October 16, 2003. For this run, we lost about a third of the time due to weather, in particular due to thunderstorm. For the rest of the run, it was photometric. The second run started on May 27, 2004 and finished on May 30, 2004. Although it was photometric for most of the run, the instrument control system crashed from time to time due to unknown reasons. Although this phenomenon had been known to happen quite often, no viable solution other than "being careful" was known by the time of our third run. Due to this crash, we lost about a night from the second run and another night and a half from the third run, which started on January 27, 2005 and finished on January 31, 2005.

Observation procedures were carefully designed due to the low surface brightness of sample galaxies. Based on known optical broadband surface brightness, we esti-

Table 2.1. Basic Properties of Sample Galaxies

Galaxy	RA (J2000.0)	Dec (J2000.0)	V_{helio}	Distance	i	P.A.	Alternate
			(kms^{-1})	(Mpc)	(deg)	(deg)	Names
(1)	(2)	(3)	(4)	(5)	(6)	(7)	(8)
D512-2	14 33 20.1	+26 59 50.0	835	11.6	61^a		F512-1
D570-4	11 18 21.4	+17 41 51.0	1051	14.6	47^a		F570-7
D575-2	12 52 21.1	+21 37 46.2	776	10.8	61^a		UGC 8011
D575-5	12:55:40.5	+19:12:33.0	419	5.8	64^a		F575-3
D584-2	16 01 49.3	+18 43 14.6	2627	36.5	52^a		UGC 10410
D584-4	15 57 27.5	+20 39 58.0	2264	31.4	63^a	355	F583-1
D646-5	12 52 59.1	+14 24 04.9	1020	14.2	63^d	29	F646-1
D721-5	14 02 43.5	+09 59 29.0	5811	80.7	47^a		F721-v4
F561-1	08 09 41.3	+22 33 33.0	4807	66.8	24^b		
F563-V1	08 46 37.8	+18 55 26.0	3890	54.0	60^b		D563-3
F568-1	10 26 06.3	+22 26 01.0	6524	90.6	26^b	13	
F571-8	11 33 55.1	+19 21 36.7	3731	51.8	90^b	165	
F577-V1	13 50 10.1	+18 16 07.7	7788	108.2	35^c	40	
F611-1	01 19 47.4	+16 47 24.6	2163	30.0	38^c		
F730-V1	17 03 55.9	+10 10 48.0	10714	148.8	50^d	16	
NGC 4455	12 28 44.1	+22 49 21.0	637	8.8	78^e	197	UGC 7603
UGC 128	00 13 50.9	+35 59 39.0	4531	62.9	57^f	62	
UGC 334	00 33 54.9	+31 27 02.6	4627	64.3	24^g	45	DDO 4
UGC 628	01 00 51.9	+19 28 32.9	5446	75.6	56^g	139	
UGC 731	01 10 43.9	+49 36 07.9	639	8.9	57^e	257	DDO 9
UGC 1230	01 45 32.5	+25 31 16.0	3833	53.2	25^c	112	
UGC 2259	02 47 55.4	+37 32 18.6	583	8.1	43^h	160	
UGC 2885	03 53 04.3	+35 35 31.0	5802	80.6	62^i	225	
UGC 3371	05 56 38.6	+75 18 58.0	816	11.3	49^c	133	DDO 39
UGC 6614	11 39 14.8	+17 08 36.8	6352	88.2	34^c	108	
UGC 8837	13 54 45.7	+53 54 02.7	144	3.8^*	80^e	22	DDO 185
UGC 9992	15 41 47.8	+67 15 15.3	427	8.8^*	30^d	35	
UGC 10310	16 16 18.3	+47 02 47.1	716	9.9	34	19^d	DDO 204
UGC 11454	19 31 33.6	+49 52 46.4	6628	92.1	64^d	106	
UGC 11557	20 23 58.3	+60 11 33.4	1390	19.3	36^d	94	
UGC 11583	20 30 15.3	+60 26 25.0	127	5.9^*	83^d	88	
UGC 11616	20 41 13.5	+63 30 38.4	5244	72.8	60^d	99	
UGC 11648	20 53 09.5	+67 10 32.9	3361	46.7	83^d	145	
UGC 11748	21 27 39.8	+45 28 58.8	5265	73.1	81^d	103	
UGC 11819	21 49 10.7	+41 56 53.3	4261	59.2	66^d	167	
UGC 11820	21 49 28.4	+14 13 52.0	1104	15.3	50^d	48	
UGC 11944	22 12 00.7	+17 54 09.6	1734	24.1	72^d	30	
UGC 12695	23 36 02.2	+12 52 32.5	6185	85.9	49^c		

Note. — This research has made use of the NASA/IPAC Extragalactic Database (NED), which is operated by the Jet Propulsion Laboratory, California Institute of Technology, under contract with the National Aeronautics and Space Administration.

$*$: Refer to Col(5) explanation

Col.(2),(3),(4): Based on NASA/IPAC Extragalactic Database.

Col(5): Hubble flow distances assuming $H_0 = 72 kmsec^{-1}Mpc^{-1}$ except UGC 8837, UGC 9992 and UGC 11583, for which Hubble flow distances calculated based on Local group model are listed.

REFERENCES - (a)Eder & Schombert (2000) (b)de Blok et al. (1996) (c) McGaugh & Bothun (1994) (d) McGaugh et al. (2001) (e) de Blok & Bosma (2002) (f) de Blok et al. (1995) (g) Bell et al. (2000) (h) Carignan et al. (1988) (i) Canzian (1993)

mated exposure times for the J and K_s bands. Our target exposure time in the K_s band was 40 minutes. While sky subtraction is applied by median sky frames from target images for many cases, we wanted to be more careful with handling our sample galaxies. Therefore we always obtained a separated dithered sets of sky for each galaxy matching total exposure time on sky to galaxies. We also accounted for rapid sky fluctuation in the sky by sandwiching each dithering set of target galaxy frames and sky frames, which means that, after a dither set of a galaxy which generally consists of nine exposures, a dither set of neighboring sky field which also consists of 9 exposures follows. With typical exposures time for an individual image running from 30 seconds to 45 seconds, a dither pattern never took longer than 8 minutes. We also chose sky fields very carefully so that there is no major extended object, especially bigger than a dithering gap, in those fields. With a default dithering gap of $5''$, we increased it to $10''$ when we could not find any suitable sky fields without a major extended object. Considering overhead, it generally took slightly longer than 2 hours to obtain an image set for a galaxy.

Table 2.2. Parameters of Near-Infrared Observations

Galaxy	Date	Telescope/Instrument	Band	Exp.Time
D512-2	May 28 2004	KPNO 4m/FLMN	K_s	31.5min
D564-8	Feb 1 2005	KPNO 4m/FLMN	K_s	36min
D565-5	Jan 29 2005	KPNO 4m/FLMN	K_s	45min
D570-4	May 29 2004	KPNO 4m/FLMN	K_s	36min
D575-2	May 30 2004	KPNO 4m/FLMN	K_s	36min
D575-5	May 31 2004	KPNO 4m/FLMN	K_s	36min
D584-2	May 30 2004	KPNO 4m/FLMN	K_s	36min
D584-4	May 31 2004	KPNO 4m/FLMN	K_s	36min
D721-5	May31 2004	KPNO 4m/FLMN	K_s	36min
D723-4	Jan 29 2005	KPNO 4m/FLMN	K_s	22.5min
D774-1	Jan 31 2005	KPNO 4m/FLMN	K_s	36min
F563-1	Feb 1 2005	KPNO 4m/FLMN	K_s	36min
F563-V1	Jan 31 2005	KPNO 4m/FLMN	K_s	22.5min
	Feb 1 2005	KPNO 4m/FLMN	K_s	13.5min
F563-V2	Jan 31 2005	KPNO 4m/FLMN	K_s	22.5min
	Feb 1 2005	KPNO 4m/FLMN	K_s	13.5min
F565-V2	Jan 29 2005	KPNO 4m/FLMN	K_s	45min
F568-1	May 28 2004	KPNO 4m/FLMN	K_s	27min
F568-V1	Jan 29 2005	KPNO 4m/FLMN	K_s	36min
F571-8	May 30 2004	KPNO 4m/FLMN	K_s	36min
F577-V1	May 29 2004	KPNO 4m/FLMN	K_s	40min
F611-1	Jan 28 2005	KPNO 4m/FLMN	K_s	40.5min
NGC 4455	May 28 2004	KPNO 4m/FLMN	K_s	40.5min
UGC 128	Oct 14 2003	KPNO 4m/FLMN	K_s	40min
UGC 334	Oct 15 2003	KPNO 4m/FLMN	K_s	26.7min
	Oct 17 2003	KPNO 4m/FLMN	K_s	13.3min
UGC 628	Oct 13 2003	KPNO 4m/FLMN	K_s	45min
UGC 731	Oct 12 2003	KPNO 4m/FLMN	K_s	41.25min
UGC 1230	Oct 14 2003	KPNO 4m/FLMN	K_s	40min
	Oct 17 2003	KPNO 4m/FLMN	J	40min
UGC 2259	Oct 13 2003	KPNO 4m/FLMN	K_s	45min
	Oct 16 2003	KPNO 4m/FLMN	J	40min
UGC 2885	Oct 12 2003	KPNO 4m/FLMN	K_s	30min
	Oct 14 2003	KPNO 4m/FLMN	K_s	15min
UGC 3371	Oct 15 2003	KPNO 4m/FLMN	K_s	34.7min
	Oct 16 2003	KPNO 4m/FLMN	K_s	5.3min
	Oct 17 2003	KPNO 4m/FLMN	K_s	10.7min
	Oct 17 2003	KPNO 4m/FLMN	J	40min
UGC 5750	Jan 29 2005	KPNO 4m/FLMN	K_s	36min
UGC 5981	Feb 1 2005	KPNO 4m/FLMN	K_s	40min
UGC 6614	May 31 2004	KPNO 4m/FLMN	K_s	36min
UGC 8837	May 30 2004	KPNO 4m/FLMN	K_s	36min
UGC 9992	May 29 2004	KPNO 4m/FLMN	K_s	36min
UGC 10310	May 29 2004	KPNO 4m/FLMN	K_s	18min
	May 30 2004	KPNO 4m/FLMN	K_s	9min
	May 31 2004	KPNO 4m/FLMN	K_s	4.5min
UGC 11454	Oct 13 2003	KPNO 4m/FLMN	K_s	45min
UGC 11557	Oct 14 2003	KPNO 4m/FLMn	K_s	40min
UGC 11583	Oct 15 2003	KPNO 4m/FLMN	K_s	40min
UGC 11616	Oct 12 2003	KPNO 4m/FLMN	K_s	45min
	May 28 2004	KPNO 4m/FLMN	K_s	22.5min
	May 31 2004	KPNO 4m/FLMN	K_s	9min
UGC 11648	Oct 15 2003	KPNO 4m/FLMN	K_s	26.7min
	Oct 16 2003	KPNO 4m/FLMN	K_s	13.3min
UGC 11748	Oct 14 2003	KPNO 4m/FLMN	K_s	40min
UGC 11819	Oct 15 2003	KPNO 4m/FLMN	K_s	40min
	Oct 17 2003	KPNO 4m/FLMN	J	40min

Table 2.2 (cont'd)

Galaxy	Date	Telescope/Instrument	Band	Exp.Time
UGC 11820	Oct 16 2003	KPNO 4m/FLMN	K_s	40min
	Oct 16 2003	KPNO 4m/FLMN	J	40min
UGC 11944	Oct 13 2003	KPNO 4m/FLMN	K_s	30min
	Oct 17 2003	KPNO 4m/FLMN	K_s	15min
UGC 12695	Oct 16 2003	KPNO 4m/FLMN	K_s	40min
	Oct 17 2003	KPNO 4m/FLMN	J	40min

Data Reduction

We used XDIMSUM for data reduction. XDIMSUM is an add-on IRAF package for creating accurate sky subtracted images from sets of dithered observations (http://iraf.noao.edu/iraf/ftp/iraf/extern/xdimsum020627/xdimsum.readme). However, the reduction procedure from XDIMSUM assumes that there is no separate set of sky fields. Therefore we used the reduction scheme as follows.

After subtracting an average dark frame, which has the same exposure time as the source, each galaxy and sky image is divided by a dome flat. This dome flat is generated by subtracting an average image of a series of low illuminated dome flats from an image of another series of high luminated dome flats.

Then we measured the median value of images using the center quarter of images. With these median values, we calculated differences of sky medians from the lowest one. Then we constructed a new set of sky frames by subtracting the differences from original sky frames. Via this process, we eliminated excessive sky fluctuation in order to obtain true local variation in sky level.

After calculating shifts between sky images, we constructed combined sky images for each dither set. Adding object masks extracted from each sky image to bad pixel masks and cosmic ray masks which are generated before combining, we generated a mask for each sky frame. When we combined sky images within dithering sets without shifts, we produced true sky frames, which we subtracted from galaxy

frames.

However, differences between median levels were considered yet again, and subtracted from galaxy frames before sky subtraction. Then final images are constructed considering shifts between image frames.

Astrometric Calibration

Basic astrometric calibration is performed by MSCGETCAT and MSCCMATCH tasks, which are provided by MSCRED package. Although our combined images are not mosaic images, we used MSCCMATCH task since its interactive procedures perform fast and effectively on single images as well.

Photometric Calibration

In order to perform photometric calibration, we refer to Persson et al. (1998). We obtained a dithered set of images of standard stars from Persson et al. (1998), which were available between acquisitions of target galaxy images. Generally, we observed about 4 sets of standard star images per night. A dithered set consists of 5 frames, of which exposure time is either 5 seconds, or 10 seconds depending on apparent magnitudes of target standard stars.

Since we have too few standard stars per night, we do not measure extinction coefficients (Figs.2.1 (a) and (b)). In addition to lack of standard star data points, sky background fluctuation overwhelms error in measurement. A typical value for sky fluctuation in a given K_s image is about 0.07 mag, sometimes reaching 0.1 mag. This is comparable to the typical extinction correction at the observed airmasses.

Instead, we calculated averages of photometric zeropoints given by each measurement. Figs.2.1 (c) and (d) show averages of zeropoints for each night during October 2003 and May 2004 runs.

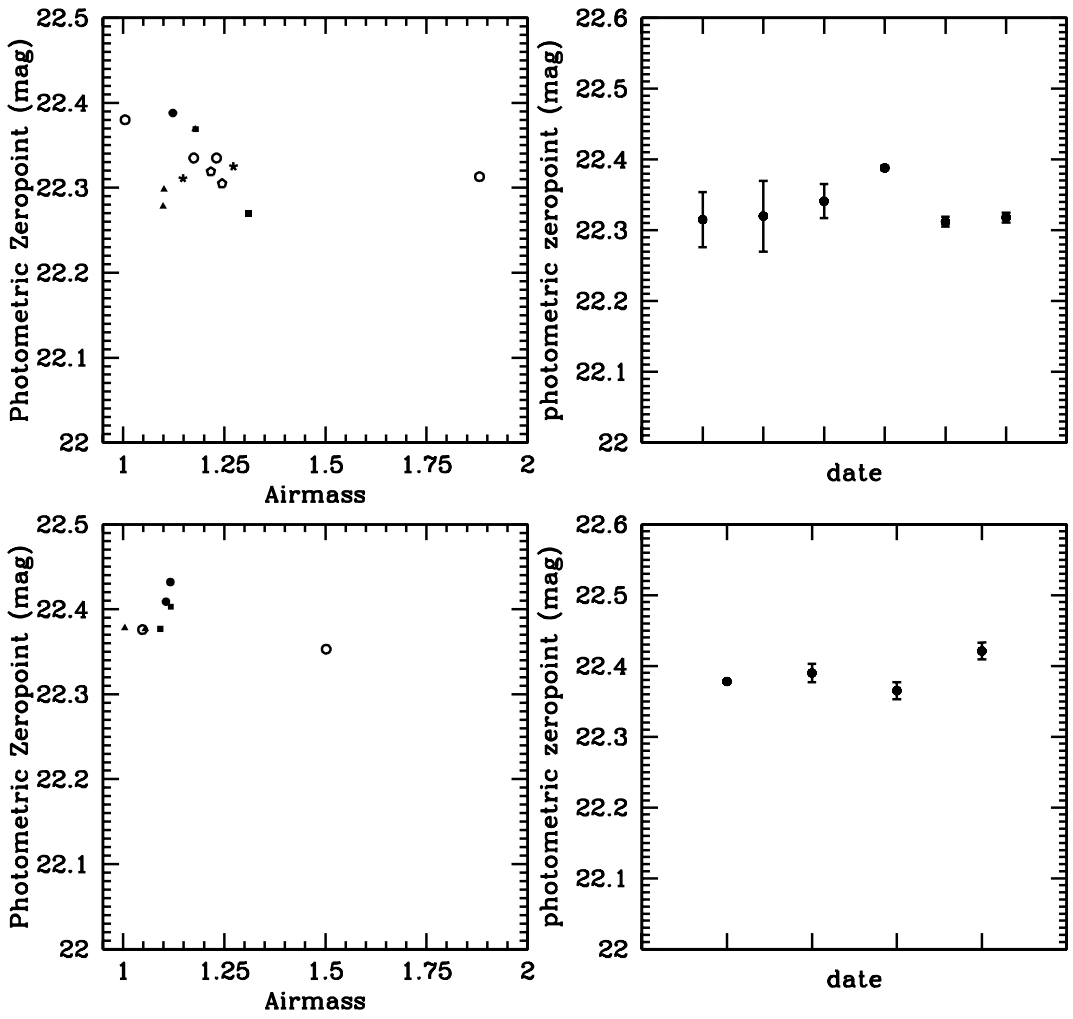

Figure 2.1: (a) Photometric zeropoints of standard stars plotted against airmass for October 2003 run and (b) May 2004 runs. (c) Average zeropoints for each night of October 2003 run. Error bars show a standard deviation for each night. (d) Average zeropoints for each night of May 2004 run.

Our estimated photometric zeropoints are 22.328 mag and 22.388 mag for October 2003 and May 2004, respectively.

2.2.3 Optical Data

Observation

10 LSB galaxies were observed at the 2.1-m telescope at Kitt Peak National Observatory through BVR filters in 2003 June after a three day run was stormed out totally in 2002 June. T2KA CCD was used during the three day run. This CCD has a pixel size of $0.''305$ pixel^{-1} and has a comparable field of view ($\sim 10' \times 10'$) to FLAMINGOS. Another LSB galaxy, UGC 2259, was observed at the 2.1-m telescope at Kitt Peak National Observatory using the same instrument by Kuzio-de Nary in September, 2004.

Data reduction for these optical images followed standard procedures using IRAF. This applied bias and dark current subtraction and flat fielding, which is performed with dome flats.

In order to complement our optical data, we used optical broadband images for 11 LSB galaxies from McGaugh & Bothun (1994). Theses images were obtained through filters with the McGraw Hill 1.3-m telescope of the MDM Observatory in 1991 February, 1991 November, and 1992 January. Two similar CCDs were employed for these runs. A TI-4849 CCD was used for the 1991 February session and a Thomson CCD was used for the other two session. Both of the CCDs have the identical scale, $0.''48$ pixel^{-1}. Standard procedures using IRAF were used for the data as well. McGaugh & Bothun (1994) describes observations and data reduction in detail.

Table 2.3. Observation Parameters for Sample Galaxies

Galaxy	Date	Telescope/Instrument	Band	Exp.Time
D646-5	Jun 27 2003	KPNO 2.1m/CFIM+T2KB	*B*	30min
	Jun 27 2003	KPNO 2.1m/CFIM+T2KB	*V*	20min
	Jun 27 2003	KPNO 2.1m/CFIM+T2KB	*R*	20min
D721-5	Jun 26 2003	KPNO 2.1m/CFIM+T2KB	*B*	30min
	Jun 25 2003	KPNO 2.1m/CFIM+T2KB	*V*	20min
	Jun 25 2003	KPNO 2.1m/CFIM+T2KB	*R*	20min
F730-V1	Jun 25 2003	KPNO2.1m/CFIM+T2KB	*B*	30min
	Jun 25 2003	KPNO2.1m/CFIM+T2KB	*V*	20min
	Jun 25 2003	KPNO2.1m/CFIM+T2KB	*R*	20min
UGC 2259	Sep 12 2004	KPNO 2.1m/CFIM+T2KB	*B*	20min
	Sep 12 2004	KPNO 2.1m/CFIM+T2KB	*R*	10min
UGC 11454	Jun 26 2003	KPNO 2.1m/CFIM+T2KB	*B*	30min
	Jun 26 2003	KPNO 2.1m/CFIM+T2KB	*V*	20min
	Jun 26 2003	KPNO 2.1m/CFIM+T2KB	*R*	20min
UGC 11583	Jun 25 2003	KPNO 2.1m/CFIM+T2KB	*B*	30min
	Jun 25 2003	KPNO 2.1m/CFIM+T2KB	*V*	20min
	Jun 25 2003	KPNO 2.1m/CFIM+T2KB	*R*	20min
UGC 11616	Jun 26 2003	KPNO 2.1m/CFIM+T2KB	*B*	30min
	Jun 26 2003	KPNO 2.1m/CFIM+T2KB	*V*	20min
	Jun 26 2003	KPNO 2.1m/CFIM+T2KB	*R*	20min
UGC 11748	Jun 26 2003	KPNO 2.1m/CFIM+T2KB	*B*	30min
	Jun 26 2003	KPNO 2.1m/CFIM+T2KB	*V*	10min
	Jun 26 2003	KPNO 2.1m/CFIM+T2KB	*R*	20min
UGC 11819	Jun 25 2003	KPNO 2.1m/CFIM+T2KB	*B*	30min
	Jun 25 2003	KPNO 2.1m/CFIM+T2KB	*V*	20min
	Jun 25 2003	KPNO 2.1m/CFIM+T2KB	*R*	20min

Astrometric Calibration

Since original CCD images obtained from KPNO 2.1-m telescope and T2KB CCD combination do not carry any world coordinate system (WCS) information in them, we have to run processes in order to generate one in each image. Basically we inserted WCS information which roughly corresponds to centers of sample galaxies and orientation of the instrument. Then we run an identical astrometric calibration process with MCSGETCAT and MSCCMATCH tasks. As with the case of FLAMINGOS images, this provides us quicker and more efficient solutions.

Photometric Calibration

We use reference stars from Landolt (1992). We measure zeropoints for standard stars first, then measure extinction coefficients based on given airmass using the least-square fitting. With extinction coefficients added, we fit color terms based on colors given in Landolt (1992). We choose B-V, B-V, and V-R for B-, V-, and R-bands, respectively, for June 2003 run and B-R for both B-, and R-bands. Once we obtain photometric calibration relations, we fit for extinction coefficients again with added color terms, and then for color coefficients again. We run recursive fittings for extinction and color coefficients until shifts in fitting results are slight. Generally it does not require more than 3 recursive fitting processes.

Final photometric calibration relationships for June 2003 run are;

$$B - b = 23.827 + 0.088 \times (B - V) - 0.236 \times \chi_B \quad (2.1)$$

$$V - v = 23.894 + 0.048 \times (B - V) - 0.141 \times \chi_V \quad (2.2)$$

$$R - r = 23.965 + 0.075 \times (V - R) - 0.103 \times \chi_R \quad (2.3)$$

Those fits are shown in Fig.2.2.

Then, for September 2004, they are;

$$B - b = 23.737 + 0.009 \times (B - R) - 0.189 \times \chi_B \quad (2.4)$$

$$R - r = 23.963 + 0.020 \times (B - R) - 0.085 \times \chi_R \quad (2.5)$$

Fig.2.3 shows fits for photometric calibration of September 2004 run.

For the sample galaxies from McGaugh (1992), we use photometric calibration relationship derived and given by McGaugh (1992). For February 1991 run, they are;

$$B - b = 21.234 - 0.061 \times (B - I) - 0.250 \times \chi_B \quad (2.6)$$

$$I - i = 21.594 + 0.065 \times (B - I) - 0.060 \times \chi_I \quad (2.7)$$

For October/November 1992 run, they are;

$$U - u = 19.901 + 0.038 \times (U - B) \quad (2.8)$$

$$B - b = 20.909 - 0.099 \times (B - V) \quad (2.9)$$

$$V - v = 21.725 + 0.005 \times (B - V) \quad (2.10)$$

$$I - i = 21.864 - 0.040 \times (V - I) \quad (2.11)$$

for the first three nights of the run. Then, for the last three nights of the run, they are;

$$U - u = 19.989 + 0.039 \times (U - B) \quad (2.12)$$

$$B - b = 21.022 - 0.081 \times (B - V) \quad (2.13)$$

$$V - v = 21.810 + 0.023 \times (B - V) \quad (2.14)$$

$$I - i = 21.900 - 0.033 \times (V - I) \quad (2.15)$$

Since instrumental magnitudes have been corrected for atmospheric extinction with the "Mt. Pinotubo" coefficients, these do not have extinction terms separately.

For January/February 1992 run, they are;

$$U - u = 19.892 - 0.017 \times (U - B) \quad (2.16)$$

$$B - b = 20.916 - 0.130 \times (B - V) \quad (2.17)$$

$$V - v = 21.686 + 0.019 \times (B - V) \quad (2.18)$$

$$I - i = 21.790 - 0.020 \times (V - I) \quad (2.19)$$

These do not include extinction coefficients since their instrument magnitude already have been corrected with "Mt. Pinotubo" coefficients as well.

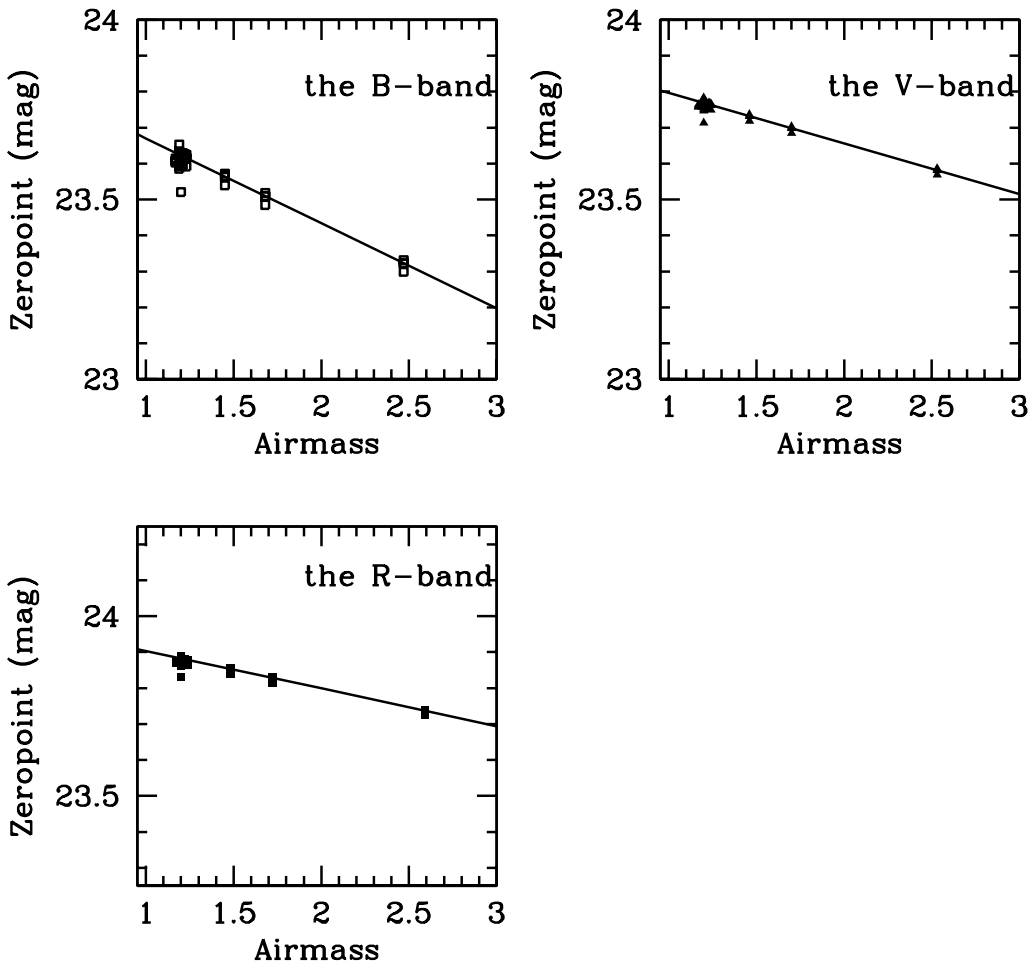

Figure 2.2: Photometric calibration for June 2003 run at KPNO 2.1-m telescope.

2.3 Images of Sample Galaxies

We present here the K_s-band images of sample galaxies along with available multi-color optical CCD images.

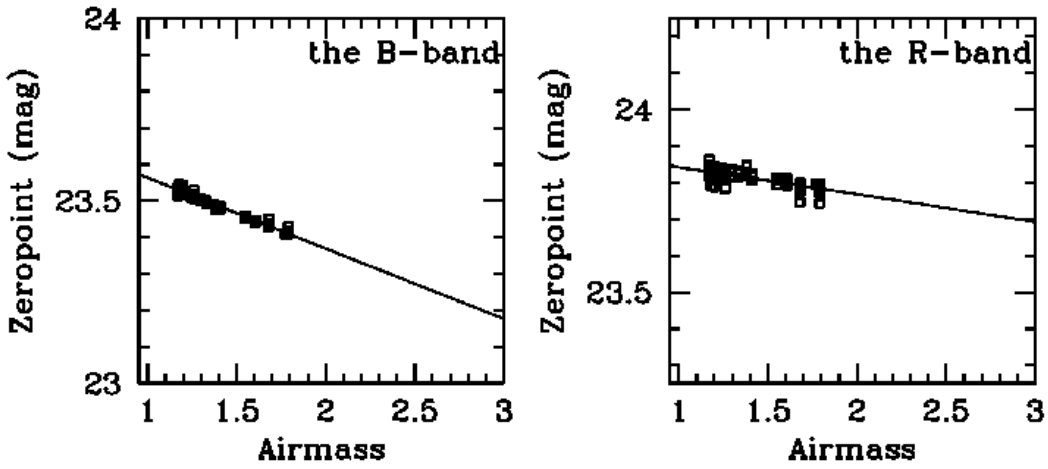

Figure 2.3: Photometric calibration for September 2004 run at KPNO 2.1-m telescope.

2.3.1 D512-2

This LSB galaxy is barely detected in K_s-band, while a bright foreground star resides southwest to the center of the galaxy (Fig.2.23 (a)). Although the galaxy is hardly prominent against the sky, it still clearly shows asymmetric structure. It has a broad tail-like feature northeast, while it does not show anything beyond the foreground star.

2.3.2 D575-2

An asymmetric, amorphous galaxy does not show any clear feature, although it has several knots on it. Its surface brightness profile does not have a clear exponential disk, either (Fig.2.23 (b)).

2.3.3 D584-2

Although this LSB dwarf galaxy hints some morphological structure, especially an exponential disk, it is still an amorphous LSB galaxy (Fig.2.4). However, around the central region, it shows some star formation activity which will be discussed more later.

2.3.4 D721-5

This LSB disk galaxy looks like nothing but a small lump in the K_s-band (Fig.2.6). However, this lump is actually the bulge region of this LSB galaxy, which has an extended disk. Its surface brightness profiles in the optical and the K_s-band fit nicely into Freeman type 2 exponential disk.

2.3.5 F561-1

This LSBG is very similar to D721-5 although it is a little closer. (Fig.2.7) Only the B-band image shows its spiral structure clearly.

2.3.6 F563-V1

This is an amorphous LSBG (Fig.2.8). It does not show any clear structure, such as bulge, disk or spiral arms.

2.3.7 F563-V2

This LSBG shows very interesting features. First, it has an extended structure northwest. This structure may be a spiral arm and a big blog just west to the center of F563-V2 may be a companion galaxy. There is nothing southeast to its center. (Fig.2.9)

2.3.8 F568-1

This LSB disk galaxy is a type Sc and still shows in the K_s-band (Fig.2.10). Although with weak spiral arm feature, it has a very clear bulge and a type I exponential disk. At the redshift of 0.0218, its scale length is also very big ($\sim$ 21.5 kpc) in the K_s-band.

2.3.9 F571-8

With a very thick bulge inside, this edge-on disk galaxy shows very long, extended, albeit thin disk (Fig.2.23 (c)). The surface density profile shows a dominant central region. Since the bulge is so big, it does not resemble any typical disk type, although its disk shows a nice clean exponential feature.

2.3.10 F577-V1

This LSB galaxy barely shows detection, although it still shows weak spiral arm and bar feature (Fig.2.11). Without a clear showing of exponential disk, this galaxy can be a representative example of hidden galaxies, if longer exposure reveal more distinctive structure.

2.3.11 F611-1

This is an asymmetric LSB dwarf galaxy (Fig.2.12). There is a very compact nucleus in the northwest and other diffuse structures lie southeast to it.

2.3.12 F730-V1

This LSBG is a quite distant galaxy which shows a quite big central structure with a small disk (Fig.2.13). It is very difficult to distinguish its spiral arms from its disk.

2.3.13 NGC 4455

This galaxy is another high surface brightness galaxy (Fig.2.25 (e)). While this galaxy has a relatively smooth exponential disk, it still has lumpy features on its surface brightness profile. It has lots of knots along outer parts of the disk. Comparison to Hα images will follow in a separate paper for Hα data.

2.3.14 UGC 128

This galaxy shows nice spiral arm features in available optical band images (Fig.2.23 (d)). On the other hand, its K_s-band image only hints its spiral arm feature at the rim of its bulge area by showing a couple nudging tips outward.

2.3.15 UGC 334

This LSB galaxy shows a very clear bar in available optical band images and probably is a type SBb galaxy (Fig.2.23 (e)). However, in our K_s-band image, the only feature which it shows best is its bar. It still hints its northeast spiral arm from the tip of its bar, though. Its disk has a weak exponential feature.

2.3.16 UGC 628

While this disk galaxy shows a bar-like feature within the central region, it also suggests spiral arms branched off the bar-like feature (Fig.2.23 (f)). Its central region looks very dominant, while its surface brightness profile shows an exponential disk without an eminent central peak.

2.3.17 UGC 731

This LSB galaxy looks just amorphous in the K_s-band (Fig.2.24 (a)). However, it shows its spiral arms moving up to shorter wavelengths and, probably its huge bar as well. The same features are noticeable in the K_s-band, if one looks into the image carefully.

2.3.18 UGC 1230

This face-on LSB galaxy has an extremely thin disk through which several background galaxies are detected (Fig.2.14). This is true for images from optical bands through the K_s-band. On the other hand, it has spiral arms, which are not evident through all bands. While spiral arm feature exist, it is extremely difficult to distinguish one arm from another. Type 1 exponential disk is well fitted to surface photometry.

2.3.19 UGC 2259

This is a nice face-on galaxy which has two distinctive spiral arms (Fig.2.15). It has a ring around its central region, which also shows up on its exponential disk of the surface brightness profile.

2.3.20 UGC 2885

This galaxy is an intermediate surface brightness galaxy, which is included into the sample for comparison (Fig.2.24 (b)). Although it has a moderate central surface brightness, this galaxy has huge scale lengths, even in the K_s-band ($\sim$ 16.5 kpc). With a very bright foreground star northeast, it displays asymmetric spiral arm feature, although its spiral arms are evident. Its exponential disk is well-defined and flat.

2.3.21 UGC 3371

This is an amorphous dwarf LSB galaxy (Fig.2.24 (c)). This nearby galaxy does not show any distinctive central feature. Still, its surface brightness profile shows an exponential fit.

2.3.22 UGC 6614

This is one of the huge red LSB galaxies, which is comparable in size to Malin 2 ($\alpha \approx 12h^{-1}kpc$) (Fig.2.16). With a clear type 2 disk feature, it has a scale length of 5.2 kpc in the K_s-band, which is significantly shorter than in optical wavelengths. While lack of detection for outer disk regions might have contributed to it, it still shows its morphological features, which are nicely seen in optical bands.

2.3.23 UGC 8837

This amorphous LSB galaxy has an asymmetric structure, which has a broad plum-like feature southwest, while ending abruptly northeast (Fig.2.24 (d)). It still has a nice exponential disk with a shallow lump inside. There is an interesting feature just off the center northeast, which looks similar to a huge foreground dust band. However, this feature is not aligned with any structure of the galaxy and simply cuts the galaxy.

2.3.24 UGC 9992

This LSB galaxy shows a clear spiral arm feature, although an asymmetric one (Fig.2.24 (e)). An arm extends well northwest, while another arm fades very quickly southeast. It does not have any sign of a bulge or nucleus.

2.3.25 UGC 10310

This face-on LSB galaxy shows a very clear exponential disk while having big HII regions on its spiral arms (Fig.2.24 (f)). Although weak, it also suggests a thick feature inside, which makes this galaxy the Hubble type of SBb or SBc. While its disk is clearly shown, it looks very thin; more than a couple background galaxies show through it.

2.3.26 UGC 11454

This spiral galaxy shows two spiral arms very clearly, while its exponential disk has a comparable scale length of 4.25 kpc (Fig.2.17). This spiral galaxy probably does not qualify as an LSBG, if the stricter traditional standard ($\mu_B > 23$ mag arcsec^{-2}) is applied. With a small distinctive bulge, this galaxy can be categorized as Sc type even in the K_s-band.

2.3.27 UGC 11557

This face-on galaxy hints two spiral arms, while it has diffuse disk feature (Fig.2.25 (a)). It also has a very bright central structure, although it is not clear what exactly lies in its center in the K_s-band. However, the bright central feature is very elongated, which well matches available optical images with a clear bar-feature. It has a well-defined exponential disk.

2.3.28 UGC 11583

This edge-on galaxy has a very thin disk, while it has a very compact, relatively bright central structure (Fig.2.18). While it is difficult to discern any spiral feature from the K_s-band image, its surface brightness profile shows relatively clear type 2 disk.

2.3.29 UGC 11616

One of the brightest galaxies among the sample, this spiral galaxy shows every feature very clearly (Fig.2.19). With a relatively big bulge, one of its spiral arms has several big knots, which represent HII regions. While once regarded as a LSB galaxy, multiband observation suggest that this one with the central surface brightness in the K_s-band at 17.8 mag arcsec $^{-2}$ may not be one.

2.3.30 UGC 11648

Looking asymmetric, it is difficult to judge if it actually features an asymmetric extended disk or something else (Fig.2.25 (b)). It has a broad peak in its central region, while its extended feature southeast is very thin and irregular. It probably does not belong to the traditional LSBG category ($\mu_B > 23.5$ mag arcsec^{-2}) either.

2.3.31 UGC 11748

This is a well-defined, relatively big spiral galaxy (Fig.2.20). It has a big bulge inside and shows spiral arm feature with a small pitch angle, although it is not very distinctive. Its disk is a well-defined type 1 exponential disk.

2.3.32 UGC 11819

This is a well-defined spiral galaxy, which has a distinctive type-2 exponential disk (Fig.2.21). It has two clear spiral arms, which are diffused in the K_s-band and are difficult to detect. Star forming regions along the spiral arms are evident accross the bands (from B-band through K_s-band). While its spiral arms end at around 25 arcsec, it has an extended disk feature beyond them. It is not clear, though, if this feature is a part of spiral arm.

2.3.33 UGC 11820

This galaxy is an amorphous dwarf galaxy, which is just detected in K_s-band (Fig.2.25 (c)). This LSBG looks almost like a globular cluster, albeit very low, it has a central peak. It also shows a type-2 exponential disk. It is possible for this galaxy to be a typical LSBG, which looks like an amorphous smudge on the sky if given only a short exposure time.

2.3.34 UGC 11944

This LSBG looks amorphous while hinting that it may have thick disk feature (Fig.2.25 (d)). The K_s-band images represents an exponential disk with a dipped central region, however, optical band images from large surveys (e.g. DSS) suggest that the thick disk feature might be a bar from which two spiral arms begin. This galaxy may turn out to be type SBa with longer exposure.

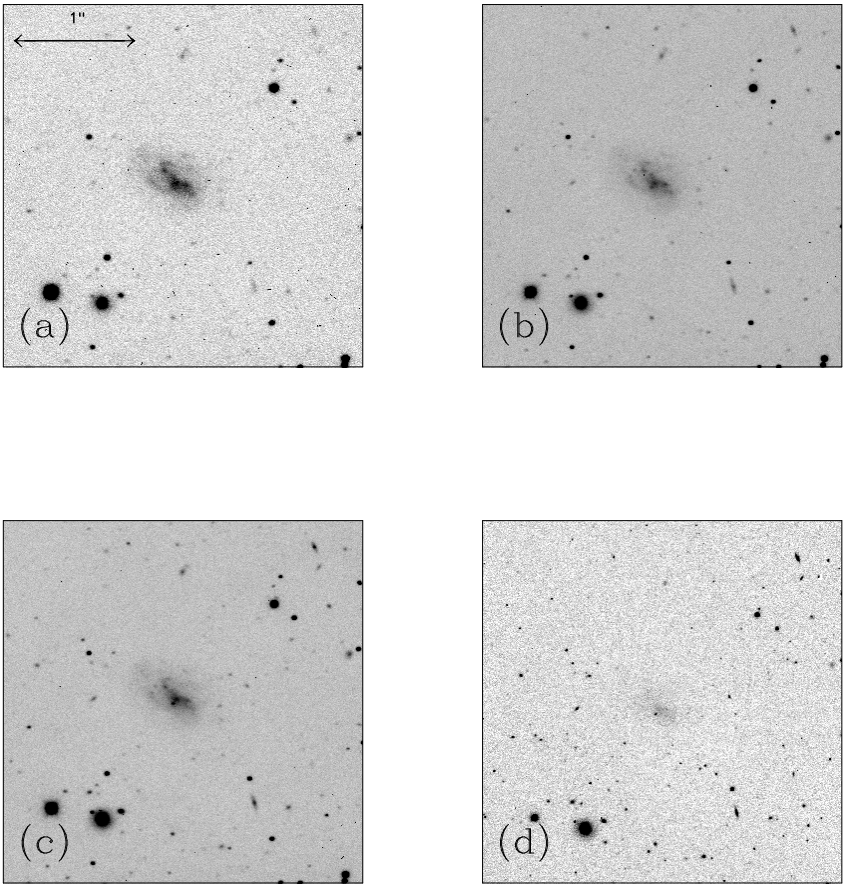

Figure 2.4: Images of D584-2. North is up and East is left. Intensity levels are adjusted arbitrarily in order to show the galaxy best. The bar on the upper left corner in (a) frame shows $1'$. (a) B (b) V (c) R (d) K_s
Three optical images are obtained with T2KA at KPNO 2.1-m telescope and the K_s-band images is obtained with FLMN at KPNO 4-m telescope.

2.3.35 UGC 12695

This LSBG looks like an amorphous knot in the K_s-band, while it shows some disk-like feature in the optical band images (Fig.2.22). In the these bands, it has a boomerang-shape, which has its opening eastward. Throughout the bands, it does not show any particular feature resembling a distinctive spiral arm.

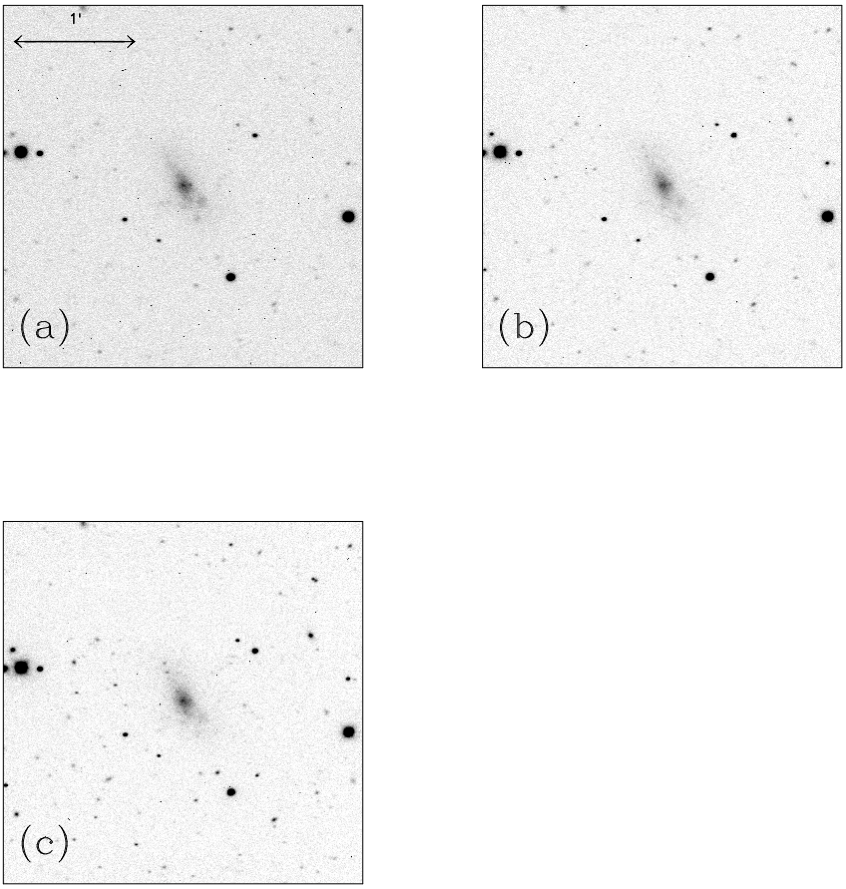

Figure 2.5: Images of D646-5. North is up and East is left. Intensity levels are adjusted arbitrarily in order to show the galaxy best. The bar on the upper left corner in (a) frame shows $1'$. (a) B (b) V (c) R Three optical images are obtained with T2KA at KPNO 2.1-m telescope.

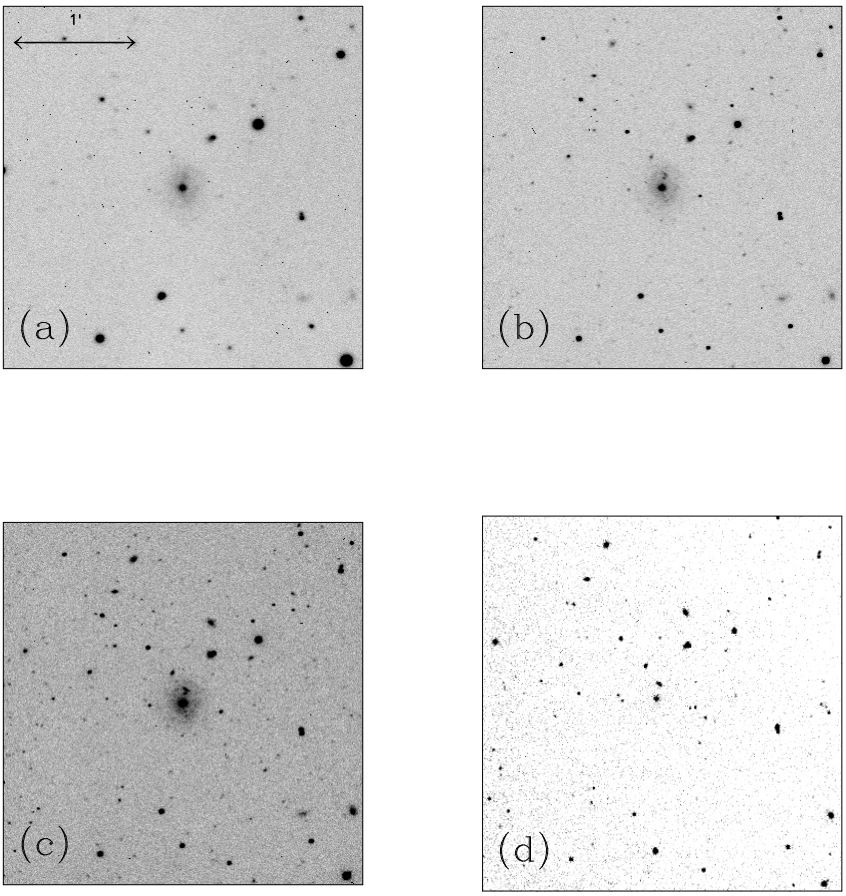

Figure 2.6: Images of D721-5. North is up and East is left. Intensity levels are adjusted arbitrarily in order to show the galaxy best. The bar on the upper left corner in (a) frame shows $1'$. (a) B (b) V (c) R (d) K_s Three optical images are obtained with T2KA at KPNO 2.1-m telescope and the K_s-band images is obtained with FLMN at KPNO 4-m telescope.

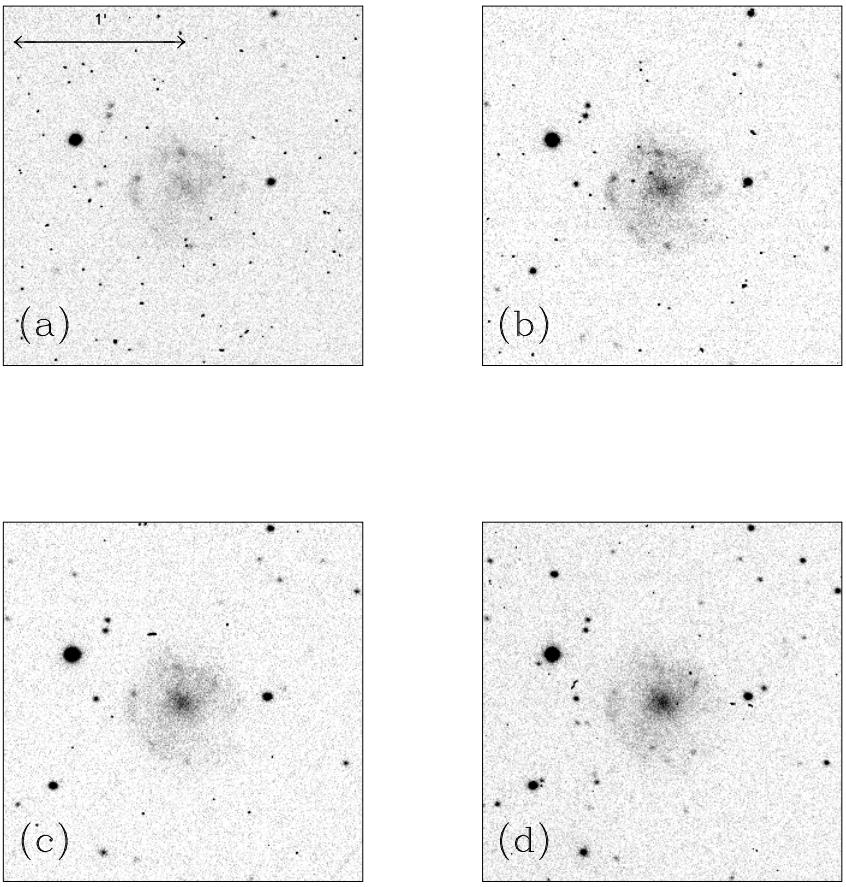

Figure 2.7: Images of F561-1. North is up and East is left. Intensity levels are adjusted arbitrarily in order to show the galaxy best. The bar on the upper left corner in (a) frame shows $1'$. (a) U (b) B (c) V (d) I These optical images are from McGaugh et al. (1995b).

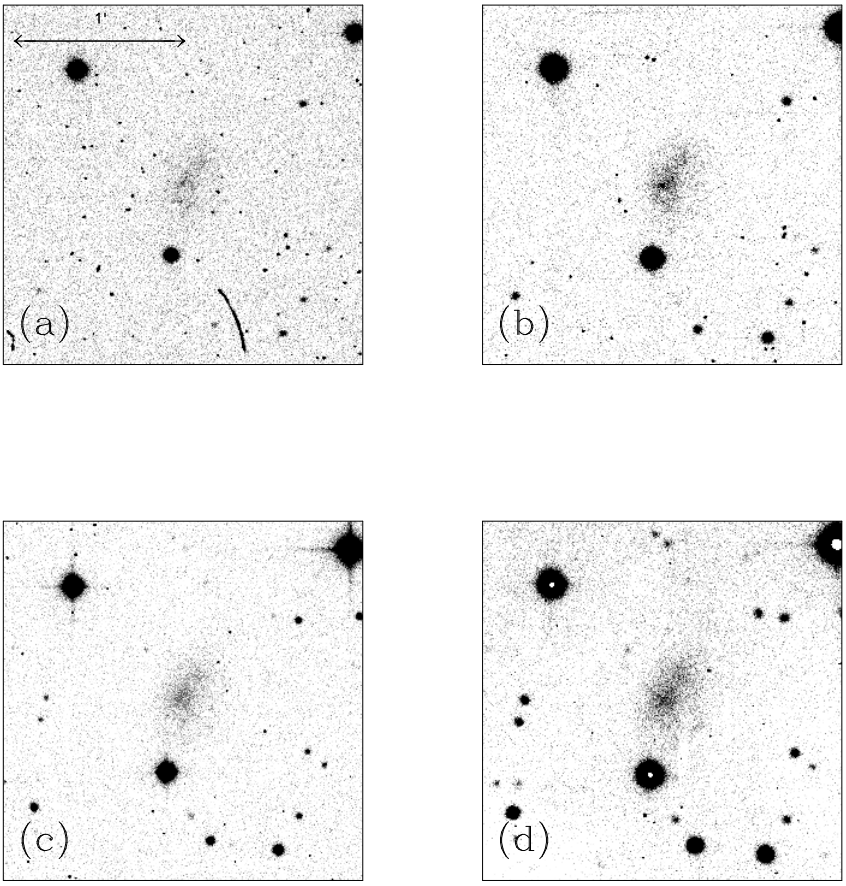

Figure 2.8: Images of F563-V1. North is up and East is left. Intensity levels are adjusted arbitrarily in order to show the galaxy best. The bar on the upper left corner in (a) frame shows $1'$. (a) U (b) B (c) V (d) I These optical images are from McGaugh et al. (1995b).

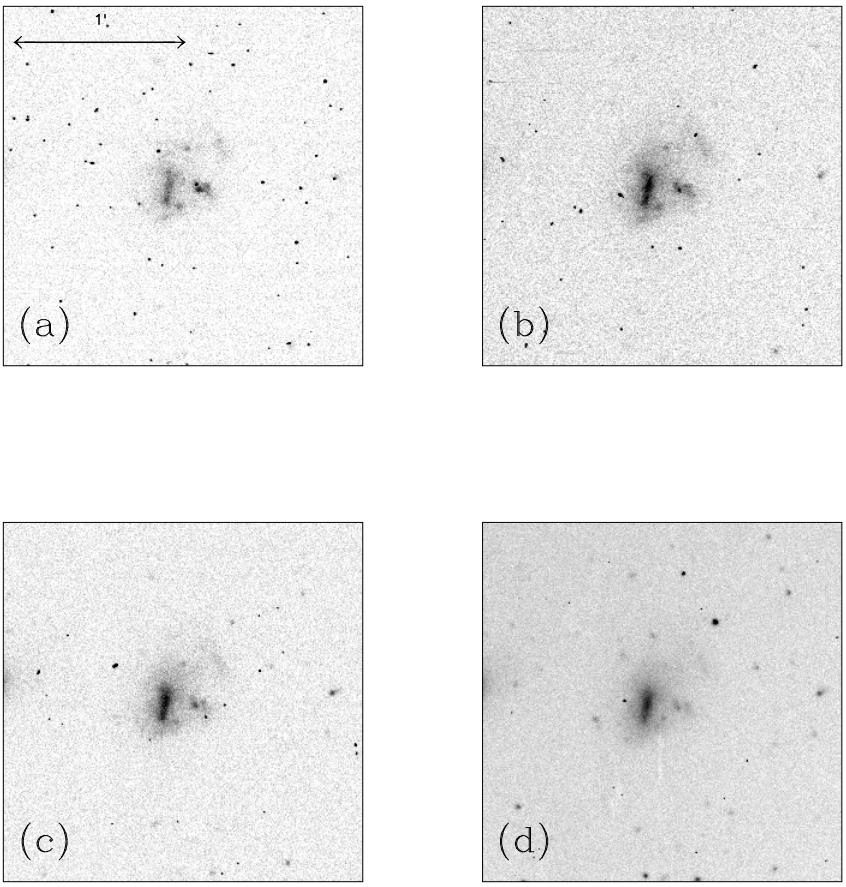

Figure 2.9: Images of F563-V2. North is up and East is left. Intensity levels are adjusted arbitrarily in order to show the galaxy best. The bar on the upper left corner in (a) frame shows 1′. (a) U (b) B (c) V (d) I These optical images are from McGaugh et al. (1995b).

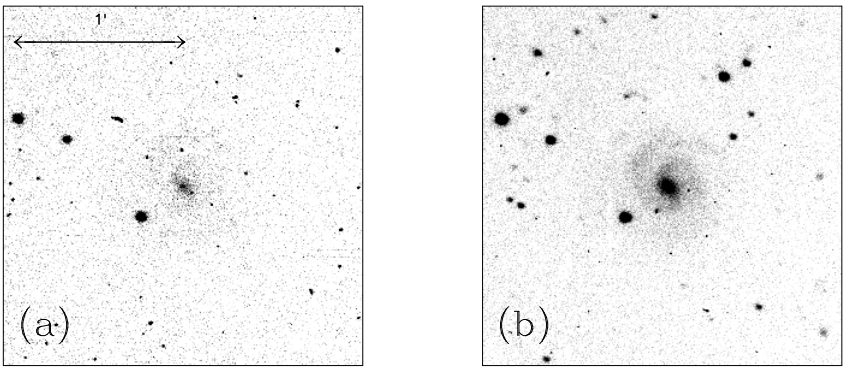

Figure 2.10: Images of F568-1. North is up and East is left. Intensity levels are adjusted arbitrarily in order to show the galaxy best. The bar on the upper left corner in (a) frame shows 1′. (a) B (b) I Two optical images are from McGaugh et al. (1995b)

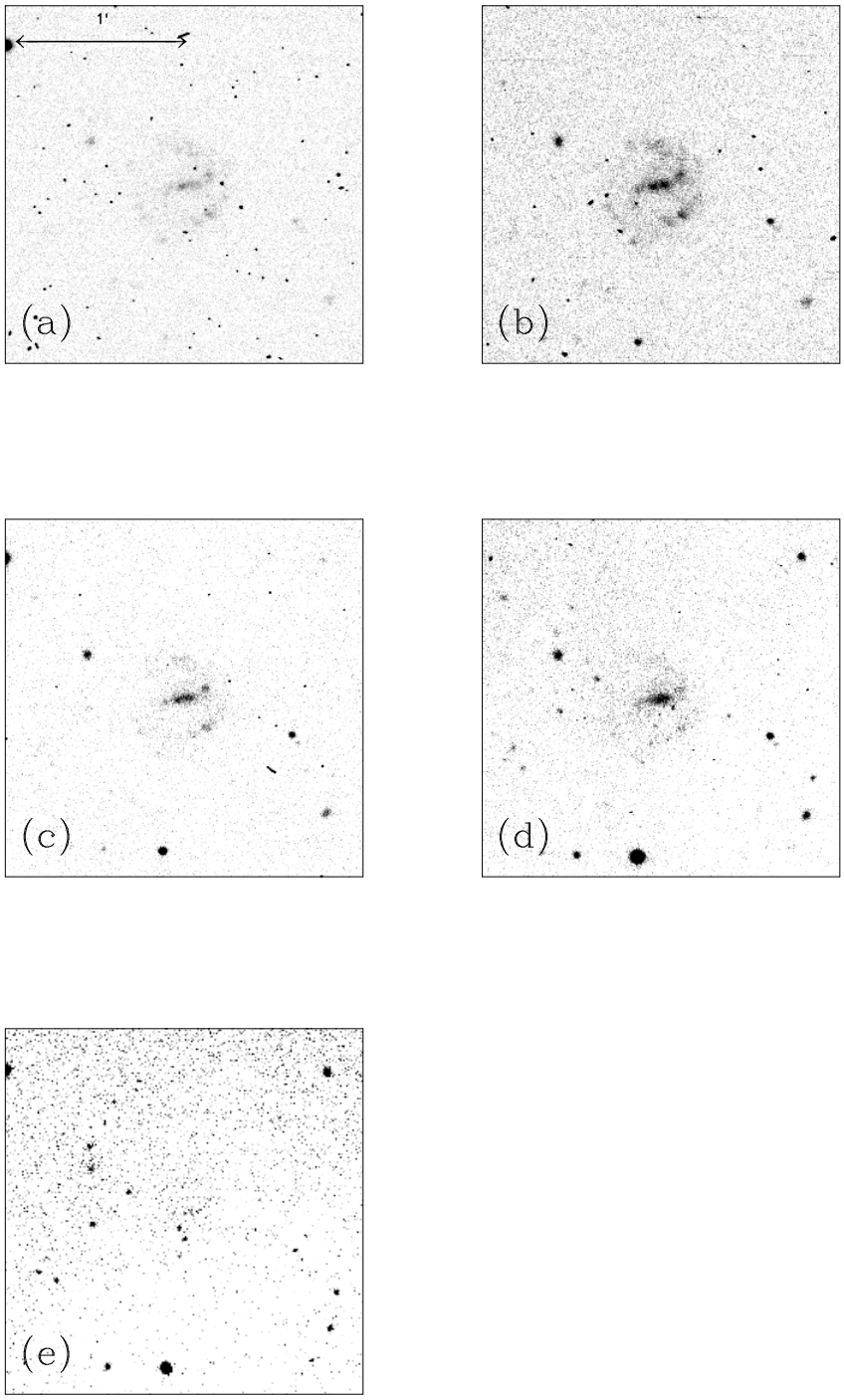

Figure 2.11: Images of F577-V1. North is up and East is left. Intensity levels are adjusted arbitrarily in order to show the galaxy best. The bar on the upper left corner in (a) frame shows $1'$. (a) U (b) B (c) V (d) I (e) K_s Four optical images are from McGaugh et al. (1995b) and the K_s-band image is obtained with FLMN at KPNO 4-m telescope.

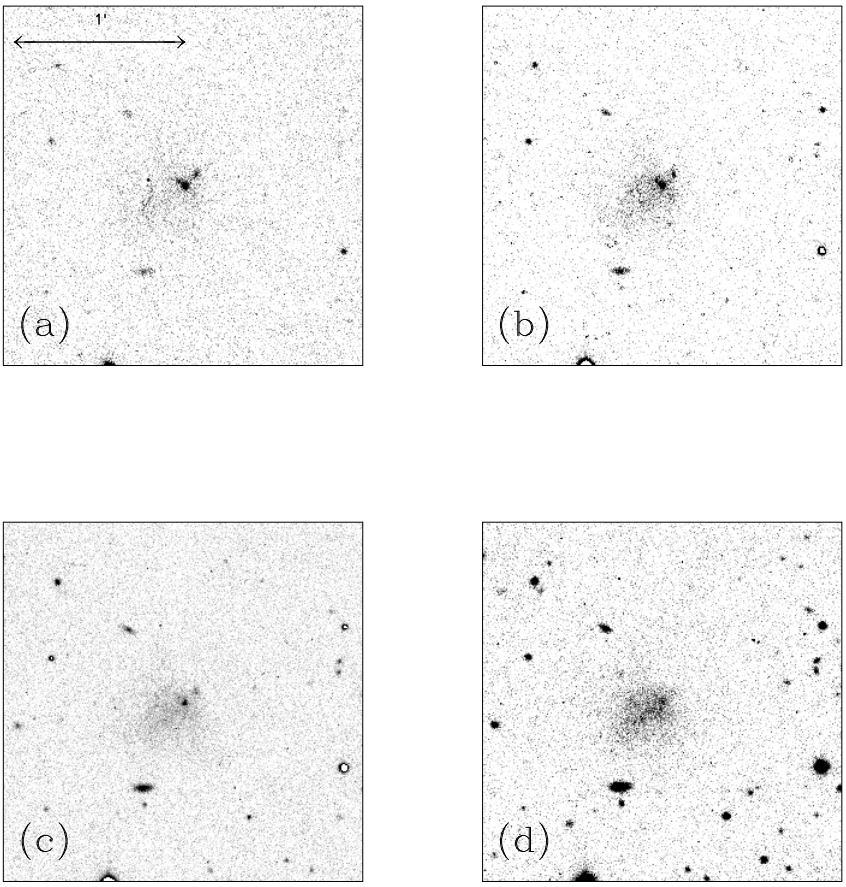

Figure 2.12: Images of F611-1. North is up and East is left. Intensity levels are adjusted arbitrarily in order to show the galaxy best. The bar on the upper left corner in (a) frame shows $1'$. (a) U (b) B (c) V (d) I These optical images are from McGaugh et al. (1995b).

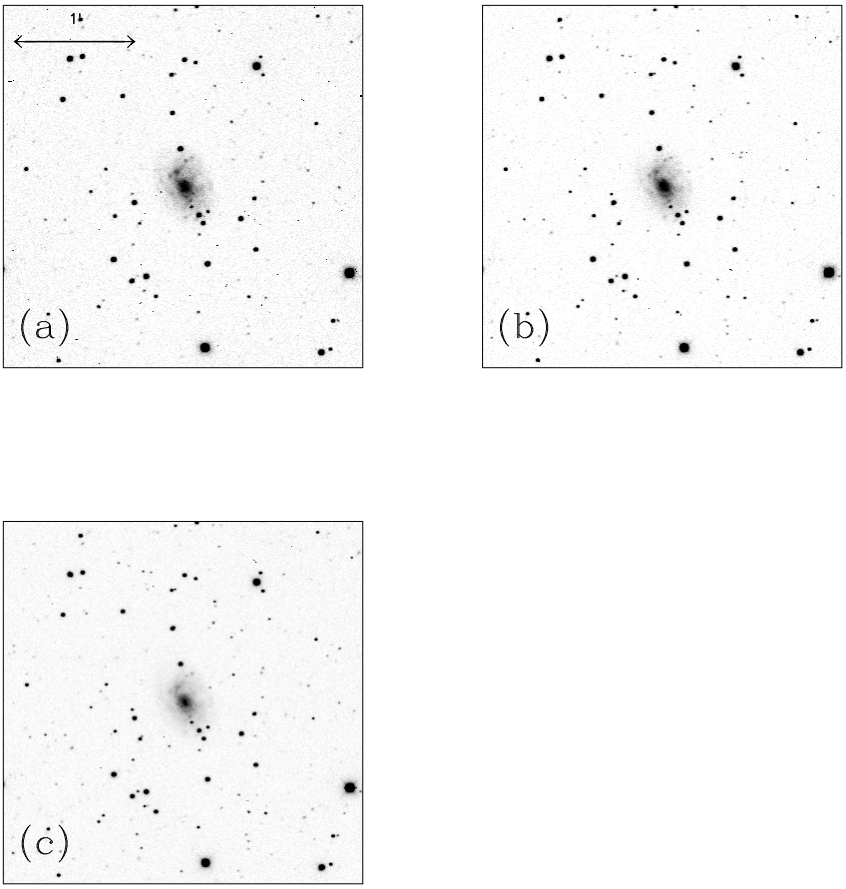

Figure 2.13: Images of F730-V1. North is up and East is left. Intensity levels are adjusted arbitrarily in order to show the galaxy best. The bar on the upper left corner in (a) frame shows $1'$. (a) B (b) V (c) R These optical images are obtained with T2KA at KPNO 2.1-m telescope.

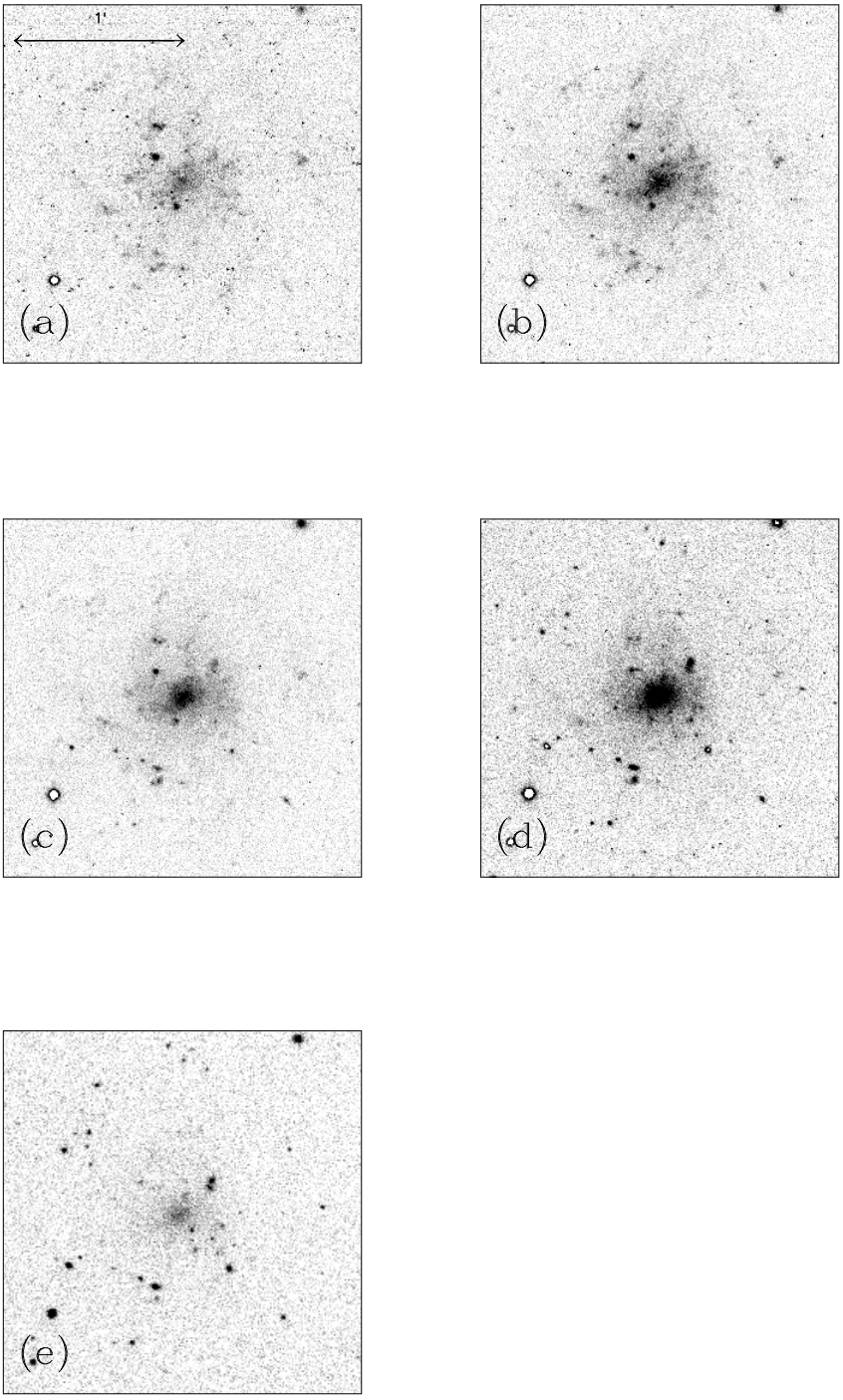

Figure 2.14: Images of UGC 1230. North is up and East is left. Intensity levels are adjusted arbitrarily in order to show the galaxy best. The bar on the upper left corner in (a) frame shows $1'$. (a) U (b) B (c) V (d) I (e) K_s Four optical images are from McGaugh et al. (1995b) and the K_s-band image is obtained with FLMN at KPNO 4-m telescope.

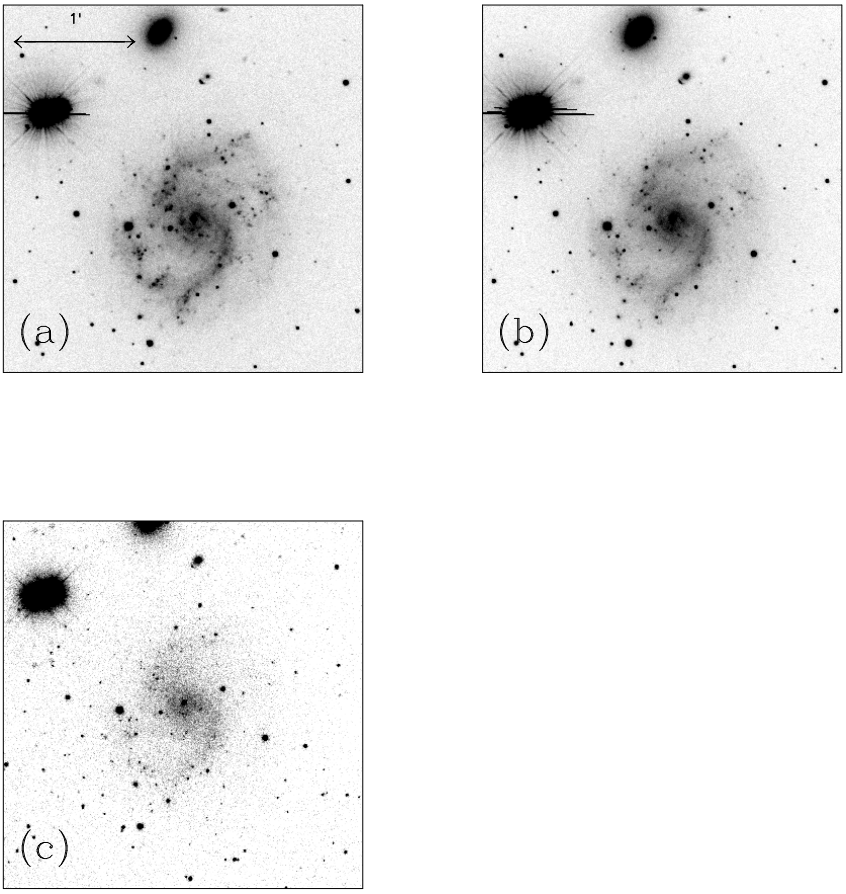

Figure 2.15: Images of UGC 2259. North is up and East is left. Intensity levels are adjusted arbitrarily in order to show the galaxy best. The bar on the upper left corner in (a) frame shows $1'$. (a) B (b) R (c) K_s Two optical images are obtained with T2KA at KPNO 2.1-m telescope by Kuzio de Naray and the K_s-band image is is obtained with FLMN at KPNO 4-m telescope.

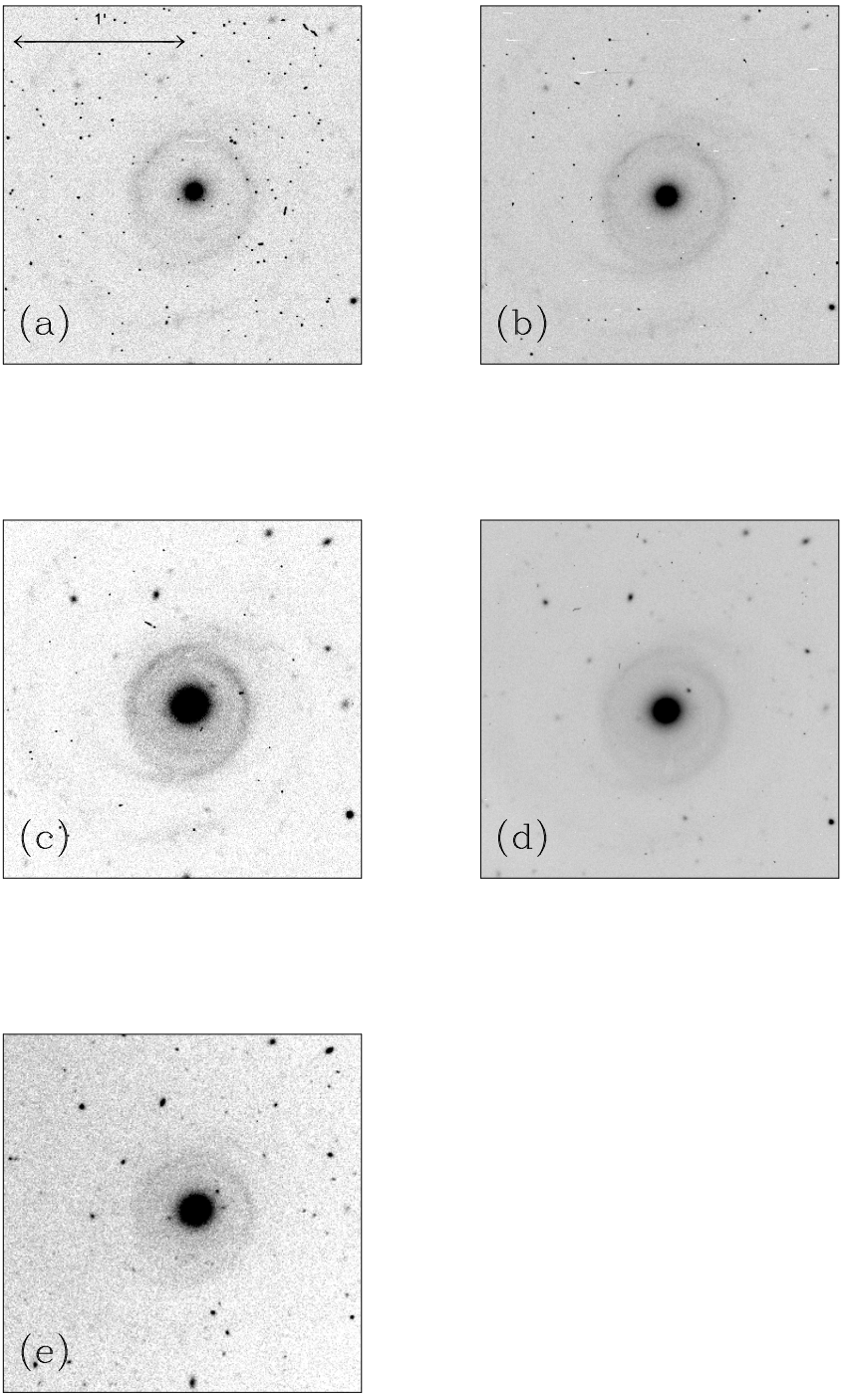

Figure 2.16: Images of UGC 6614. North is up and East is left. Intensity levels are adjusted arbitrarily in order to show the galaxy best. The bar on the upper left corner in (a) frame shows $1'$. (a) U (b) B (c) V (d) I (e) K_s Four optical images are from McGaugh et al. (1995b) and the K_s-band image is obtained with FLMN at KPNO 4-m telescope.

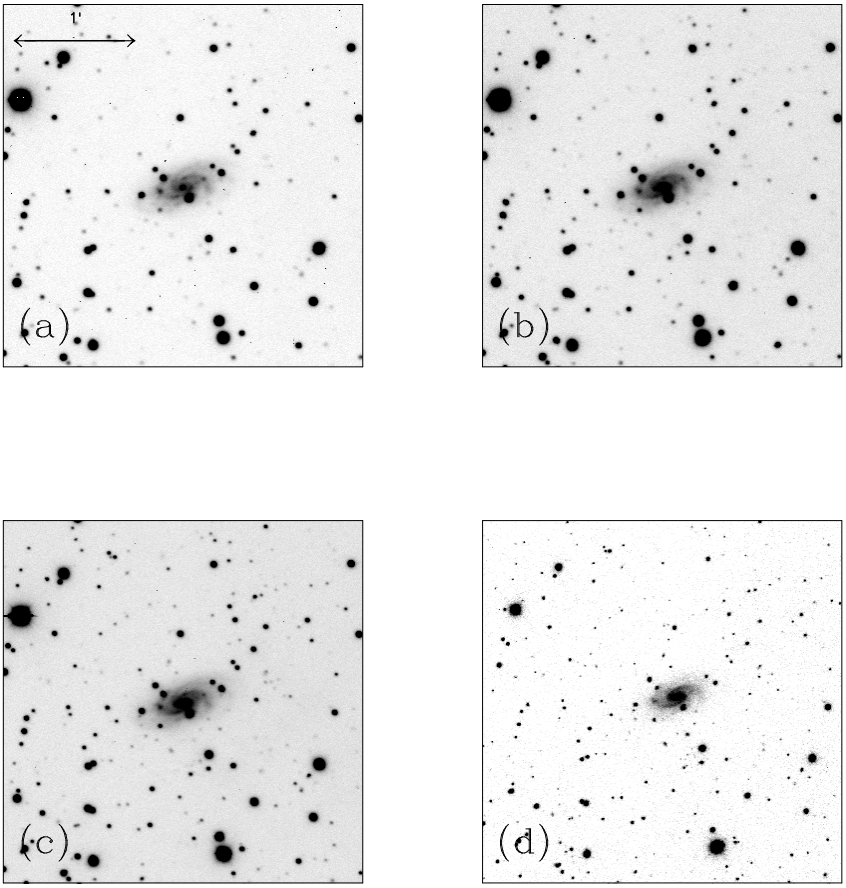

Figure 2.17: Images of UGC 11454. North is up and East is left. Intensity levels are adjusted arbitrarily in order to show the galaxy best. The bar on the upper left corner in (a) frame shows $1'$. (a) B (b) V (c) R (d) K_s Three optical images are obtained with T2KA at KPNO 2.1-m telescope and the K_s-band image is obtained with FLMN at KPNO 4-m telescope.

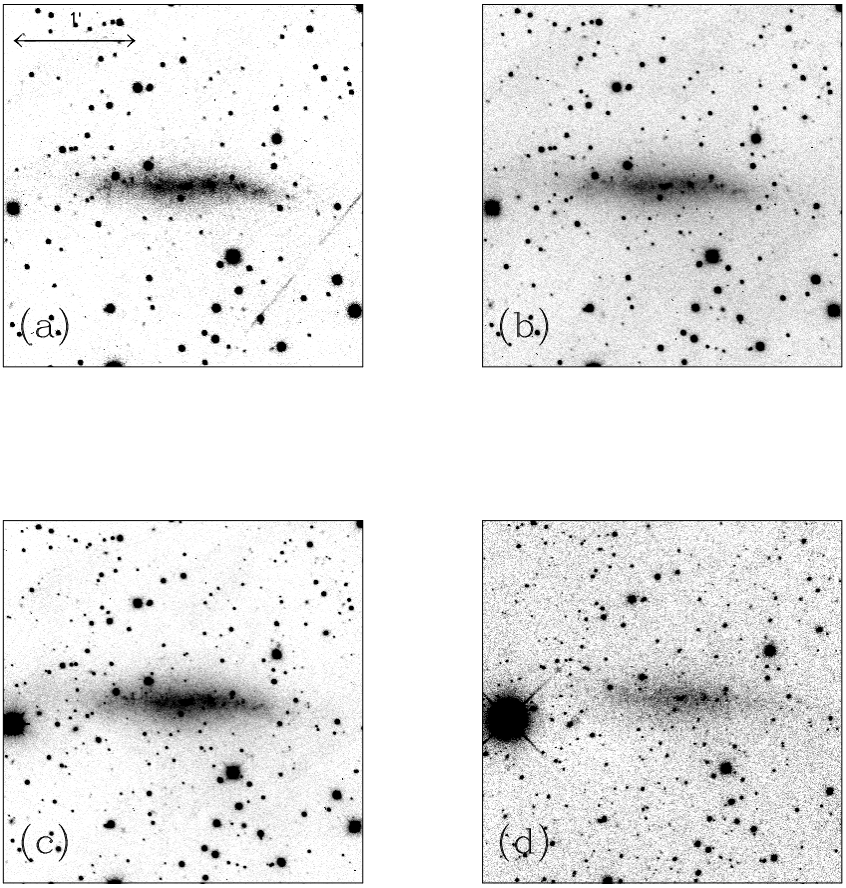

Figure 2.18: Images of UGC 11583. North is up and East is left. Intensity levels are adjusted arbitrarily in order to show the galaxy best. The bar on the upper left corner in (a) frame shows $1'$. (a) B (b) V (c) R (d) K_s Three optical images are obtained with T2KA at KPNO 2.1-m telescope and the K_s-band image is obtained with FLMN at KPNO 4-m telescope.

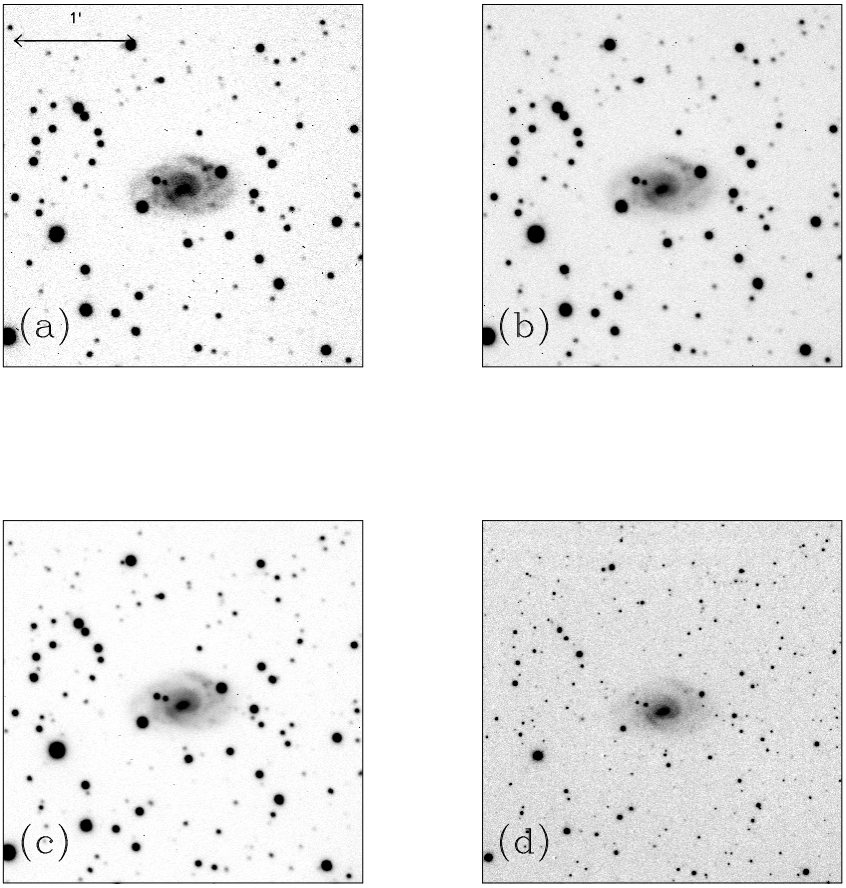

Figure 2.19: Images of UGC 11616. North is up and East is left. Intensity levels are adjusted arbitrarily in order to show the galaxy best. The bar on the upper left corner in (a) frame shows $1'$. (a) B (b) V (c) R (d) K_s Three optical images are obtained with T2KA at KPNO 2.1-m telescope and the K_s-band image is obtained with FLMN at KPNO 4-m telescope.

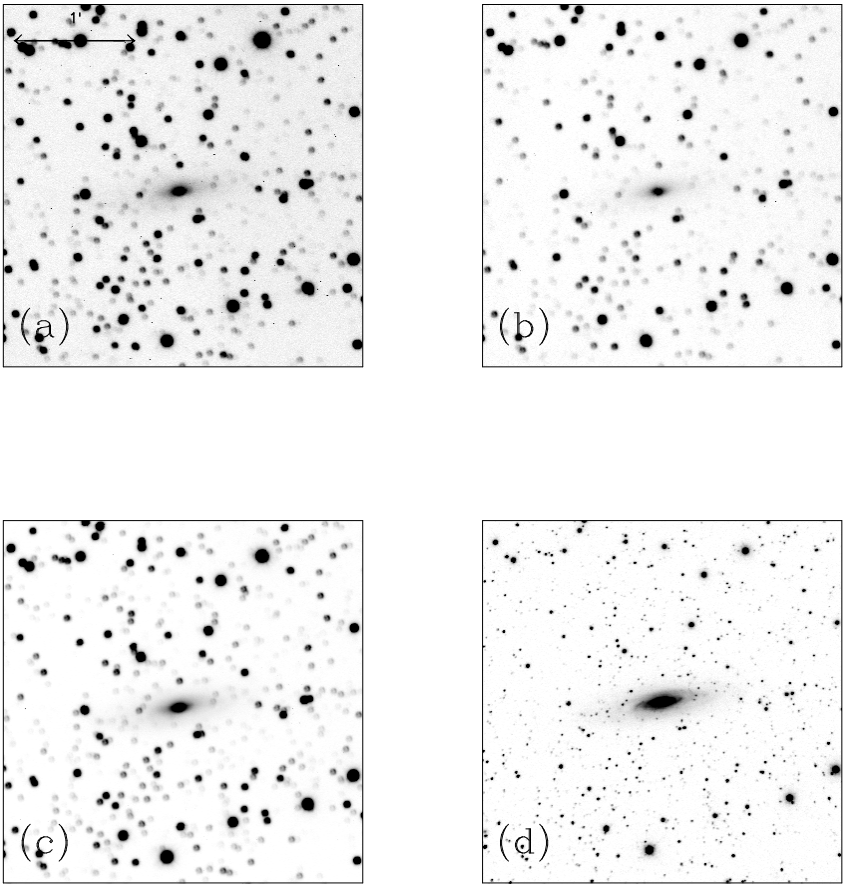

Figure 2.20: Images of UGC 11748. North is up and East is left. Intensity levels are adjusted arbitrarily in order to show the galaxy best. The bar on the upper left corner in (a) frame shows $1'$. (a) B (b) V (c) R (d) K_s Three optical images are obtained with T2KA at KPNO 2.1-m telescope and the K_s-band image is obtained with FLMN at KPNO 4-m telescope.

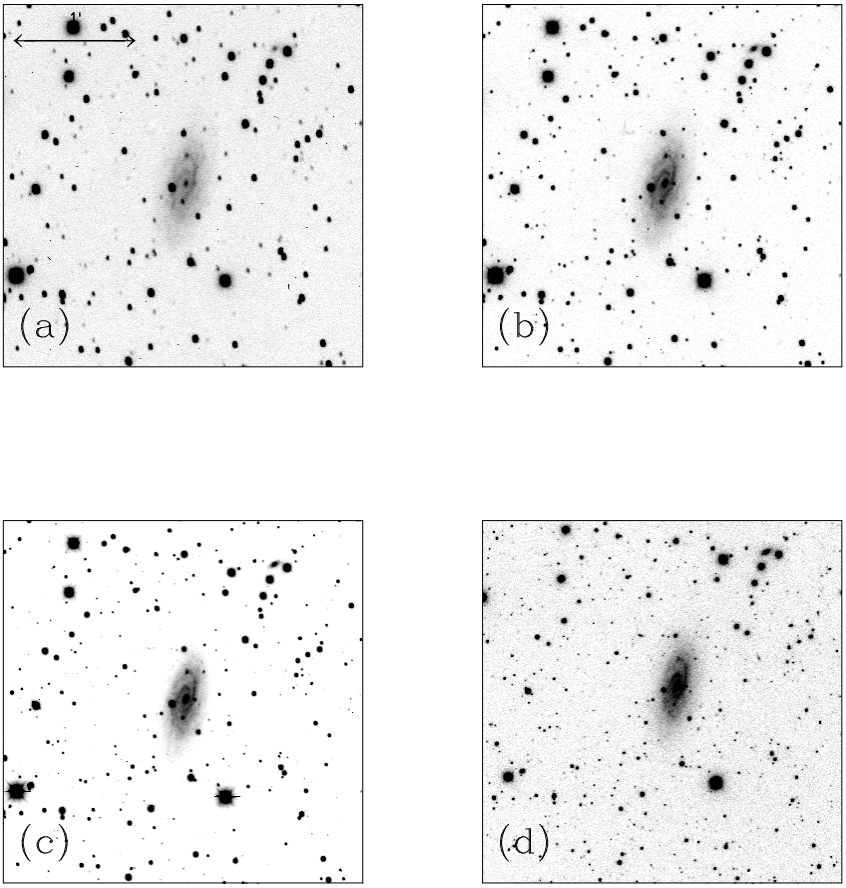

Figure 2.21: Images of UGC 11819. North is up and East is left. Intensity levels are adjusted arbitrarily in order to show the galaxy best. The bar on the upper left corner in (a) frame shows $1'$. (a) B (b) V (c) R (d) K_s Three optical images are obtained with T2KA at KPNO 2.1-m telescope and the K_s-band image is obtained with FLMN at KPNO 4-m telescope.

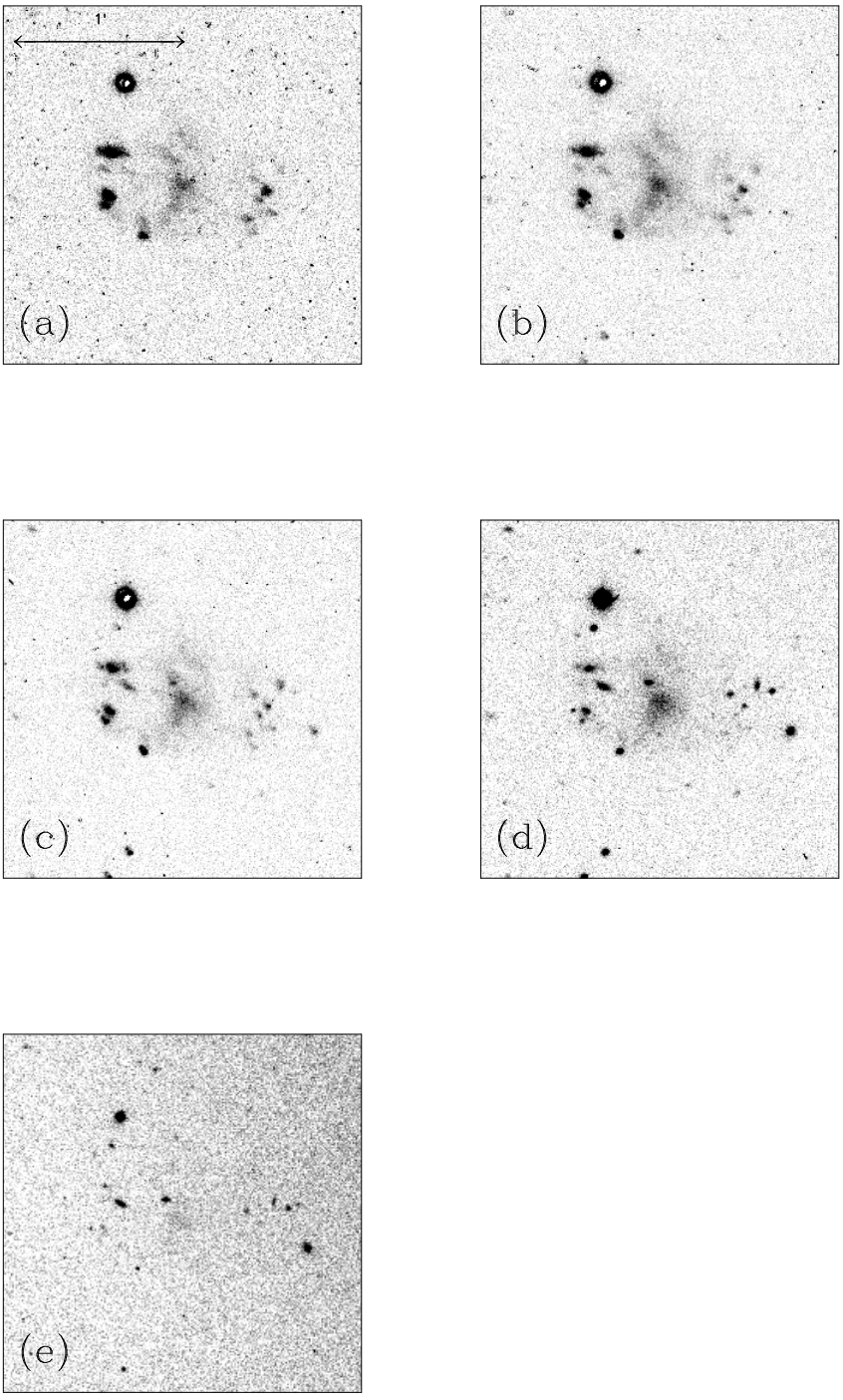

Figure 2.22: Images of UGC 12695. North is up and East is left. Intensity levels are adjusted arbitrarily in order to show the galaxy best. The bar on the upper left corner in (a) frame shows $1'$. (a) U (b) B (c) V (d) I (e) K_s Four optical images are from McGaugh et al. (1995b) and the K_s-band image is obtained with FLMN at KPNO 4-m telescope.

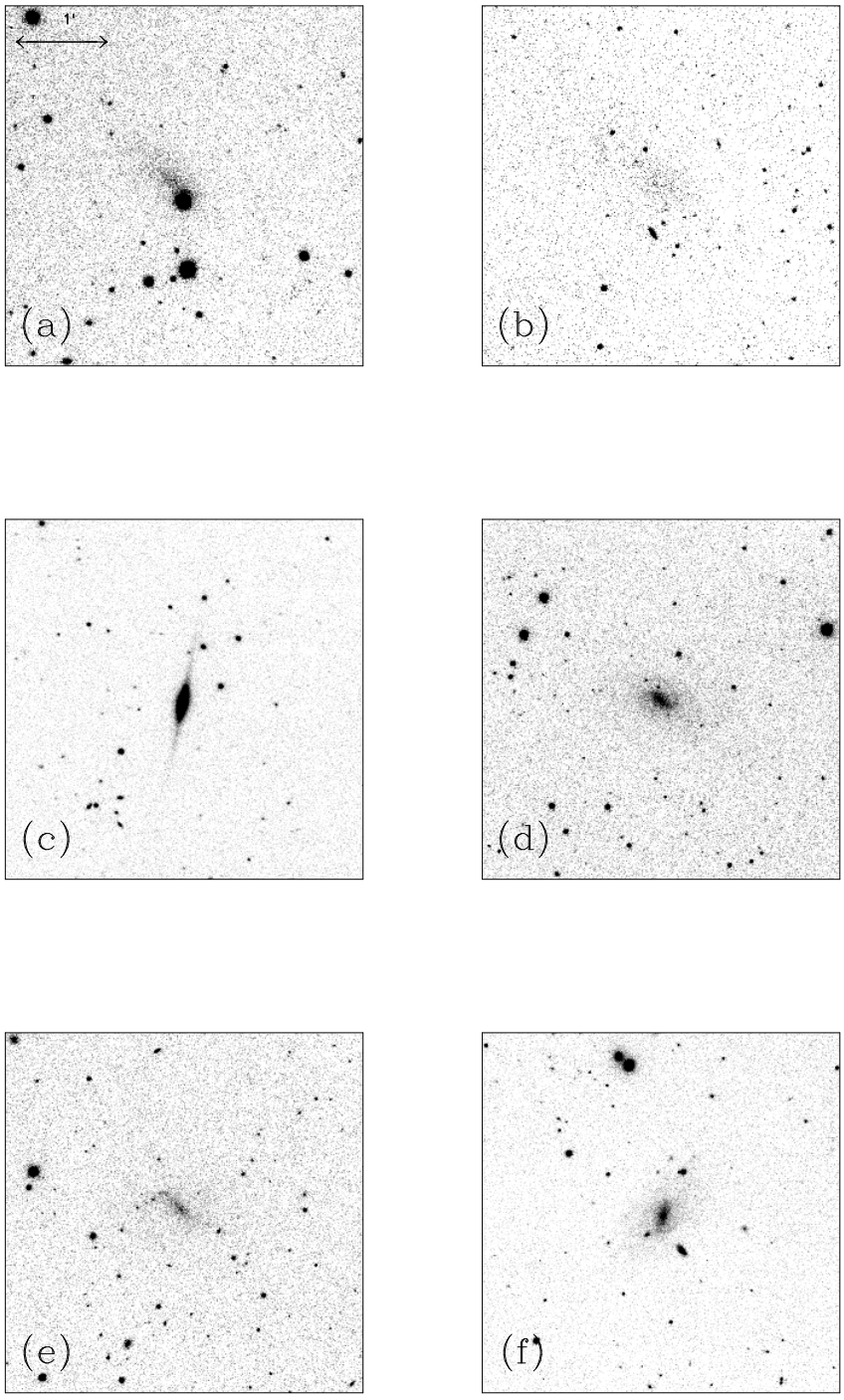

Figure 2.23: K_s-band images of sample galaxies without optical images. North is up and East is left. Intensity levels are adjusted arbitrarily in order to show the galaxy best. The bar on the upper left corner in (a) frame shows $1'$ and linear sizes are same for every image. (a) D512-2 (b) D575-2 (c) F571-8 (d) UGC 128 (e) UGC 334 (f) UGC 628

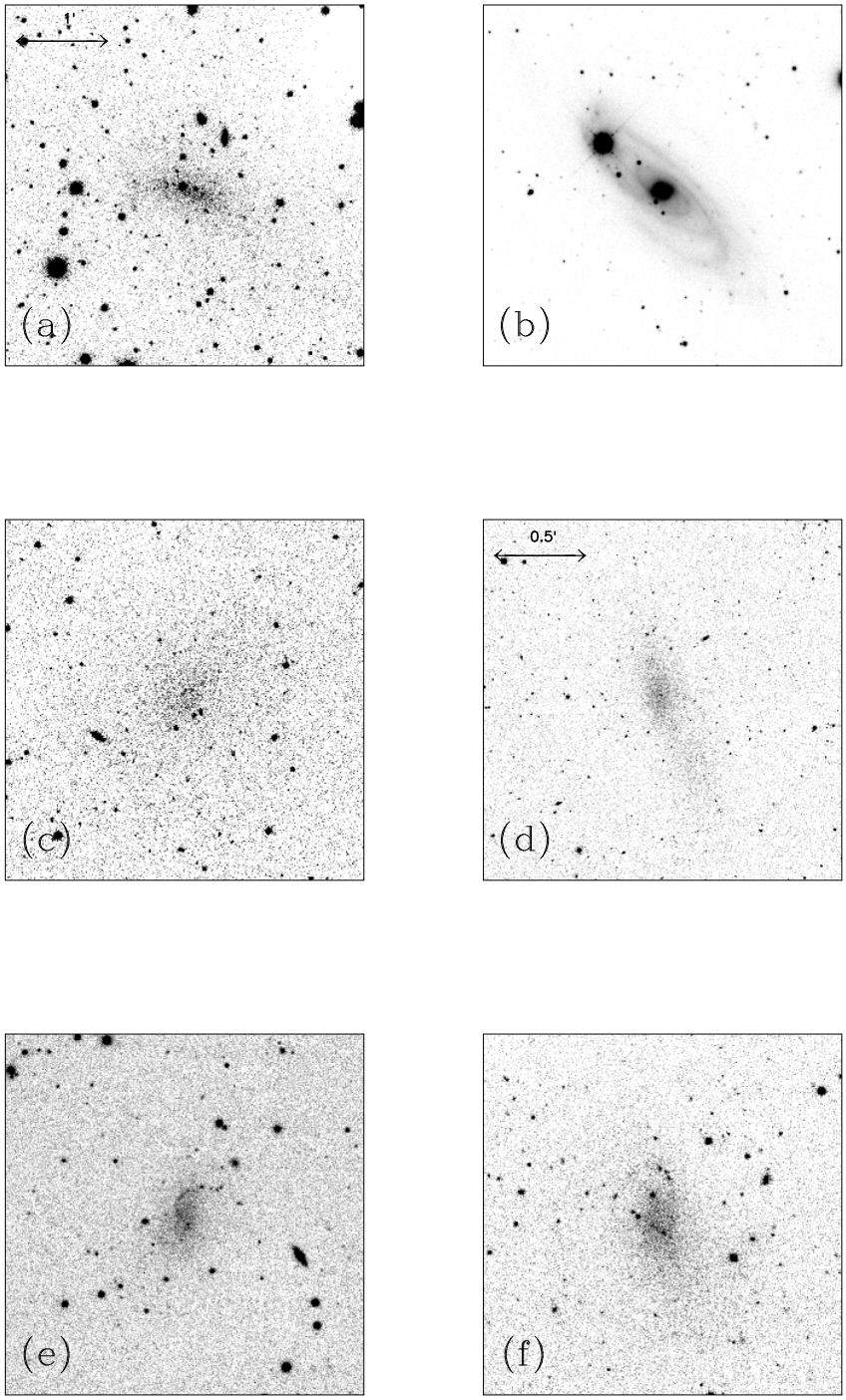

Figure 2.24: Another K_s-band image set for sample galaxies without optical images. North is up and East is left. Intensity levels are adjusted arbitrarily in order to show the galaxy best. The bar on the upper left corner in (a) frame shows $1'$ and linear sizes are same for every image, except (d) UGC 8837. For UGC 8837, the bar on the upper left corner indicates $0.5'$. (a) UGC 731 (b) UGC 2885 (c) UGC 3371 (d) UGC 8837 (e) UGC 9992 (f) UGC 10310

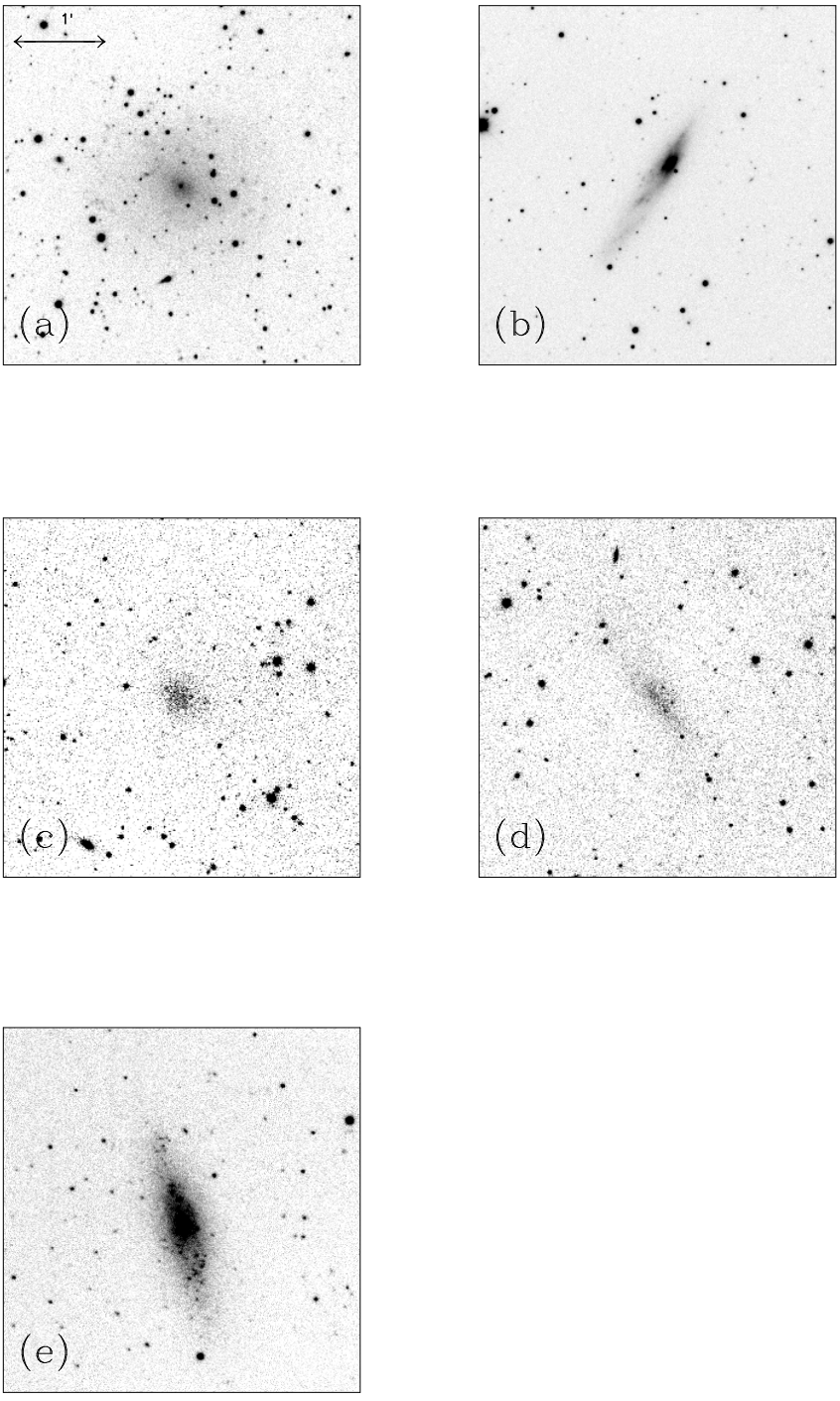

Figure 2.25: Final K_s-band image set for sample galaxies without optical images. North is up and East is left. Intensity levels are adjusted arbitrarily in order to show the galaxy best. The bar on the upper left corner in (a) frame shows $1'$. (a) UGC 11557 (b) UGC 11648 (c) UGC 11820 (d) UGC 11944 (e) NGC 4455

2.4 Surface Photometry

2.4.1 Methodology

Surface photometry is carried out by ARCHANGEL package, which was developed by Dr. J. Schombert for surface photometry of galaxies (Schombert 2007). ARCHANGEL enables one to perform quick and precise surface photometry automatically.

When ARCHANGEL decides centers of sample galaxies in image frames, it evaluates sky values depending on parameters, such as grid sizes, and σ values for object detection. Once ARCHANGEL estimates sky values, then it generates *clean* images by eliminating foreground and background stars, background galaxies, and other non-factor objects. Then it runs ellipse fitting, which resembles ELLIPSE task from IRAF. While ELLIPSE task required you to decide many options before running properly, ARCHANGEL generally provides reliable automated fitting through several available options. Once surface photometry profiles are produced by ARCHANGEL, exponential disk profiles are eye-fitted. Then, basic parameters, such as total magnitude, exponential disk scale length, and central surface brightness are measured. Exponential disk fits on sample galaxies are described and discussed in the following sections in detail.

2.4.2 Error Analysis

There are four possible error sources for our surface photometry. The first one is erroneous photometric calibration. Photometry on standard stars and photometric zeropoint fitting can cause offsets. Typically photometry on standard stars does not issue a big error. For our optical and NIR photometry, this is generally smaller

than 0.01 mag. Since recursive least-square fitting uses this error, we do not have to consider this error separately. Photometric zeropoint fitting involves airmass and colors. Since our NIR images were acquired during a wide range of airmass, we decided to pick averages of photometric zeropoints for NIR photometry. Errors are less than 0.05 mag. With recursive fitting, photometric zeropoints for optical runs have even smaller errors, less than 0.02 mag.

Another measurement error is from isophote measurement. ARCHANGEL provides measurement errors of isophotes which it generates. These errors are standard deviations along borders of isophotes. These errors become bigger toward outer ellipses since skybackground become dominant in outer regions.

However, the biggest source of error is sky uncertainty. de Jong (1996) claimed that sky subtraction is very important to the practice of bulge/disk decomposition. With intensive simulations and tests, MacArthur et al. (2003) confirmed that sky uncertainty provides the biggest error in studies of surface photometry. Our method to measure skybackground was as following. We put multiple (typically around 20) boxes around our target galaxies. Bright objects were generally masked out beforehand, or median values were chosed instead of averages. For NIR images which we subtracted skybackground, we measure these averages from sky frames, instead of target galaxy frames. Then we calculated standard deviations of those averages of boxes. We take these standard deviations as our skybackground errors.

Table 2.4. Results of Surface Photometry

Galaxy	Band	m_T	M_T	μ_0	μ_0^{cor}	h^1	h^2	A_λ^3
D512-2	V[a]		-16.96	21.1			0.5	
	I[a]		-17.76					
	K_s	11.649	-18.67	19.7	20.5±0.01	8.9	0.5±0.05	0.006
D575-2	U[b]		-15.26±0.04					
	B[b]		-15.14±0.01					
	V[b]		-15.560±0.02	23.66±0.09			1.56±0.07	
	K_s	15.840	-14.32	21.2	22.0±0.08	38	2.0±0.23	0.014
D575-5	U[b]		-12.79±0.04					
	B[b]		-12.65±0.01					
	V[b]		-12.85±0.03	24.69±0.09			1.56±0.07	
D584-2	B	16.707	-16.10	23.55	24.1±0.02	5.94	1.05±0.05	0.297
	V	16.612	-16.20	22.71	23.2±0.02	7.80	1.38±0.05	0.228
	R	18.902	-13.91	22.3	22.8±0.03	9.33	1.65±0.15	0.184
	K_s	15.037	-17.775	20.1	20.6±0.25	6.22	1.1±0.21	0.025
D584-4	U[b]		-17.26±0.05					
	B[b]		-16.89±0.01					
	V[b]		-17.17±0.02	23.35±0.06			2.53±0.06	
D646-5	B	16.678	-14.08	23.3	24.2±0.01	9.5	0.65±0.02	0.132
	V	16.624	-14.13	22.75	23.6±0.01	8.7	0.6±0.02	0.101
	R	16.168	-14.59	22.4	23.3±0.02	9.5	0.65±0.05	0.082
D646-7	U[b]		-12.70±0.02					
	B[b]		-12.25±0.01					
	V[b]		-12.53±0.02	21.72±0.20			0.15±0.01	
D721-5	B	18.037	-16.50	23.15	23.6±0.07	4.68	1.83±0.09	0.111
	V	17.011	-17.52	22.25	22.7±0.07	4.80	1.88±0.10	0.085
	R	16.699	-17.84	21.95	22.35±0.09	5.75	2.25±0.11	0.069
	K_s	16.304	-18.23	20.95	21.35±0.19	7.54	2.95±0.30	0.009
F561-1	U	15.489	-18.601	23.45	23.55±0.10	17.1	5.53±0.23	0.253
	B	16.505	-17.585	23.45	23.55±0.09	12.5	4.05±0.18	0.201
	V	16.052	-18.038	23.05	23.15±0.09	11.4	3.7±0.22	0.154
	I	14.802	-19.288	22.35	22.45±0.11	14.6	4.73±0.46	0.090
F563-V1	U	17.705	-15.925	24.15	24.9±0.05	13.5	3.53±0.16	0.141
	B	18.189	-15.441	23.55	24.3±0.05	10.9	2.85±0.12	0.112
	V	16.869	-16.761	23.35	24.1±0.04	9.35	2.45±0.08	0.086
	I	15.453	-18.177	22.35	23.1±0.08	8.97	2.35±0.22	0.050
F563-V2	U	13.107	-20.749	23.35	23.5±0.08	11.4	3.3±0.35	0.091
	B	16.922	-16.934	22.3	22.4±0.07	10.2	2.95±0.29	0.072
	V	16.191	-17.665	22.35	22.5±0.07	10.0	2.9±0.27	0.055
	I	14.929	-18.927	21.0	21.15±0.12	7.9	2.3±0.41	0.032
F568-1	B	16.443	-18.313	23.65	23.7±0.08	12.5	5.25±0.35	0.083
	I	15.616	-19.140	21.15	21.3±0.12	10.2	4.5±0.41	0.037
	K_s	13.103	-21.68	19.9	20.0±0.12	9.8	4.3±0.35	0.007
F571-8	K_s	13.047	-20.53	18.95	18.95±0.05	11.3	2.85±0.27	0.009
F577-V1	U	17.293	-17.848	22.05	22.3±0.03	3.2	1.65±0.21	0.123
	B	17.172	-17.969	22.08	22.3±0.01	6.8	3.55±0.16	0.097
	V	17.062	-18.079	21.65	21.9±0.02	2.9	1.5±0.27	0.075
	I	15.617	-19.524	20.15	20.4±0.01	3.6	1.9±0.13	0.044
	K_s	17.914	-17.26	20.15	20.4±0.03	1.9	1.0±0.21	0.008
F611-1	U	16.494	-15.89	22.68	22.9±0.03	14.4	2.1±0.09	0.490
	B	15.394	-16.99	23.68	23.9±0.02	11.3	1.65±0.08	0.389
	V	13.924	-18.46	23.35	23.6±0.02	12.0	1.75±0.07	0.299
	I	16.727	-15.66	23.25	23.5±0.05	10.3	1.5±0.13	0.175
F730-V1	B	16.642	-19.224	22.35	22.8±0.03	9.6	6.9±0.25	0.435
	V	16.009	-19.857	21.75	22.2±0.02	8.3	6.0±0.27	0.334
	R	15.590	-20.276	21.35	21.8±0.02	8.1	5.85±0.30	0.269
NGC 4455	K_s	10.069	-24.67	18.4	20.0±0.02	24.5	1.05±0.03	0.008

Table 2.4 (cont'd)

Galaxy	Band	m_T	M_T	μ_0	μ_0^{cor}	h^1	h^2	A_λ^3
UGC 128	U^e	15.0±0.2	-19.00	23.96±0.15		32±6		
	B^e	15.16±0.05	-18.84	23.55±0.05		24±0.6		
	V^e	14.50±0.05	-19.50	22.94±0.02		25±0.5		
	R^e	14.35±0.05	-19.65	22.50±0.01		22±0.01		
	I^e	14.06±0.05	-19.94	22.09±0.04		21±0.3		
	K_s	11.298	-22.70	19.1	19.95±0.05	7.05	2.15±0.18	0.023
UGC 334	B^e	15.4±0.3	-18.64	23.5±0.1		25±10		
	V^e	14.7±0.3	-19.34	22.6±0.2		23±11		
	R^e	14.4±0.3	-19.64	22.3±0.2		21±7		
	I^e	14.4±0.2	-19.64	21.9±0.1		17±3		
	K_s	10.594	-23.45	19.55	19.65±0.07	8.7	2.7±0.27	0.020
UGC 628	U^e	15.5±0.1	-18.89	23.0±0.1		17±1		
	B^e	15.6±0.1	-18.79	23.1±0.1		17±2		
	V^e	15.1±0.1	-19.29	22.55±0.05		16.5±0.7		
	R^e	14.7±0.1	-19.69	22.14±0.05		16.0±0.3		
	I^e	14.2±0.05	-20.19	21.65±0.02		15.2±0.3		
	K_s	10.382	-24.01	18.65	19.25±0.01	6.1	2.25±0.04	0.016
UGC 731	U^b		-17.44±0.02					
	B^b		-17.12±0.01					
	V^b		-17.46±0.02	23.33±0.04			3.09±0.08	
	K_s	10.192	-19.55	19.1	21.45±0.06	8.4	0.36±0.06	0.051
UGC 1230	U	14.915	-18.686	21.35	21.45±0.02	7.9	2.05±0.14	0.627
	B	16.111	-17.490	21.65	21.75±0.01	7.6	1.95±0.09	0.498
	V	15.573	-18.028	21.05	21.15±0.01	7.4	1.9±0.07	0.382
	I	14.627	-18.974	20.0	20.1±0.01	5.8	1.5±0.05	0.224
	K_s	9.711	-21.04	19.15	19.25±0.01	5.2	1.35±0.06	0.042
UGC 2259	B	13.809	-15.703	22.7	23.0±0.02	40.8	1.6±0.05	0.315
	R	12.489	-17.023	21.5	21.8±0.02	39.5	1.55±0.06	0.195
	K_s	9.133	-20.41	19.5	19.85±0.04	19.1	0.75±0.10	0.027
UGC 2885	B^d		-22.80	22.0			13.0	
	V		-23.27					
	K_s	8.067	-26.26	17.55	18.35	42.2	16.5	0.073
UGC 3371	U^c	13.60	-16.68					
	B^c	13.71±0.19	-16.56±0.19	24.21			3.65	
	V^c	13.05	-17.23					
	K_s	10.435	-19.84	20.65	21.10±0.04	11.5	0.63±0.05	0.054
UGC 6614	U	16.249	-18.451	21.6	21.8±0.23	9.4	4.0±0.35	0.153
	B	14.781	-19.919	21.3	21.5±0.15	14.7	6.3±0.27	0.122
	V	13.406	-21.294	20.35	20.55±0.15	8.5	3.65±0.30	0.094
	I	11.377	-23.323	19.1	19.3±0.24	8.7	3.7±0.29	0.055
	K_s	10.741	-23.99	18.2	18.4±0.25	11.5	4.9±0.36	0.010
UGC 8837	U^b		-14.74±0.02					
	B^b		-14.47±0.01					
	V^b		-14.95±0.01	22.87±0.05			0.79±0.01	
	K_s	10.581	-17.28	20.15	21.9±0.01	33.0	0.60±0.02	0.005
UGC 9992	U^c	14.54	-15.18					
	B^c	14.70±0.10	-15.02±0.10	22.84			0.71	
	V^c	14.33	-15.39					
	K_s	12.640	-17.08	19.4	19.6±0.01	9.7	0.41±0.01	0.013
UGC 10310	U^b		-17.54±0.01					
	B^b		-17.20±0.01					
	V^b		-17.58±0.01	22.30±0.11			1.74±0.10	
	K_s	10.714	-19.27	20.05	20.25±0.02	37.3	1.8±0.04	0.004
UGC 11454	B	14.022	-20.80	21.4	22.25±0.03	9.0	4.0±0.23	0.422
	V	13.050	-21.77	20.55	21.4±0.02	9.0	4.0±0.13	0.324
	R	12.792	-22.03	20.3	21.15±0.01	10.1	4.5±0.28	0.261

Table 2.4 (cont'd)

Galaxy	Band	m_T	M_T	μ_0	μ_0^{cor}	h^1	h^2	A_λ^3
	K_s	10.604	-24.22	17.8	18.65±0.02	7.4	3.3±0.20	0.036
UGC 11557	K_s	9.742	-21.69	18.88	19.10±0.01	45.4	4.25±0.02	0.087
UGC 11583	B	14.668	-14.183	22.3	24.30±0.01	32.7	0.28±0.01	1.319
	V	14.667	-14.184	21.65	24.65±0.01	29.2	0.25±0.01	1.013
	R	13.369	-15.481	21.3	23.3±0.01	36.2	0.31±0.01	0.817
	K_s	11.679	-17.172	19.85	21.85±0.01	21.0	0.18±0.01	0.112
UGC 11616	B	13.581	-20.73	21.55	22.3±0.04	17.0	6.0±0.08	1.497
	V	13.102	-21.21	20.85	21.6±0.04	15.3	5.4±0.09	1.150
	R	12.734	-21.58	20.25	21.0±0.05	13.9	4.9±0.12	0.927
	K_s	10.387	-23.92	17.85	18.6±0.07	8.5	3.0±0.14	0.127
UGC 11648	K_s	10.394	-22.95	17.25	19.25±0.02	16.8	3.8±0.04	0.199
UGC 11748	B	12.394	-21.93	22.75	24.6±0.03	8.5	3.0±0.15	2.757
	V	11.764	-22.56	21.45	23.3±0.02	9.7	3.43±0.13	2.118
	R	11.30	-23.02	20.40	22.25±0.05	8.8	3.13±0.15	1.708
	K_s	10.071	-24.25	15.3	17.15±0.04	7.1	2.5±0.18	0.234
UGC 11819	B	14.226	-19.605	21.5	22.45±0.03	22.7	6.5±0.19	1.731
	V	13.557	-20.274	20.65	21.6±0.03	19.9	5.7±0.22	1.330
	R	13.202	-20.629	20.1	21.05±0.03	18.5	5.3±0.24	1.072
	K_s	10.800	-23.06	17.85	18.8±0.04	15.7	4.5±0.25	0.147
UGC 11820	U^b		-17.41±0.02					
	B^b		-17.17±0.01					
	V^b		-17.56±0.02	23.64±0.07			3.50±0.10	
	K_s	12.235	-18.70	19.65	20.1±0.02	43.0	3.2±0.03	0.046
UGC 11944	U^c	14.74	-17.17					
	B^c	14.92±0.09	-16.99	24.30			4.32	
	V^c	14.50		-17.41				
	K_s	11.413	-20.50	20.2	21.45±0.03	11.6	1.35±0.10	0.017
UGC 12695	U	16.739	-17.901	21.85	22.3±0.01	4.9	2.05±0.12	0.316
	B	17.370	-17.27	22.05	22.5±0.01	5.3	2.20±0.11	0.251
	V	17.084	-17.556	21.65	21.95±0.01	4.3	1.80±0.09	0.193
	I	17.145	-17.495	21.05	21.5±0.02	4.9	2.05±0.12	0.130
	K_s	12.500	-22.17	21.35	21.8±0.05	3.2	1.35±0.11	0.021

Note. — Col.(1): Galaxy name Col.(2): Band Col.(3) : Apparent total magnitude Col.(4) : Absolute total magnitude Col.(5) : Central surface brightness only corrected for galactic extinction Col.(6) : Central surface brightness corrected for galactic extinction and inclination Col.(7) : Disk scale length in arcsec Col.(8) : Disk scale length in kpc Col.(9) : Galactic extinction from NED based on Schlegel et al. (1998)
Reference :(a)Pildis et al. (1997) (b)Hunter & Elmegreen (2006) (c)van Zee (2001) (d)Chattopadhyay & Chattopadhyay (2006)

2.4.3 Structure of Sample Galaxies

For disk galaxies, an exponential disk profile is generally fit in the form of

$$\Sigma(r) = \Sigma_0 e^{-r/\alpha}, \tag{2.20}$$

while their inner regions are fit using the de Vaucouleurs $r^{1/4}$ profile

$$\Sigma(r) = \Sigma_e e^{-7.67[(r/r_e)-1]}. \tag{2.21}$$

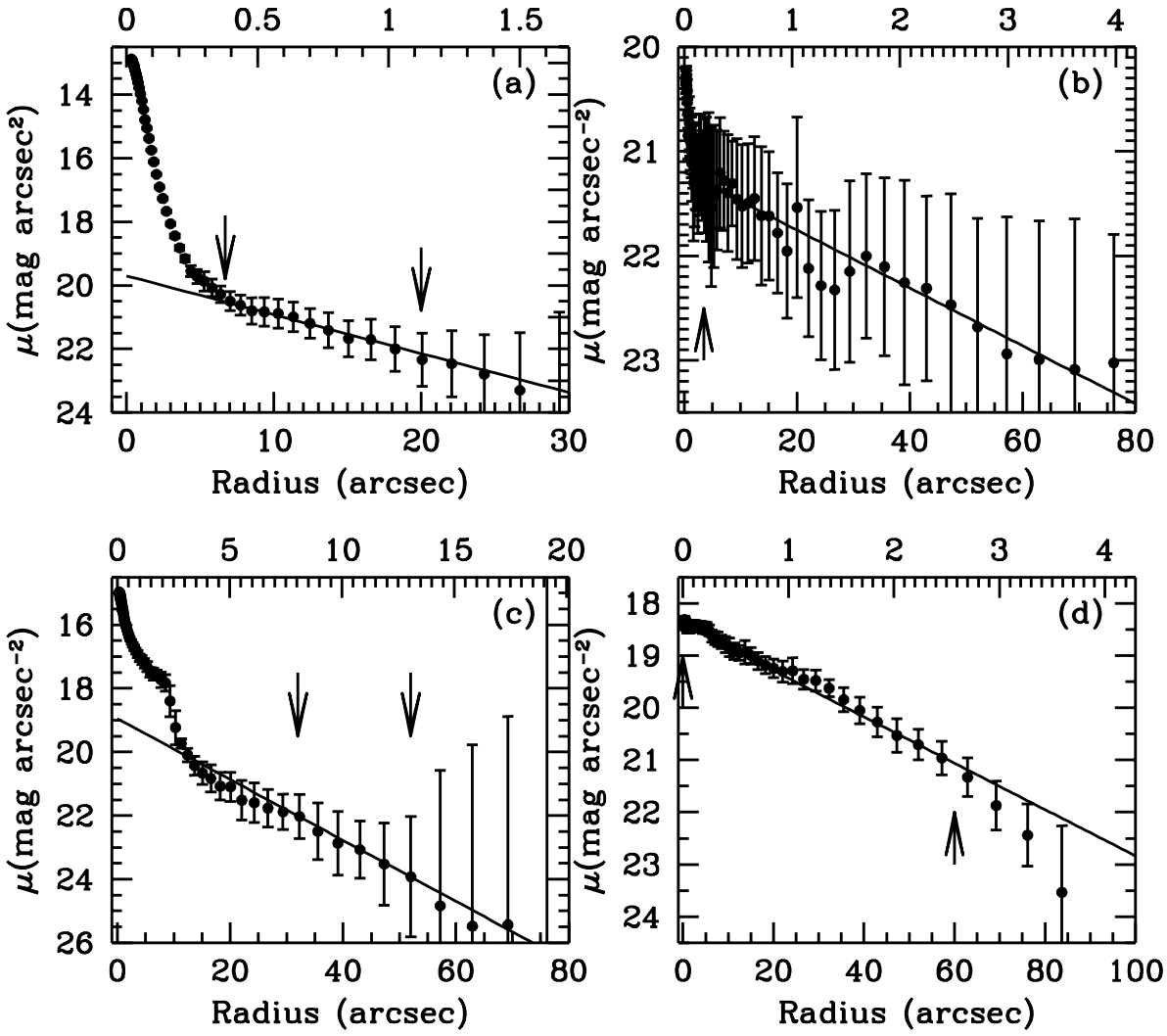

Figure 2.26: K_s-band surface photometry profiles of sample galaxies (a) D512-2 (b) D575-2 (c) F571-8 (d) NGC 4455. Upper x-axis is in kpc. Arrows indicate profile portions where exponential disk fitting is performed.

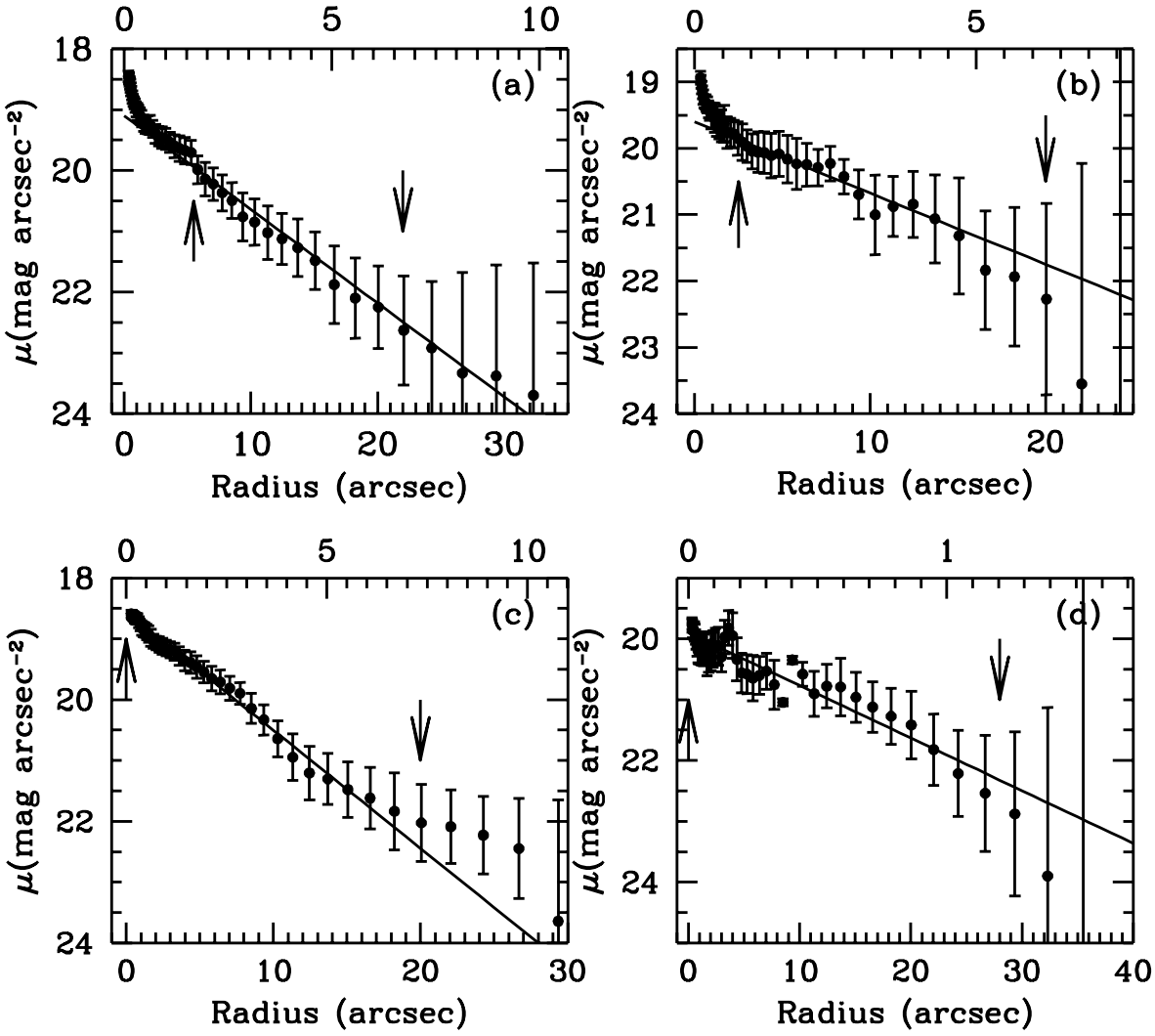

Figure 2.27: K_s-band surface photometry profiles of sample galaxies (a) UGC 128 (b) UGC 334 (c) UGC 628 (d) UGC 731. Arrows indicate profile portions where exponential disk fitting is performed.

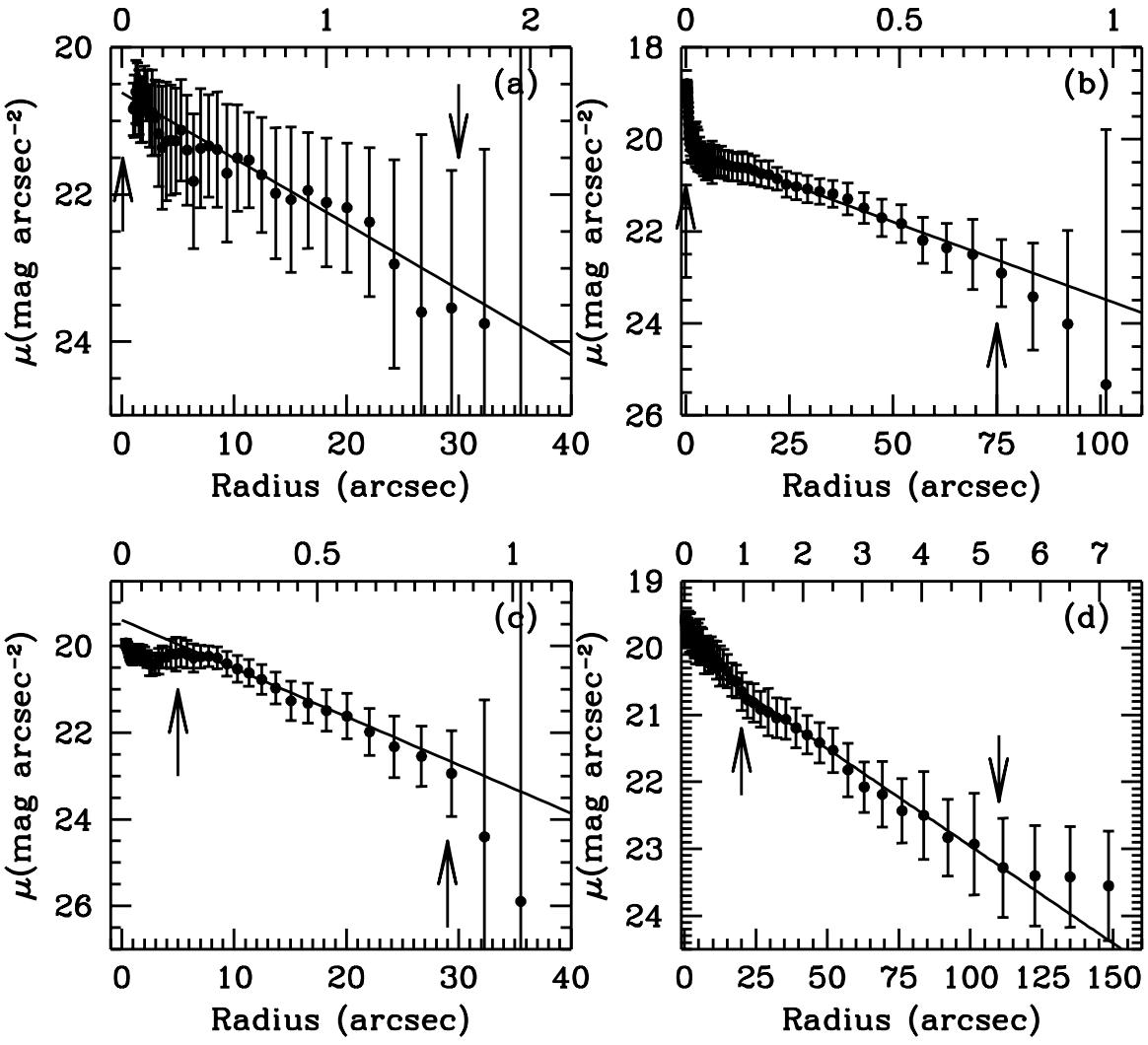

Figure 2.28: K_s-band surface photometry profiles of sample galaxies (a) UGC 3371 (b) UGC 8837 (c) UGC 9992 (d) UGC 10310. Arrows indicate profile portions where exponential disk fitting is performed.

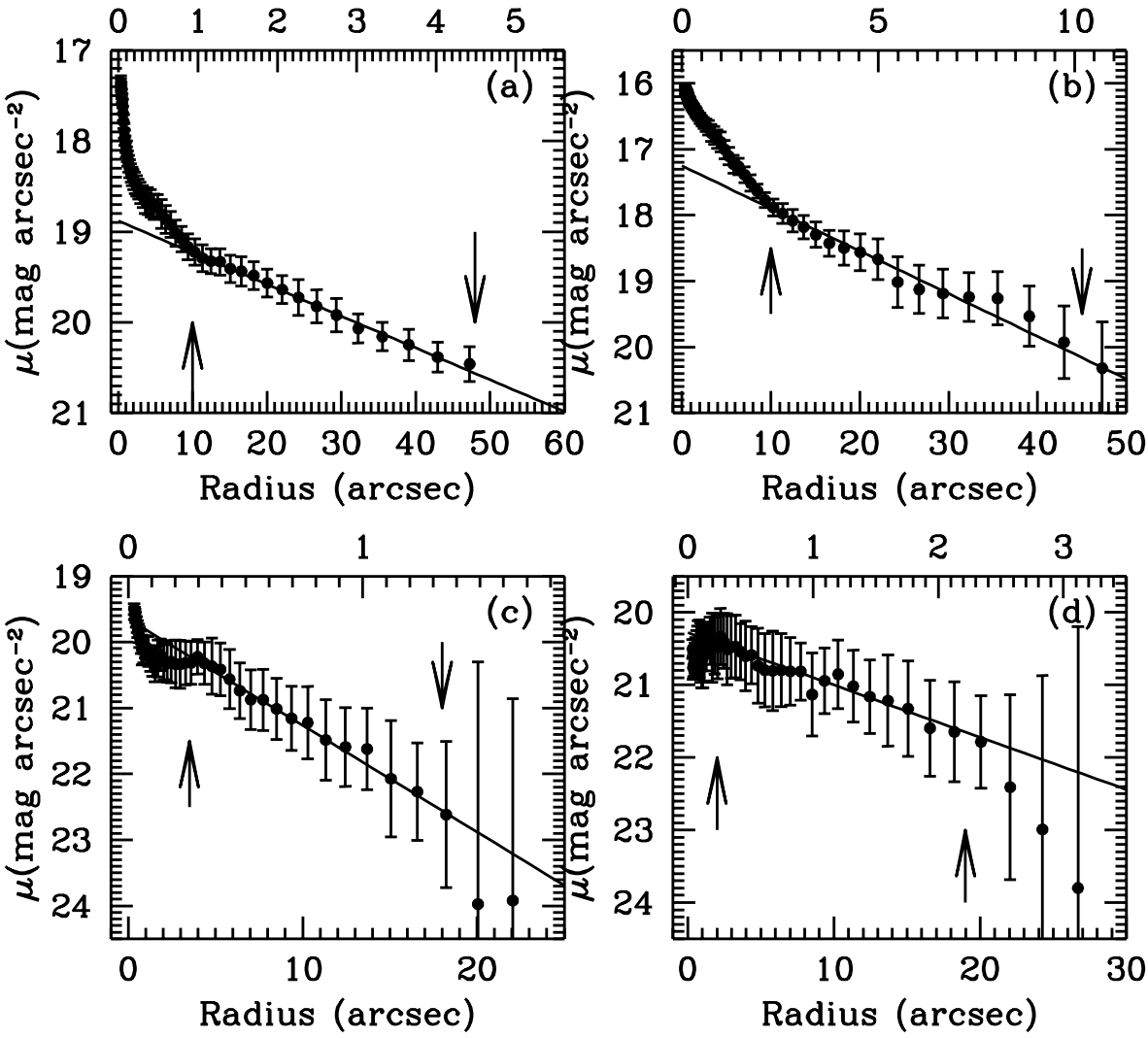

Figure 2.29: K_s-band surface photometry profiles of sample galaxies (a) UGC 11557 (b) UGC 11648 (c) UGC 11820 (d) UGC 11944. Arrows indicate profile portions where exponential disk fitting is performed.

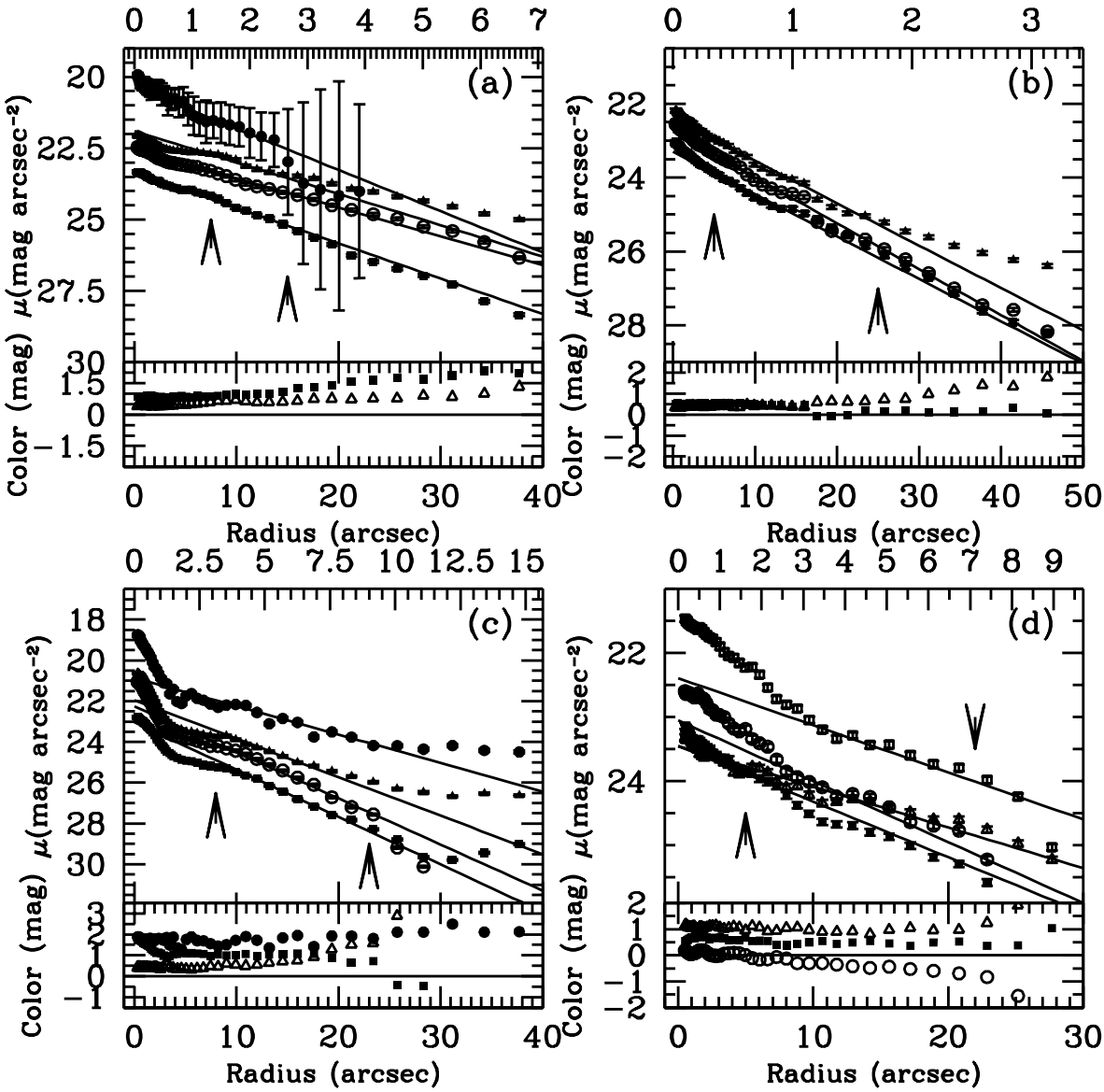

Figure 2.30: Multiband surface photometry profiles of sample galaxies Each symbol represet as follow: empty triangle U, filled square B, empty circle V, filled triangle R, empty square I, filled circle K_s for photometry profiles which are presented in upper boxes. Generally from the top to the bottom they are K_s-, I-, R-, V-, B-, and U-band.

Colors in lower boxes are represented by filled circles for R-K_s, empty triangles for V-R, or V-I, filled squares for B-V, and empty circles for U-B.

(a) D584-2 (b) D646-5 (c) D721-5 (d) F561-1

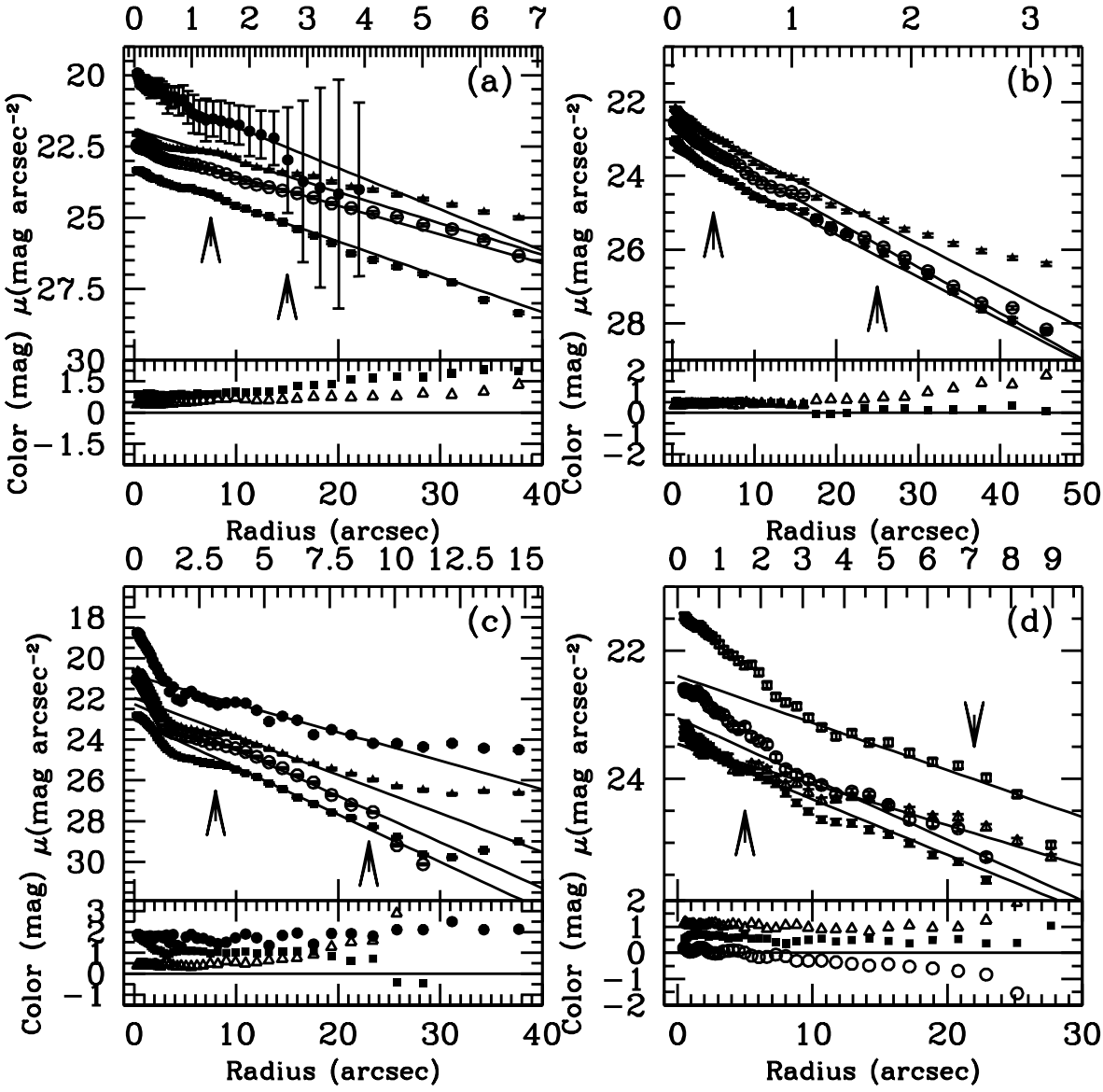

Figure 2.31: Multiband surface photometry profiles of sample galaxies (a) F563-v1 (b) F563-v2 (c) D721-5 (d) F568-1. Symbols are the same as in Fig.2.30.

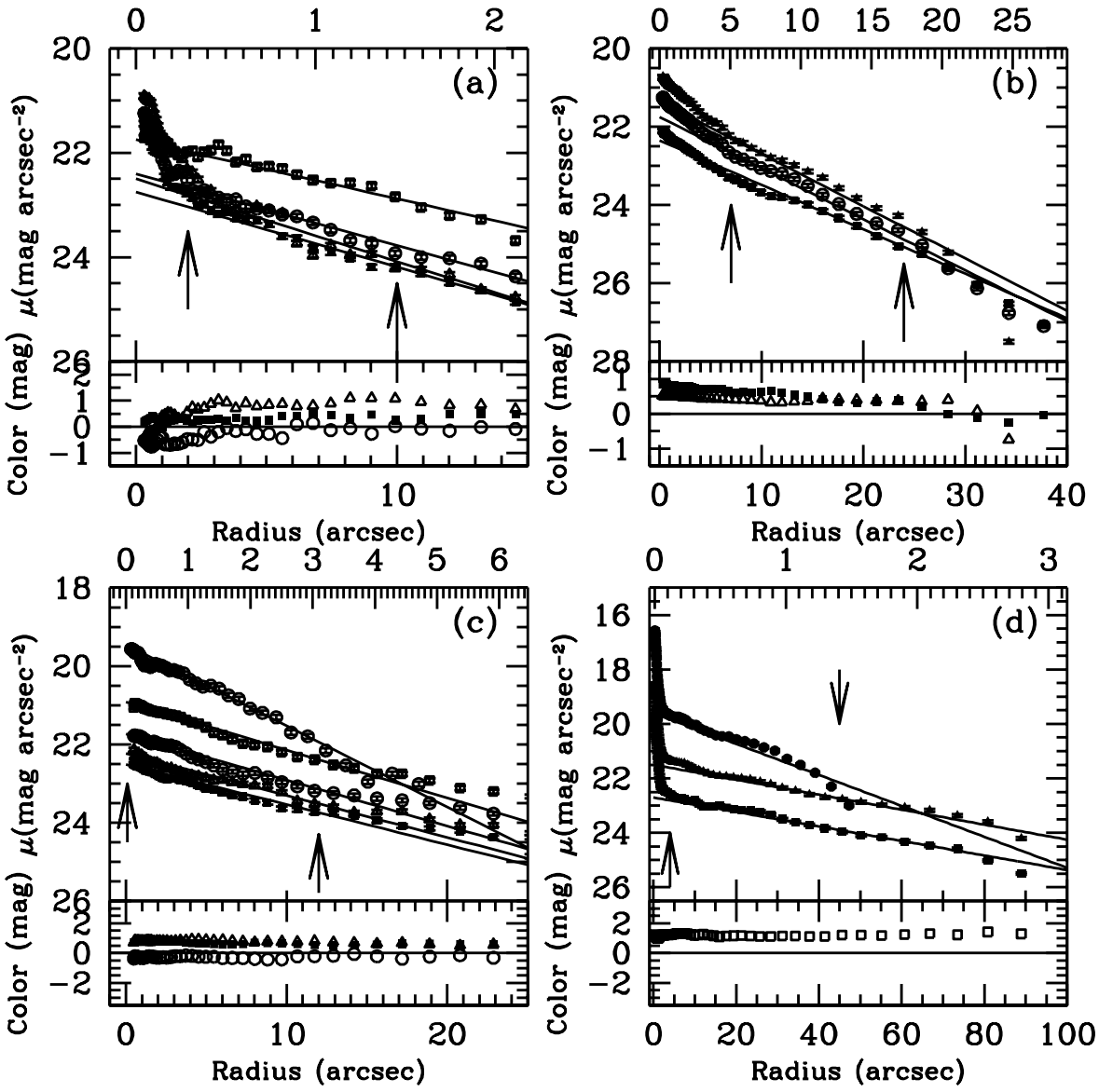

Figure 2.32: Multiband surface photometry profiles of sample galaxies (a) F611-1 (b) F730-v1 (c) UGC 1230 (d) UGC 2259. Symbols are the same as in Fig.2.30.

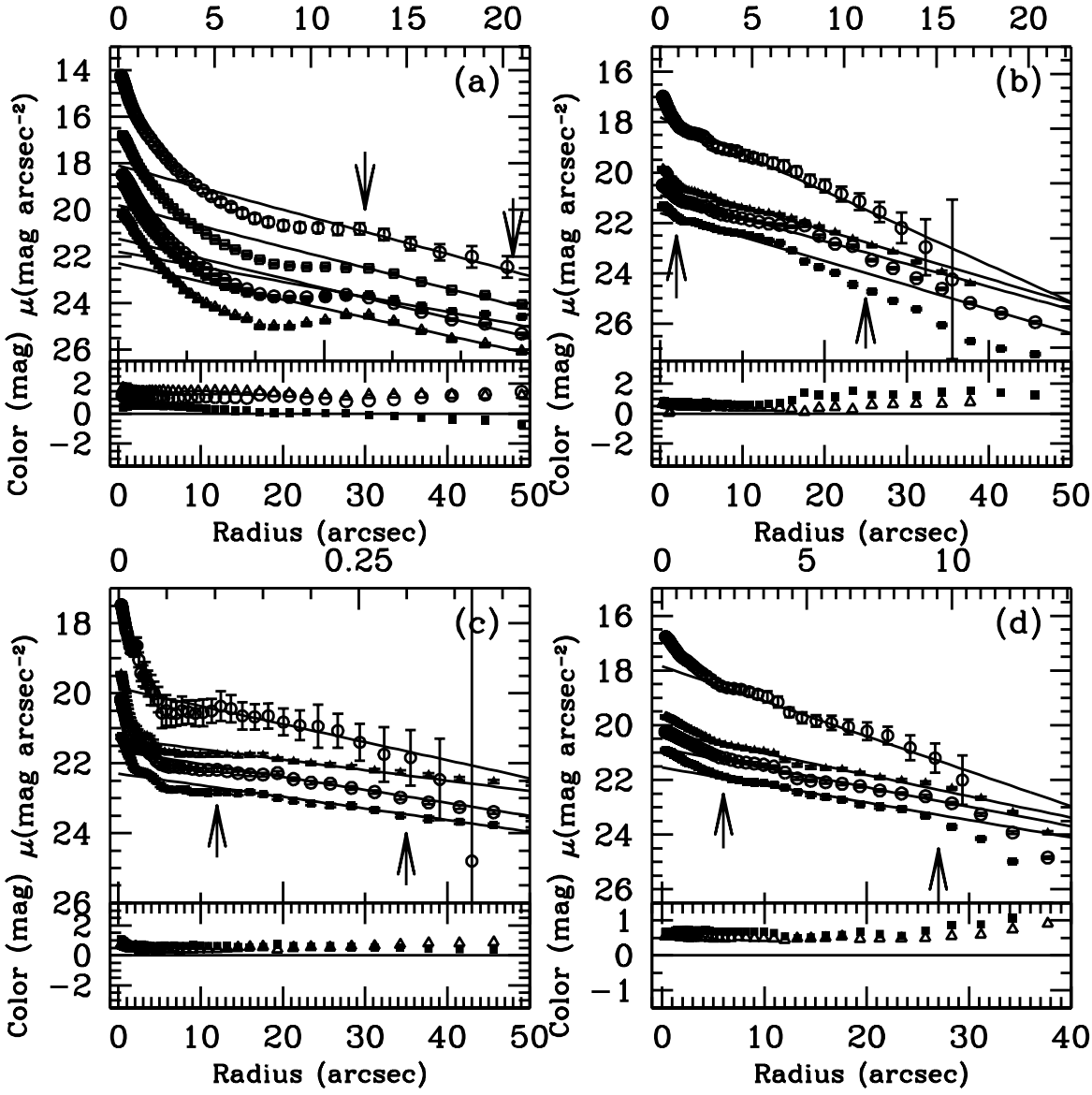

Figure 2.33: Multiband surface photometry profiles of sample galaxies (a) UGC 6614 (b) UGC 11454 (c) UGC 11583 (d) UGC 11616. Symbols are the same as in Fig.2.30.

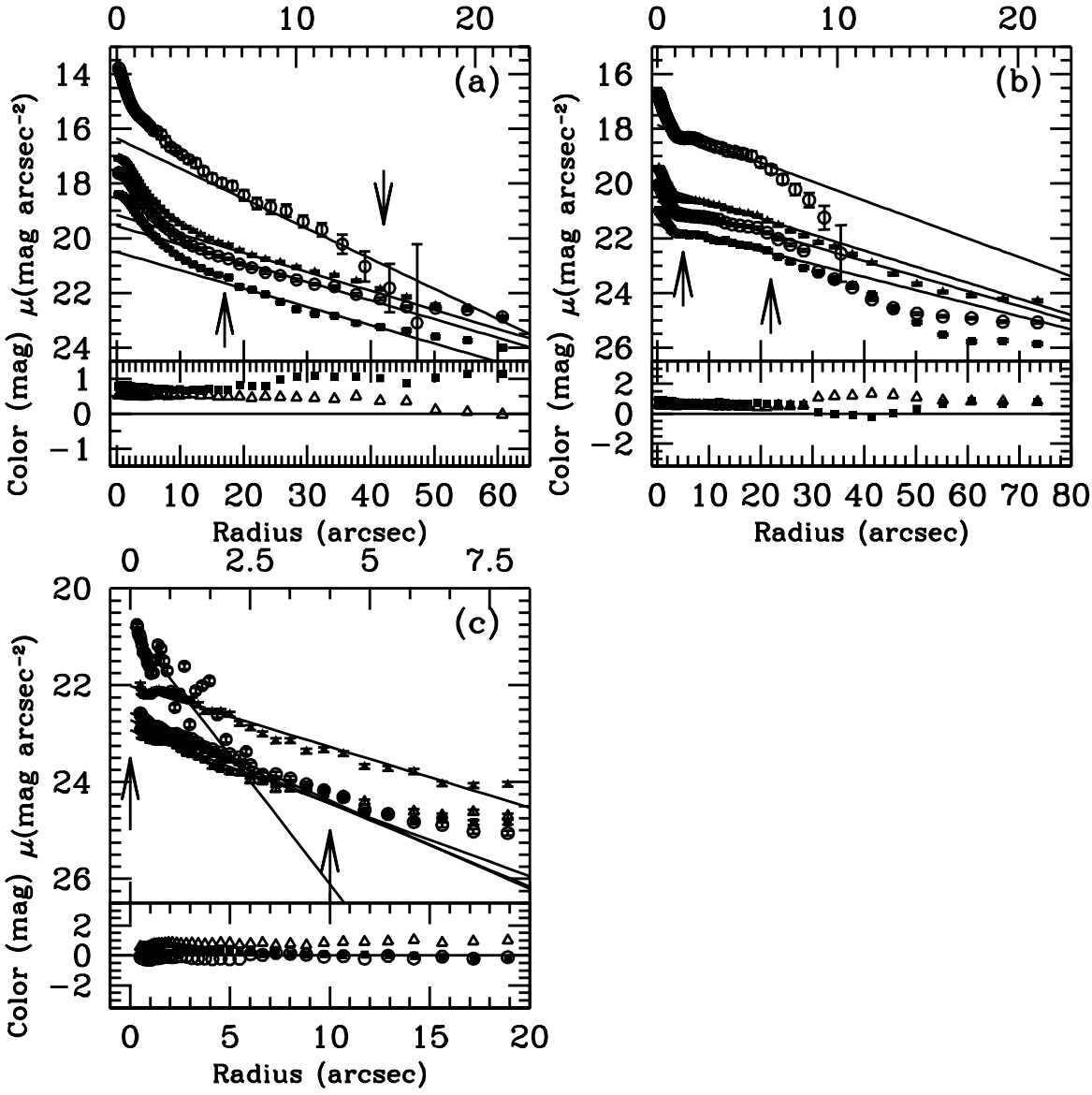

Figure 2.34: Multiband surface photometry profiles of sample galaxies (a) UGC 11748 (b) UGC 11819 (c) UGC 12695. Symbols are the same as in Fig.2.30.

Here, Σ is the surface luminosity density in flux units, r is the major axis radius, Σ_0 is the central surface brightness and α is the scale length of exponential disk. Σ_e and r_e are the effective surface brightness and effective radius, respectively.

For sample galaxies, exponential disk profiles are fit to surface brightness profiles generated by ARCHANGEL. Each surface brightness profile is examined carefully, then it is decided which portion of a profile is fitted as "disk". We performed this process by eye-examination. Each portion which is used as a disk is marked by arrows in each surface brightness profile plot. Then linear square fittings were run on these portions in order to calculate the central surface brightnesses and scale lenghts of disks.

Throughout bands, the central surface brightness and the exponential disk scales do not show any typical value, or any strong correlation within a given band (Fig.2.35).

For the sample galaxies with available B-band images, the average central surface brightness in the B-band is 23.13 mag arcsec^{-2} with a standard deviation of 0.93 mag arcsec^{-2}. Among these 19 galaxies, 2 galaxies have the central surface brightness brighter than 22 mag arcsec^{-2}. The average of exponential disk scale length for these galaxies is 3.29 $\pm$ 2.01 kpc.

Although not for the same sample galaxies, average central surface brightness for other bands are 22.54 $\pm$ 1.09 mag arcsec^{-2} , 22.08 $\pm$ 0.83 mag arcsec^{-2}, and 19.99 $\pm$ 1.27 mag arcsec^{-2} for V-, R-, and K_s-bands, respectively.

Average exponential disk scale lengths are 2.84 $\pm$ 1.68 kpc, 3.01 $\pm$ 1.91 kpc, and 2.57 $\pm$ 2.93 kpc for V-, R-, and K_s-bands, respectively.

These values do not represent trends through bands since their sample galaxies do not overlap exclusively. However, they still suggest that there exist some trends. Correlation coefficients between parameters within bands are given by Table 2.5,

Table 2.5. Correlation Matrix of B-band Parameters

	h	M_T
μ	-0.48	0.59
h		-0.68

Table 2.6. Correlation Matrix of V-band Parameters

	h	M_T
μ	-0.48	0.52
h		-0.59

2.6, 2.7 and 2.8. Trends through bands will be discussed in section 2.4.6 in detail.

2.4.4 Luminosity

ARCHANGEL measures flux of a target galaxy by integrating isophote flux along its radius. As for structural parameters, sample galaxies do not have any typical luminosity values through bands. (Fig.2.36). The only noticeable trend is that scatters increase for longer wavelength bands. The K_s-band luminosity has a much larger scatter compared to the B-band luminosity (Fig.2.36 (c)).

Sample galaxies have a wide range of luminosity. The brightest galaxy in the sample is roughly 4 orders of magnitude brighter than the least bright galaxy. This is valid throughout all bands.

Table 2.7. Correlation Matrix of R-band Parameters

	h	M_T
μ	-0.67	0.46
h		-0.53

Table 2.8. Correlation Matrix of K_s-band Parameters

	h	M_T
μ	- 0.57	0.59
h		-0.51

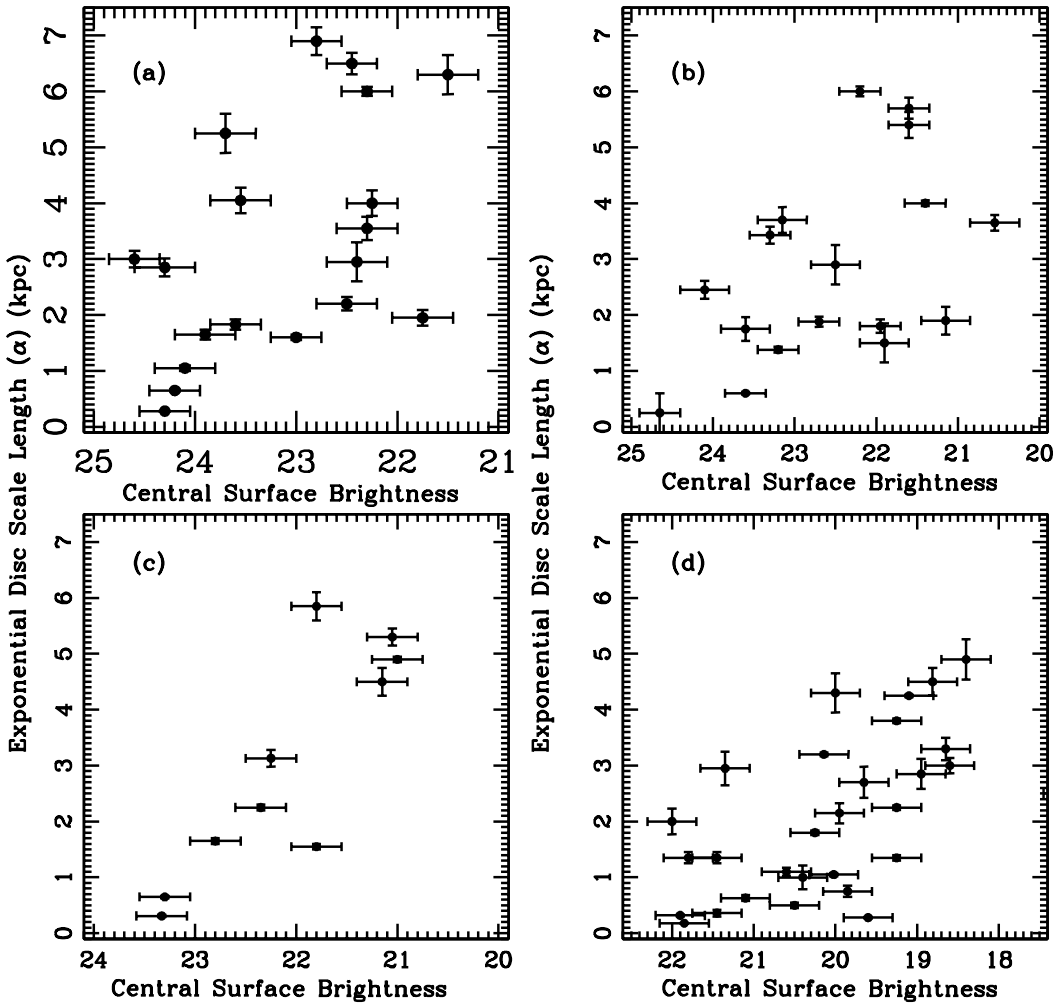

Figure 2.35: Central surface brightness vs disk scale length: (a) B (b) V (c) R (d) K_s.

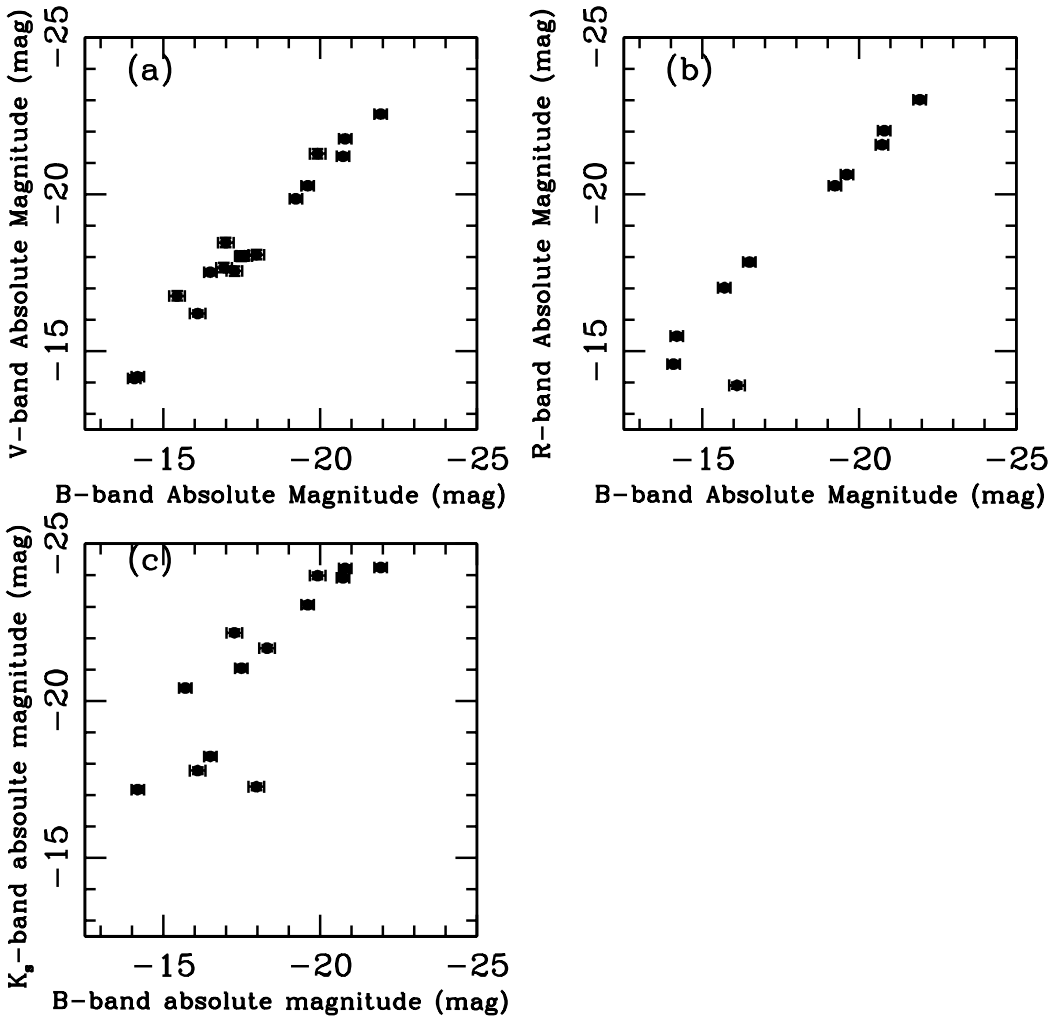

Figure 2.36: Luminosity plots show relations between broadband magnitudes. (a) B vs V (b) B vs R (c) B vs K_s.

Generally, sample galaxies are brighter when their central surface brightness is brighter through bands, although the scatter is big (Figs. 2.37). Likewise, sample galaxies are brighter when their disk scale lengths are bigger (Fig.2.38). This is an obvious trend since sample galaxies are selected to have a narrow window of central surface brightness.

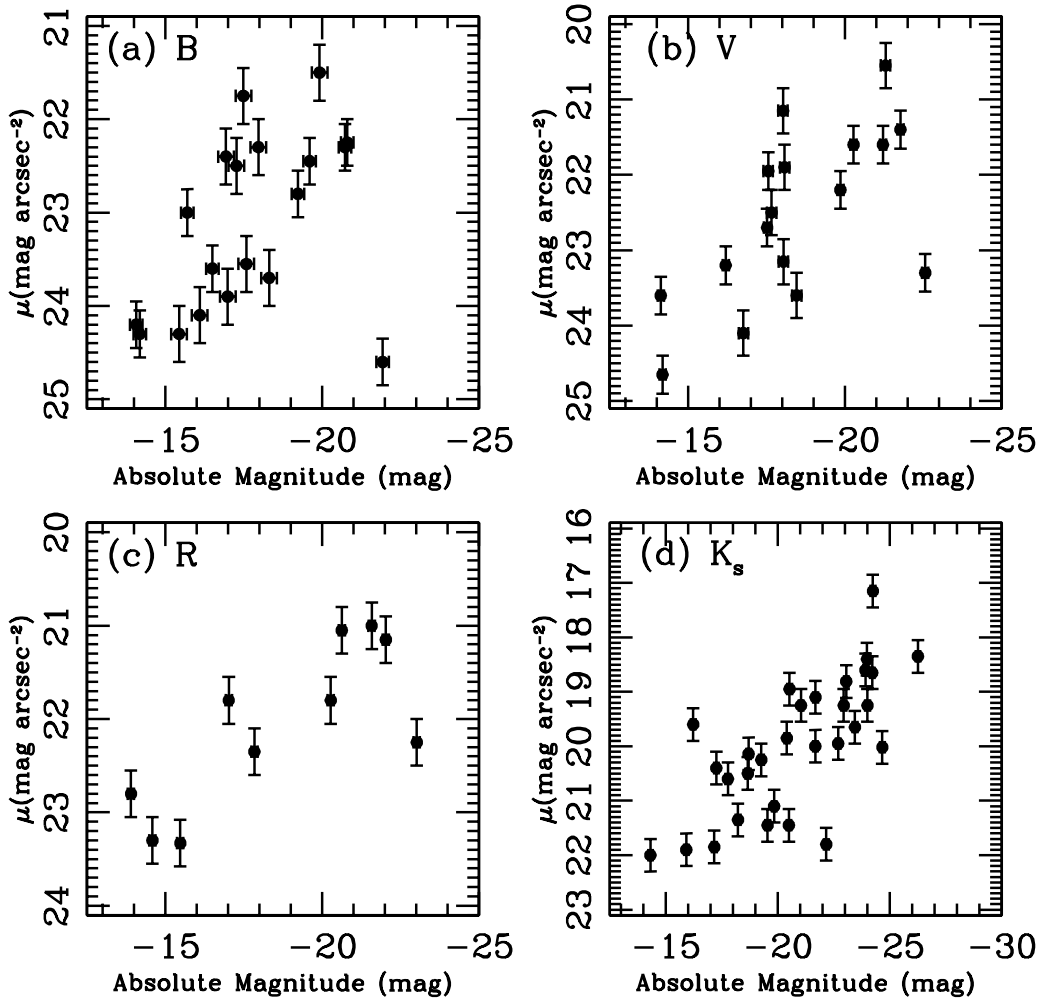

Figure 2.37: Luminosity versus central surface brightness. (a) B (b) V (c) R (d) K_s.

2.4.5 Colors

Since our optical broadband data are patchwork, colors should be taken carefully. For 32 galaxies, which have both $B-$, and $V-$bands available, the average of $B-V$ is 0.453 $\pm$ 0.28. For $B-R$, the average is 1.035 $\pm$ 0.28 with 12 sample galaxies, while -0.25$\pm$ 0.422 and 0.99 $\pm$ 0.40 for $U-B$ with 21 galaxies, and $V-I$ with 11 galaxies, respectively.

Compared to other studies, these mean colors are well matched. Mean colors

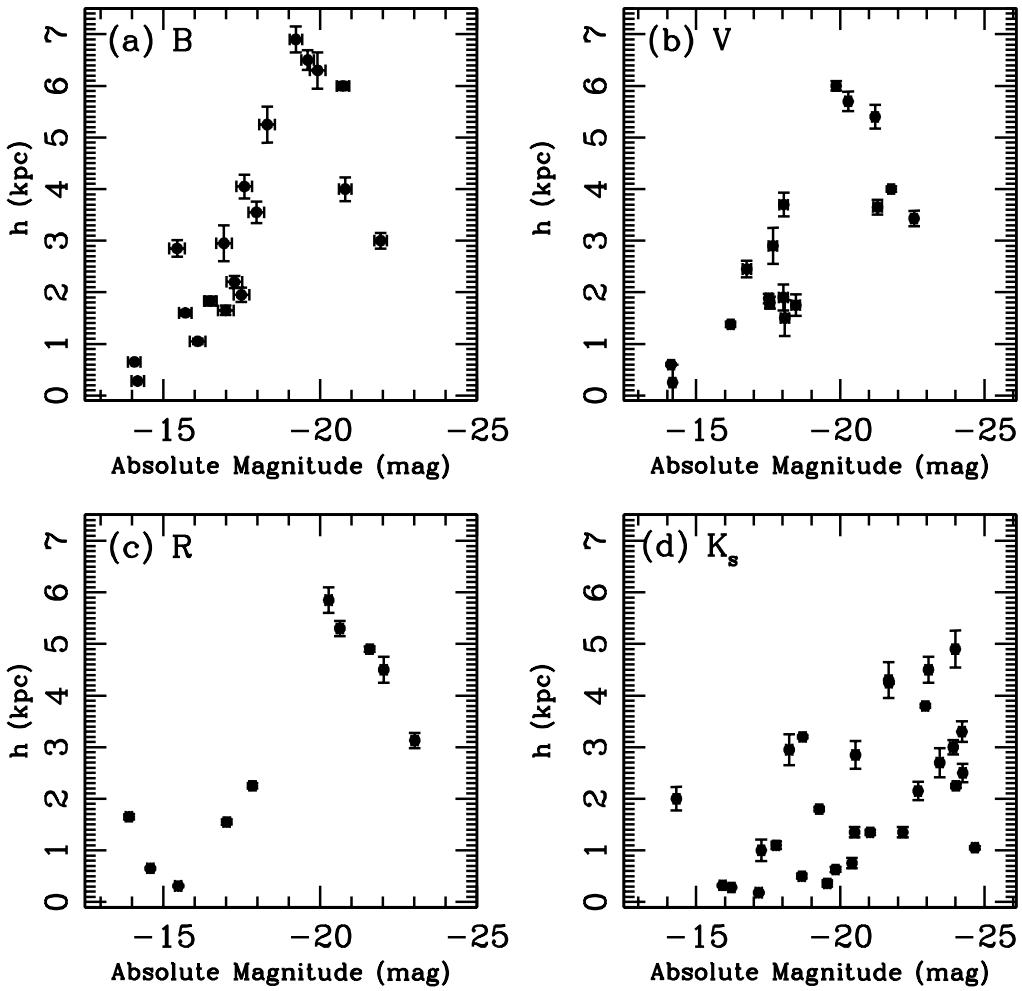

Figure 2.38: Luminosity versus exponential disk scale length. (a) B (b) V (c) R (d) K_s.

from McGaugh & Bothun (1994) are $U-B=-0.17\pm0.05, B-V=0.49\pm0.04$, and $V-I=0.89\pm0.04$. de Blok et al. (1995) has $U-B=-0.14\pm0.05, B-V=0.52\pm0.05, B-R=0.78\pm0.1$, and $V-I=0.69\pm0.01$.

In order to compare the colors of our sample LSBGs to HSBGs, we used color values derived by de Blok et al. (1995). Using the RC3 (de Vaucouleurs et al. 1991), the ESO-LV (Lauberts & Valentijn 1989), and results from some other studies, de Blok et al. (1995) determined the color of typical HSB Sdm-Sm galaxies. These

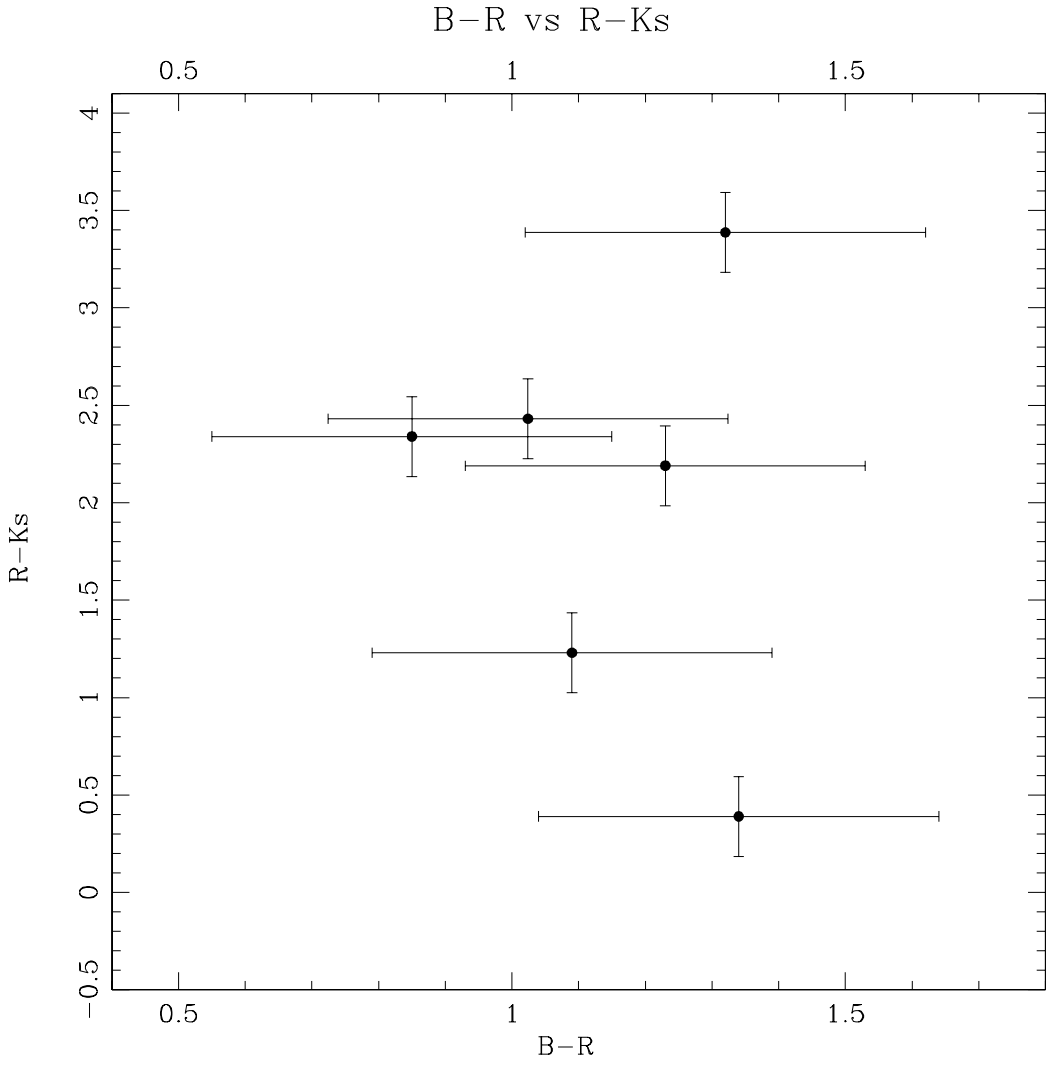

Figure 2.39: $B - R$ versus $R - K_s$ for sample galaxies.

colors are $U - B = -0.14, B - V = 0.51, B - R = 0.92$, and $V - I = 0.9$.

Comparison with these colors show that $U - B$ and $B - V$ of LSBGs are roughly identical to those of late-type HSB spiral galaxies. These blue colors are generally associated with star formation, which is taking place in LSBGs.

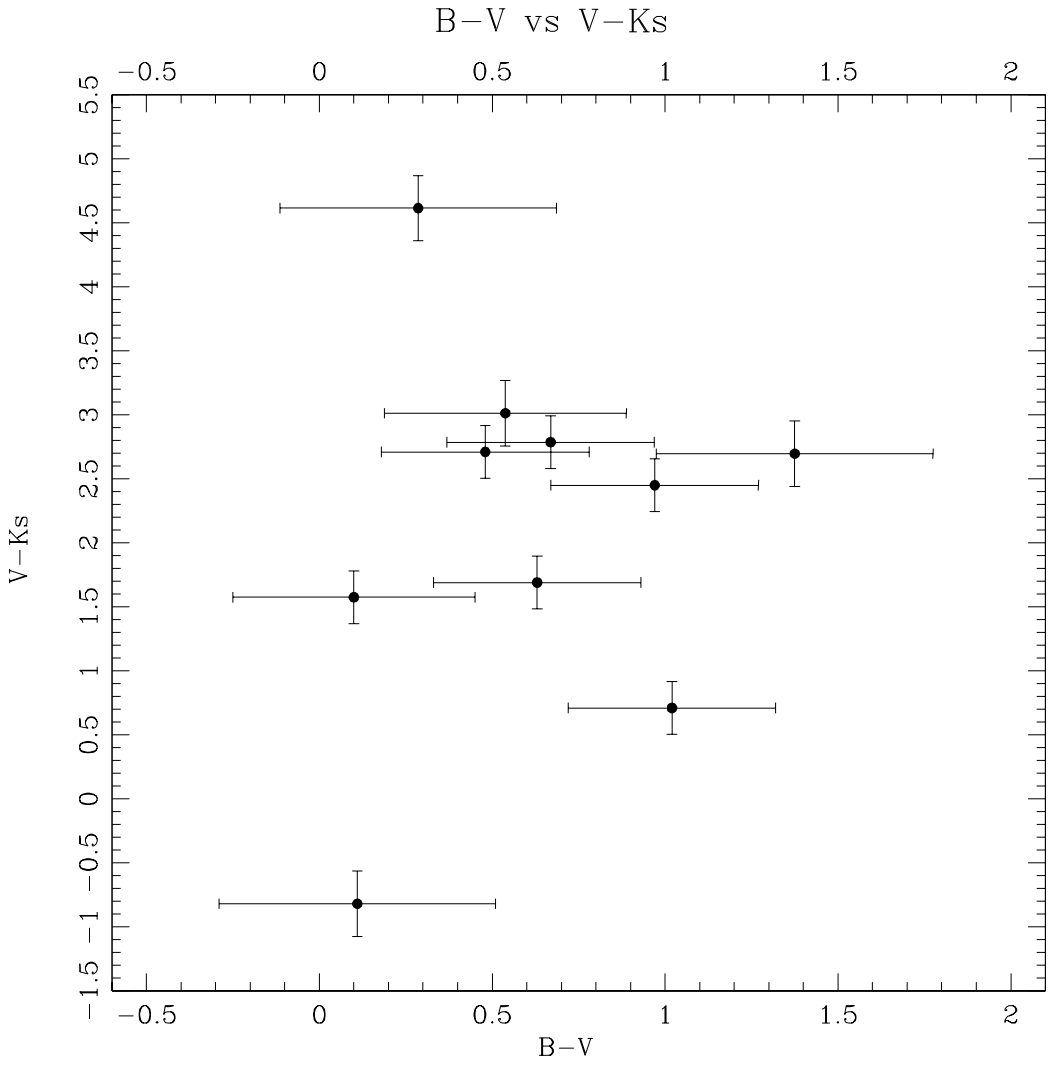

Figure 2.40: $B - V$ versus $V - K_s$ for sample galaxies.

2.4.6 Color Dependence of Structure Parameters

The structural parameters of exponential disk profiles depend on wavelength. In order to verify more carefully, sample galaxies which share same broadband luminosity data are plotted for various parameters (Figs. 2.41, 2.42,2.43, 2.44, 2.45).

For sample galaxies with $B-, V-$, and K_s-bands in common, central surface brightness increases from $\mu_0 = 22.88 \pm 1.02$ for $B-$band, to $\mu_0 = 22.18 \pm 1.12$ for $V-$band, to $\mu_0 = 19.71 \pm 1.49$ for K_s-band. Exponential disk scale length also increases from 3.33 ± 2.06 (kpc) for $B-$band, to 2.81 ± 1.67 (kpc) for $V-$band, to 2.38 ± 1.44 (kpc) for K_s-band.

This is also true for sample galaxies with $B-, R-$, and K_s- bands. Central surface brightness decreases from $\mu_0 = 23.25 \pm 0.89$ for $B-$band, to $\mu_0 = 21.96 \pm 0.80$ for $R-$band, to $\mu_0 = 18.81 \pm 1.84$ for K_s-band. Exponential disk scale length decreases from 3.03 ± 2.14 (kpc) for $B-$band, to 2.94 ± 1.69 (kpc) for $R-$band, to 2.29 ± 1.38 (kpc) for K_s-band.

It is noticed that, for disk scale length, ratios between disk scale length of each band should be examined rather than simple averages, because changes within small galaxies with small disk scale lengths would be hidden with simple comparison of averages.

That being said, it is relatively clear that disk scale length of K_s is shorter than those of $B-, V-$, and $R-$bands. It is not clear that this will invoke color gradient on disk stellar populations, since, for some sample galaxies, K_s-band images show marginal detection and lead to short disk scale lengths. Our surface brightness detection limit for the K_s-band images is about 23.5 mag arcsec^{-2}. There are sample galaxies whose exponential disks do not extend to two to three times their disk scale lengths above this limit (e.g. UGC 12695 see Fig.2.34 (d)). We excluded

Table 2.9. Correlation Matrix of Color Dependence

	B-V	B-R	R-K_s
M_B	-0.49	0.51	0.12
M_{Ks}	-0.32	0.41	0.15
μ_B	-0.71	-0.12	0.07
μ_{Ks}	-0.59	-0.55	0.10
h_B	0.51	-0.65	0.09
h_{Ks}	0.65	-0.53	0.16

sample galaxies which do not show their disks extending two times their optical scale lengths, then calculated ratios of B-band exponential disk scale length to K_s-band exponential disk scale length. For those 13 sample galaxies, the mean ratio between two disk scale lengths is 0.67 compared to the mean ratio of 0.57 for the entire sample. Therefore, we can conclude K_s-band disk scale lengths generally are shorter than B-band disk scale lengths for our sample LSBGs. de Jong & van der Kruit (1994) and Peletier et al. (1994) found similar results.

2.5 Discussion

We have looked into colors of our sample LSBGs and compared them to colors of LSBGs from literatures and those of HSBGs. In this section, we describe a few plausible scenarios which may apply to LSBGs, and discuss their strengths and shortcomings.

2.5.1 Initial Starburst Scenario

An initial starburst with subsequent cutoff in star formation makes disks, or galaxies redder and fainter with time, as short-lived blue stars die. When LSBGs were first found, this scenario was considered as a very natural explanation for the nature of LSBGs. They were simply regarded as the faded remnants of normal galaxies.

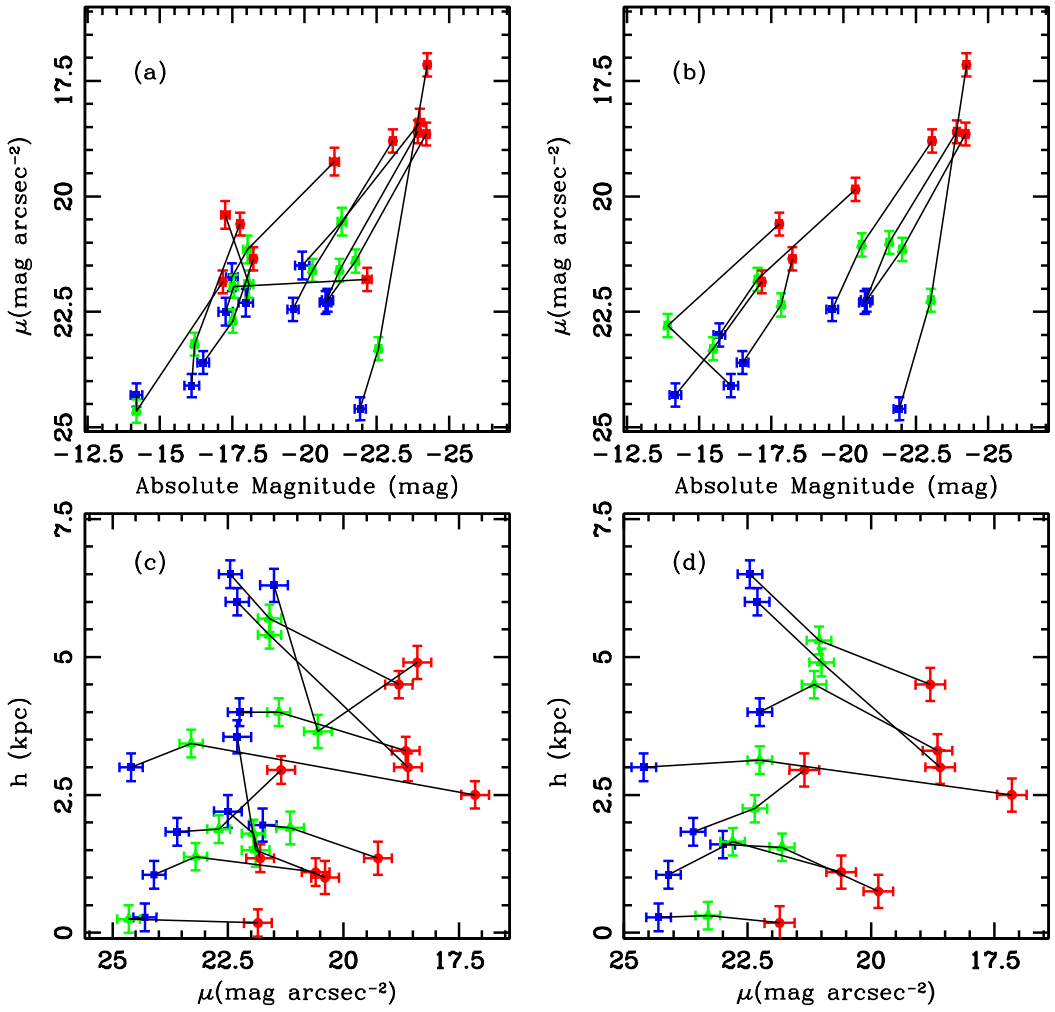

Figure 2.41: Correlations between central surface brightness, disk scale length and luminosity for various bands. Left panels represent sample galaxies with B, V, and K_s bands. Right panels represent sample galaxies with B, R, and K_s bands. Blue symbols represent B-band values, green symbols represent either V (left panels), or R-band (right panels) values, and red symbols represent K_s-band values. (a) luminosity versus central surface brightness (b) luminosity versus central surface brightness (c) central surface brightness versus disk scale length (d) central surface brightness versus disk scale length.

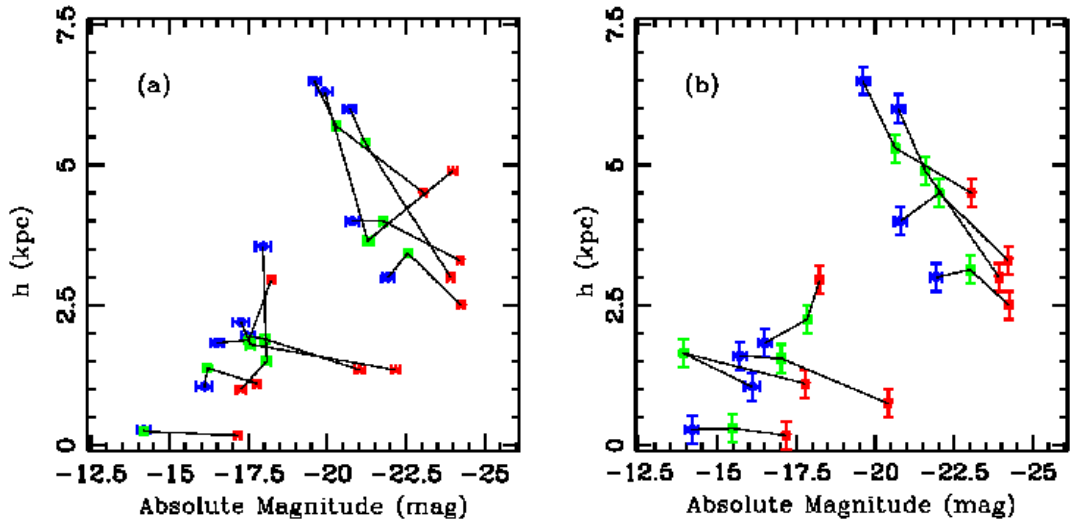

Figure 2.42: Correlations between central surface brightness, disk scale length and luminosity for various bands. See Fig.2.41 for symbol descriptions. (a) luminosity versus disk scale lengths (b) luminosity versus disk scale lengths.

However, we should be able to witness a strong correlation between their central surface brightnesses and colors, or any age indicators for that matter. Fig. 2.43 (b) does not show the necessary trend. If LSBGs truly had been once normal galaxies, their central surface brightnesses should become fainter as $B - V$ colors become redder. This is not shown by Fig. 2.43 (b). Based on this plot, generally bluer galaxies are those galaxies with fainter central surface brightnesses, not only in the B-band, but also in the K_s-band.

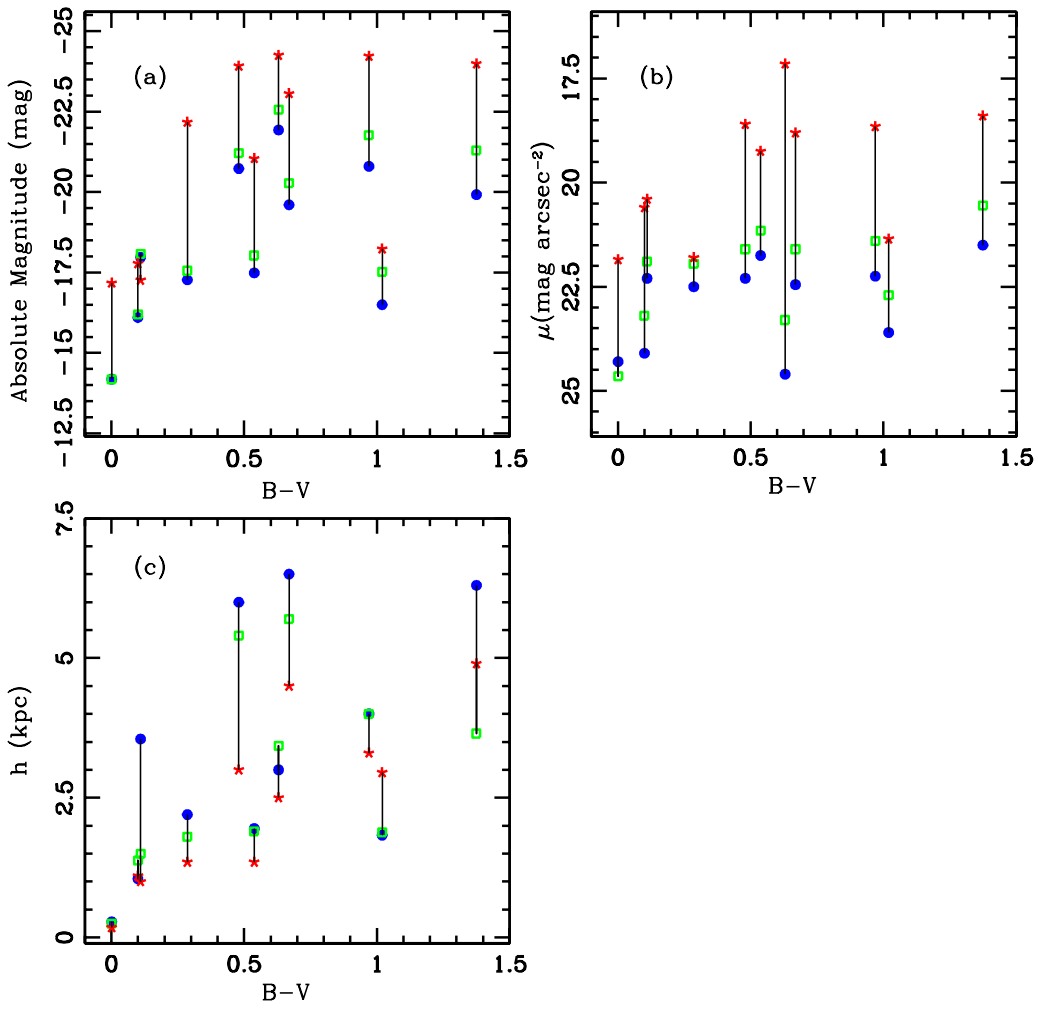

Figure 2.43: Color dependence of central surface brightness, disk scale length and luminosity. See Fig.2.41 for symbol descriptions. These panels are sample galaxies with B, V, and K_s-band data. (a) B-V versus luminosity (b) B-V versus central surface brightness (c) B-V versus disk scale length.

2.5.2 Exponentially Declining Scenario

The scenario with exponentially declining star formation rates (SFRs) has been considered as the standard star formation history for spiral galaxies. This scenario can result in blu colors in $U-B$ and $B-V$ bands which are similar to those of spiral galaxies since these two colors are sensitive to recent star formation activity.

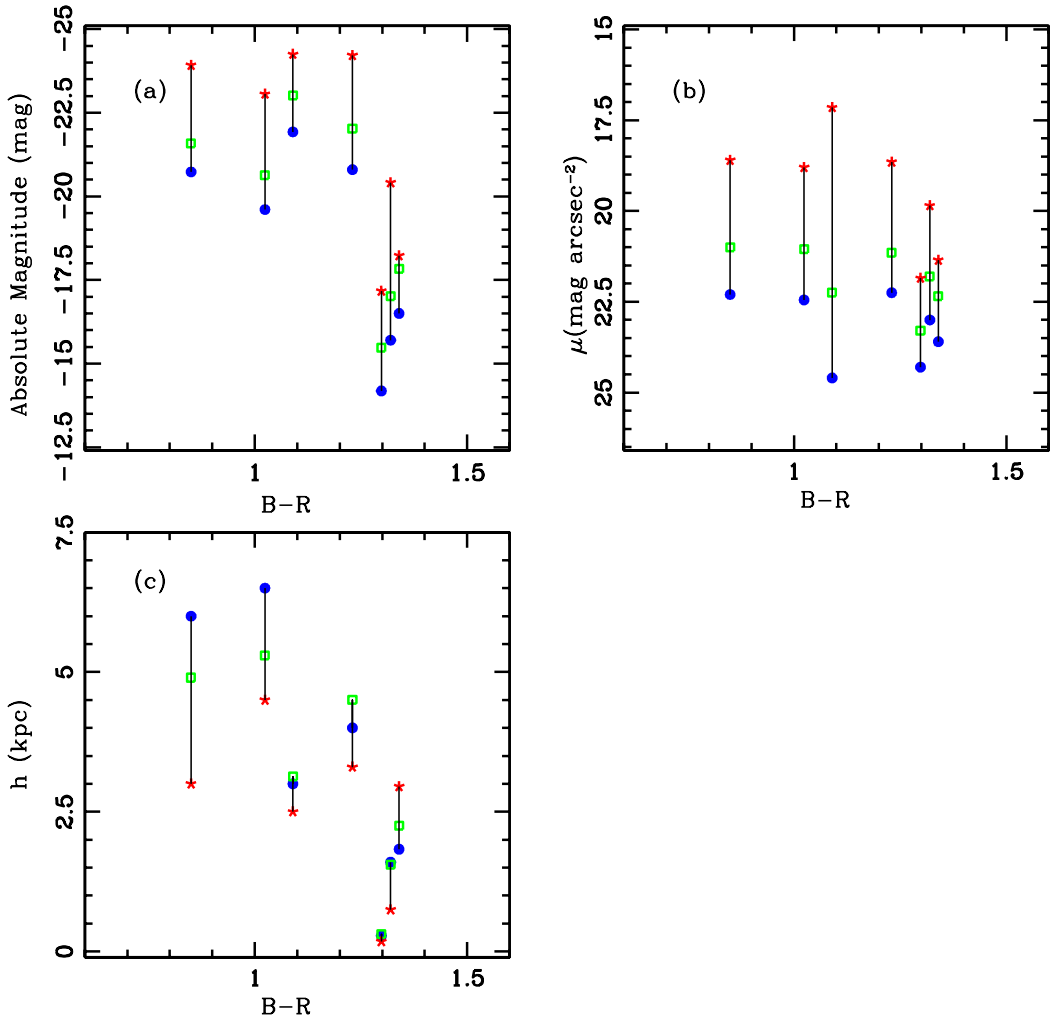

Figure 2.44: Color dependence of central surface brightness, disk scale length and luminosity. See Fig.2.41 for symbol descriptions. These panels are galaxies with B, R, and K_s-band data. (a) B-R versus luminosity (b) B-R versus central surface brightness (c) B-R versus disk scale length.

Although very weak, LSBGs do have star forming activity and this scenario with declining SFRs fits well with low current SFRs that we observe in LSBGs.

Therefore, in order to confirm whether LSBGs really have gone through the SFHs with exponentially declining SFRs, we have to look at the presence or absence of a large old, red stellar population, since a greater amount of stars should have been formed in the past with this SFH. These old stars should be eminent in the $R-$ and

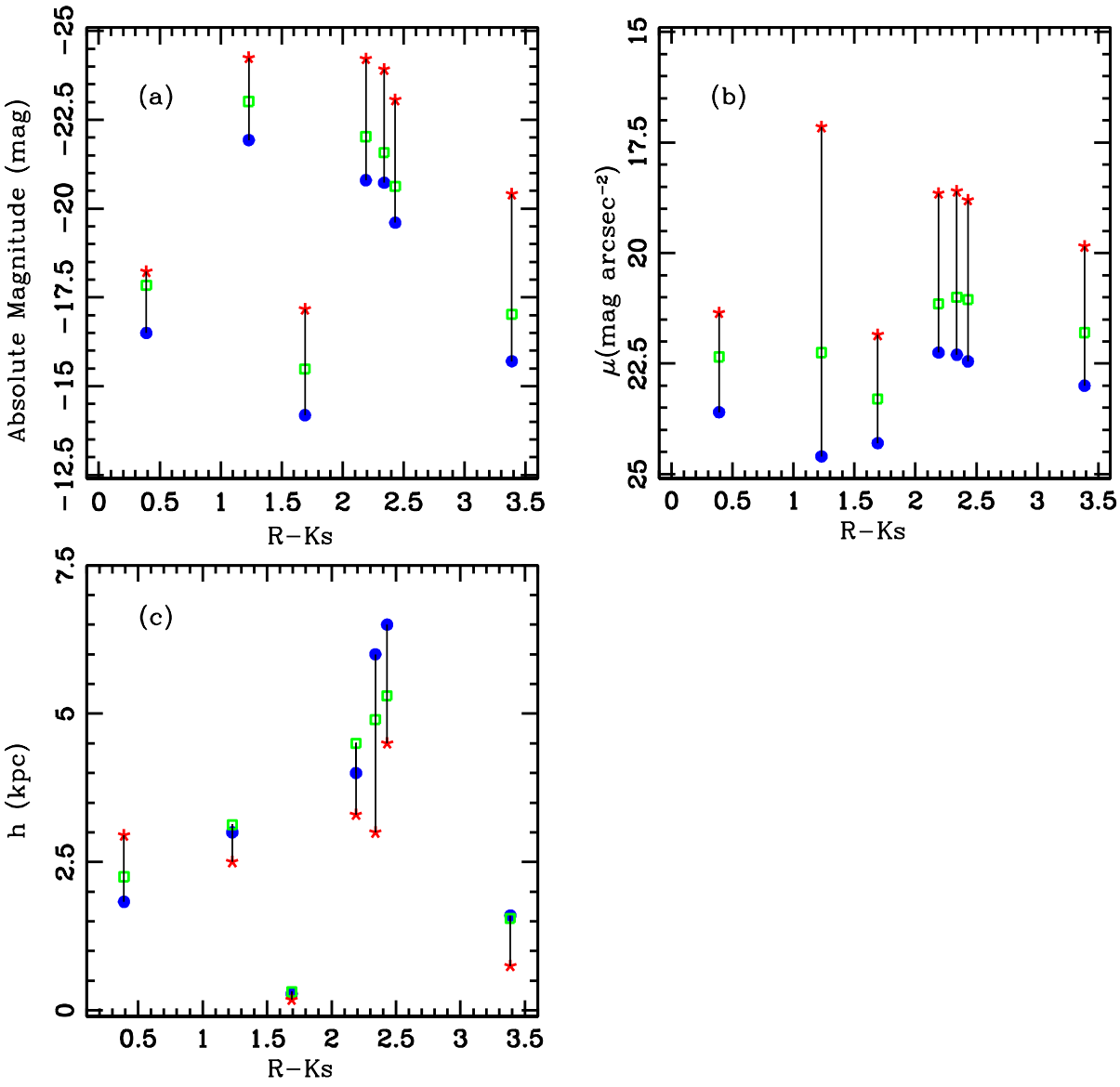

Figure 2.45: Same as Fig.2.43. (a) R-K_s versus luminosity (b) R-K_s versus central surface brightness (c) R-K_s versus disk scale length.

$I-$ bands and colors of galaxies with these old populations will be similar to those of late-type HSBGs. However, the $B-R$ and $V-I$ colors of LSBGs are bluer than those of HSBGs.

K_s-band photometry may be the best indicator for old stellar populations since it is believed to be insensitive to current star forming activity. Although LSBGs generally are less luminous than HSBGs in the K_s-band, there are several LSBGs which are quite luminous in the K_s-band. Indeed, among our sample LSBGs, there are several galaxies whose absolute K_s-band magnitudes reach $\sim$ -24 mag. However, galaxies which are luminous in the K_s-band do not always have red colors in $V-I$ similar to those of HSBGs. Of ten sample LSB galaxies whose K_s-band absolute magnitudes are brighter than -22.0 mag, three LSBGs clearly have bluer $V-I$, or $R-I$ colors and another three galaxies have intermediate colors. Hence the exponentially decreasing scenarios is not favored to explain colors of LSBGs.

2.5.3 Constant Star Formation Scenario

A galaxy with a constant SFR scenario would have $U-B$ and $B-V$ colors similar to those of LSBGs. $B-R$ and $V-I$ colors are also expected to show the presence of of a large old population which have been formed through the life time of a galaxy. Although we can claim that generally our sample LSBGs have bluer colors of $B-R$ and $V-I$, we can not simply rule out this scenario. Unlike what de Blok et al. (1995) found, we have many LSBGs with high luminosity in NIR photometry, which potentially lead into a large amount of old stellar populations, and a decent number of our sample LSBGs have redder colors of $B-R$ and $V-I$ than values from previous studies. A roughly constant SFR over time does thus seem grossly consistent with the observed colors.

2.5.4 Sporadic Star Formation Scenario

The blue $U - B$ and $B - V$ colors, combined with the fact that there are star formation activities in LSBGs, suggest that LSBGs may have SFHs with sporadic SFRs. Based on low metallicity and the near absence of molecular ISM, it is quite unlikely that LSBGs have had a large amount of past star formation. Still a small surge in SFR can make those colors bluer. Salzer et al. (1991) show that it does not require a large amount of young blue populations to produce blue colors especially in LSB regions. Therefore, if a small hike in the SFR of a LSBG is taking place at the moment, it leads to bluer colors for the galaxy, whether or not it has had a very low constant SFR.

2.6 Summary

We have looked into luminosities, colors, and structural parameters of a large sample of LSBGs. They are generally blue in optical and NIR colors, as has been documented. Although we cannot draw firm conclusions on the SFHs of LSBGs, it is clear that the stellar populations do indeed contain a young components. Much of light from LSBGs originate from their young stars. Several SFH scenarios, such as an initial burst scenario and an exponentially decreasing SFR scenario do not explain colors of LSBGs. We still need to look into their current star formation activity and amounts of their old stellar populations in order to confirm how their SFHs have been evolving.

Structural parameters of LSBGs, along with their luminosities, have a large range of values. The most distinctive relationship is that disk scale lengths become shorter toward longer wavelengths, especially in the NIR wavelengths.

Chapter 3

Star Formation in Low Surface Brightness Galaxies

3.1 Introduction

Star formation is one of the most important factors in deciding the evolutionary histories of galaxies. Galaxies turn gas into stars in variety of different ways with different star formation histories (SFHs). The stellar life cycle changes properties of galaxies such as luminosity, colors and morphology. Of star formation properties, young massive star formation is most important because it involves large and rapid changes. Therefore, investigation of the younger stellar content of galaxies have been very important for understanding star formation properties of galaxies and their implications for the evolutionary properties.

There are several methods to trace the young stellar populations of galaxies, which rely on integrated light measurement, or nebular recombination lines. The most basic method involves the use of integrated colors and spectra along with synthesis models (Bruzual & Charlot 1993). However, star formation rates (SFRs)

derived from integrated colors are relatively uncertain due to reddening, IMF, age, or metallicity. Ultraviolet continuum is dominated by young stars, thus provides a more reliable probe across redshifts, although the extinction calibration is problematic. On the other hand, since the dust absorbs a large portion of the ultraviolet continuum and re-emits in the thermal infrared around at 10$\sim$300 μm, the far-infrared emission can be a good tracer of the SFR. However, dust heating and re-emitting are complex processes that make the relationship between IR emission and the SFR uncertain.

Although it has its own shortcomings, using the nebular emission lines, in particular Hα luminosity, is most popular to measure the SFR. The emission lines re-emit the integrated stellar luminosity of galaxies shorter than the Lyman limit, therefore provide a direct, sensitive probe of the young massive stellar population.

LSBGs are known to have very low SFRs, probably an order of magnitude lower than that of HSBGs (Bothun et al. 1997; McGaugh et al. 1995a). However, there have not been many studies which have tried to measure SFRs from a large sample of LSBGs. van Zee (2001) measured SFRs of several LSBGs in her sample, while her main samples consist of dwarf galaxies. Recently, O'Neil et al. (2007a) measured SFRs for 15 LSBGs. However, their sample consists mainly of large LSBGs.

We measured SFRs of a large random sample of LSBGs and investigate their star formation properties We studied correlations between star formation characteristics and other physical parameters, such as luminosity, colors, structural parameters and so on. In section 3.2, we present our observation and data reduction process in detail. Results follow in Section 3.3 providing basic measurement results along with correlations between parameters. In section 3.4 we present Hα images of sample galaxies and discuss Hα emission morphology. In section 4.4 we discuss implications of our results for star formation history of LSBGs.

3.2 Observations and Data Reduction

3.2.1 Sample Selection

Sample selection criteria for the near-infrared observation is given in 2.2.1. Basic properties of sample galaxies are provided by Table. 3.1.

Observations

All observation runs for Hα photometry were performed by the Mino-Mosaic Imager at the WYIN 3.6-m telescope. The Mini-Mosaic Imager (heerafter, MIMO) consists of two SITe 4096x2048 chips separated by a tiny gap, which corresponds to 50.5 pixels. The MIMO has a pixel scale of 0.14″/pixel and a large field of view (9.6 × 9.6 ′), which is fairly compatible with FLMN. Each of the two CCDs is read out through 2 amplifiers, resulting in a modestly short readout time for the 4096 × 4096 equivalent array.

There were two runs in November 2003 and May 2004, which consist of 4 and 3 nights, respectively. We lost a night from November 2003 run due to weather. The first night of May 2004 run was not photometric. For the rest of the nights, weather condition was photometric.

Observations were executed following these procedures. Zero and dark frames are obtained during day time as much and as often as possible. We also obtained dome flats for each Hα filter, including WIYN-14, which is an off-band filter. For scientific frames, we obtained at least 2 frames, per sample galaxies, which shift along the north-south direction. This is to eliminate the known cross-talk ghost effect between amplifiers. We generally had sample galaxies sit around the center of each CCD chip for each exposure.

Table 3.1. Basic Properties of Sample Galaxies

Galaxy	RA (J2000.0)	Dec (J2000.0)	V_{helio} (km s^{-1})	Distance (Mpc)	i (deg)	Morphological Type	Alternate Names	References
(1)	(2)	(3)	(4)	(5)	(6)	(7)	(8)	(9)
D500-2	10 31 43.4	+25 18 30.0	1282	17.8		Sm	UGC 5716	
D512-2	14 33 20.1	+26 59 50.0	835	11.6	61	Sm	F512-1	(2)
D570-4	11 18 21.4	+17 41 51.0	1051	14.6	47	dI	F570-7	(2)
D575-5	12:55:40.5	+19:12:33.0	419	5.8	64	dI	F575-3	(2)
D584-2	16 01 49.3	+18 43 14.6	2627	36.5	52	Im	UGC 10410	(2)
D646-7	12 58 40.4	+14 13 03	214	3.0		ImV	UGC 8091	
DDO 189	14 22 32.2	+45 23 02.0	686	9.5		Im	UGC 9211	
F561-1	08 09 41.3	+22 33 33.0	4807	66.8		Sm		
F563-V1	08 46 37.8	+18 55 26.0	3890	54.0		dI	D563-3	
F568-1	10 26 06.3	+22 26 01.0	6524	90.6	26	Sc		(1)
F577-V1	13 50 10.1	+18 16 07.7	7788	108.2	35	Sd		(3)
NGC 1560	04 32 49.1	+71 52 59.0	-36	4.5		SAd	UGC 3060	
NGC 4455	12 28 44.1	+22 49 21.0	637	8.8	78	SBd	UGC 7603	(5)
UGC 128	00 13 50.9	+35 59 39.0	4531	62.9	57,26	Sdm		(6),(7)
UGC 334	00 33 54.9	+31 27 02.6	4627	64.3	24	Sm	DDO 4	(7)
UGC 628	01 00 51.9	+19 28 32.9	5446	75.6	56	Sm		(5)
UGC 731	01 10 43.9	+49 36 07.9	639	8.9	57	Im	DDO 9	(5)
UGC 1230	01 45 32.5	+25 31 16.0	3833	53.2	25,22	Sm		(3),(5)
UGC 2259	02 47 55.4	+37 32 18.6	583	8.1	43	SBdm		(8)
UGC 2885	03 53 04.3	+35 35 31.0	5802	80.6	62	SAc		(9)
UGC 3371	05 56 38.6	+75 18 58.0	816	11.3	49	Im	DDO 39	(3)
UGC 5750	10 35 45.1	+20 59 24.0	4169	57.9		SBdm		
UGC 5981	10 52 03.9	+10 08 54.0	2720	37.8		SAc	NGC 3433	
UGC 6151	11 05 56.3	+19 49 31.0	1335	18.5		Sm	DDO 91	
UGC 6614	11 39 14.8	+17 08 36.8	6352	88.2	34,36	SAa		(3),(4)
UGC 8837	13 54 45.7	+53 54 02.7	144	3.8*	80	IBm	DDO 185	(5)
UGC 9992	15 41 47.8	+67 15 15.3	427	8.8*	30	Im		(4)
UGC 10310	16 16 18.3	+47 02 47.1	716	9.9	34	SBm	DDO 204	(4)
UGC 11454	19 31 33.6	+49 52 46.4	6628	92.1	64	Sdm		(4)
UGC 11557	20 23 58.3	+60 11 33.4	1390	19.3	36	SABdm		(4)
UGC 11583	20 30 15.3	+60 26 25.0	127	5.9*	83	Irr	KK98 250	(4)
UGC 11616	20 41 13.5	+63 30 38.4	5244	72.8	60	Scd		(4)
UGC 11648	20 53 09.5	+67 10 32.9	3361	46.7	83	Im		(4)
UGC 11748	21 27 39.8	+45 28 58.8	5265	73.1	81	S		(4)
UGC 11819	21 49 10.7	+41 56 53.3	4261	59.2	66	Im		(4)
UGC 11820	21 49 28.4	+14 13 52.0	1104	15.3	50	Sm		(4)
UGC 11944	22 12 00.7	+17 54 09.6	1734	24.1	72	Im		(4)
UGC 12695	23 36 02.2	+12 52 32.5	6185	85.9	49	Sm		(3)

Note. — Col.(9): References for inclination angle, and position angle.

REFERENCES - (1) de Blok et al. (1996) (2) Eder & Schombert (2000) (3) McGaugh & Bothun (1994) (4) McGaugh et al. (2001) (5) de Blok & Bosma (2002) (6) de Blok et al. (1995) (7) Bell et al. (2000)(8) Carignan et al. (1988)(9) Canzian (1993) (10) Swaters et al. (2003)

Table 3.2. Parameters of Hα Filters

Name	Center Wavelength	FWHM	T_{mas}	V_{helio}	Comments
WIYN-14	6562	378	89	N/A	Hα continuum
WIYN-15	6569	73	84	$0 \sim 1280$	Hα narrow
WIYN-16	6620	72	86	$960 \sim 4250$	Hα narrow
KPNO-1565	6653	68	83	$2560\sim 5670$	Hα narrow
KPNO-1566	6709	71	83	$5050\sim 8300$	Hα narrow

We used 4 Hα narrow band filters for our emission line acquisition. They are WIYN-15, WIYN-16, KPNO-1565, and KPNO-1566, which are chosen to corresponds to heliocentric velocity of sample galaxies. We also chose WIYN-14, which is an intermediate band filter designed to sample the continuum in the vicinity of Hα. Properties of each filter are given by Table. 3.2.

For most sample galaxies, narrow band acquisition consists of two fifteen-minute exposures totaling thirty minutes. WIYN-14 images for continuum subtraction followed immediately after narrow band images with five-minute exposure time per pointing, totaling ten minutes. This pattern is applied all but one galaxy, which is F568-1 with 45-minute exposure of narrow band frames. Parameters of Hα observations are given with Table. 3.3.

Table 3.3. Parameters of Hα Observations

Galaxy	Date	Telescope/Instrument	Band	Exp.Time
D500-2	May 18 2004	WIYN 3.6m/MIMO	W14	10min
	May 18 2004	WIYN 3.6m/MIMO	W15	30min
D512-2	May 18 2004	WIYN 3.6m/MIMO	W14	10min
	May 18 2004	WIYN 3.6m/MIMO	W15	30min
D570-4	May 18 2004	WIYN 3.6m/MIMO	W14	10min
	May 18 2004	WIYN 3.6m/MIMO	W15	30min
D575-5	May 18 2004	WIYN 3.6m/MIMO	W14	10min
	May 18 2004	WIYN 3.6m/MIMO	W15	30min
D584-2	May 19 2004	WIYN 3.6m/MIMO	W14	10min
	May 19 2004	WIYN 3.6m/MIMO	W16	30min
D646-7	May 19 2004	WIYN 3.6m/MIMO	W14	10min
	May 19 2004	WIYN 3.6m/MIMO	W15	30min
DDO 189	May 17 2004	WIYN 3.6m/MIMO	W14	10min
	May 17 2004	WIYN 3.6m/MIMO	W15	30min
F561-1	Nov 19 2003	WIYN 3.6m/MIMO	W14	10 min
	Nov 19 2003	WIYN 3.6m/MIMO	KP1565	30 min
F563-V1	Nov 19 2003	WIYN 3.6m/MIMO	W14	10 min
	Nov 19 2003	WIYN 3.6m/MIMO	KP1565	30 min
F568-1	May 17 2004	WIYN 3.6m/MIMO	W14	15 min
	May 17 2004	WIYN 3.6m/MIMO	W15	45 min
F577-V1	May 17 2004	WIYN 3.6m/MIMO	W14	10min
	May 17 2004	WIYN 3.6m/MIMO	KP1566	30min
NGC 1560	Nov 19 2003	WIYN 3.6m/MIMO	W14	10 min
	Nov 19 2003	WIYN 3.6m/MIMO	W15	30 min
NGC 4455	May 18 2004	WIYN 3.6m/MIMO	W14	10min
	May 18 2004	WIYN 3.6m/MIMO	W15	30min
UGC 128	Nov 20 2003	WIYN 3.6m/MIMO	W14	10 min
	Nov 20 2003	WIYN 3.6m/MIMO	KP1565	30 min
UGC 334	Nov 20 2003	WIYN 3.6m/MIMO	W14	10 min
	Nov 20 2003	WIYN 3.6m/MIMO	KP1565	30 min
UGC 628	Nov 18 2003	WIYN 3.6m/MIMO	W14	15 min
	Nov 18 2003	WIYN 3.6m/MIMO	W15	30 min
UGC 731	Nov 20 2003	WIYN 3.6m/MIMO	W14	10 min
	Nov 20 2003	WIYN 3.6m/MIMO	W15	30 min
UGC 1230	Nov 19 2003	WIYN 3.6m/MIMO	W14	10 min
	Nov 19 2003	WIYN 3.6m/MIMO	KP1565	30 min
UGC 2259	Nov 18 2003	WIYN 3.6m/MIM O	W14	10min
	Nov 18 2003	WIYN 3.6m/MIMO	W15	300min
UGC 2885	Nov 20 2003	WIYN 3.6m/MIMO	W14	10 min
	Nov 20 2003	WIYN 3.6m/MIMO	KP1566	30 min
UGC 3371	Nov 19 2003	WIYN 3.6m/MIMO	W14	10 min
	Nov 19 2003	WIYN 3.6m/MIMO	W15	30 min
	Nov 20 2003	WIYN 3.6m/MIMO	W14	10 min
	Nov 20 2003	WIYN 3.6m/MIMO	W15	30 min
UGC 5750	May 19 2004	WIYN 3.6m/MIMO	W14	10min
	May 19 2004	WIYN 3.6m/MIMO	KP1565	30min
UGC 5981	Nov 20 2003	WIYN 3.6m/MIMO	W14	10 min
	Nov 20 2003	WIYN 3.6m/MIMO	W16	30 min
	May 19 2004	WIYN 3.6m/MIMO	W14	10min
	May 19 2004	WIYN 3.6m/MIMO	W16	30min
UGC 6151	May 17 2004	WIYN 3.6m/MIMO	W14	10min
	May 17 2004	WIYN 3.6m/MIMO	W15	30min
UGC 6614	May 19 2004	WIYN 3.6m/MIMO	W14	10min
	May 19 2004	WIYN 3.6m/MIMO	KP1566	30min
UGC 8837	May 18 2004	WIYN 3.6m/MIMO	W14	10min
	May 18 2004	WIYN 3.6m/MIMO	W15	30min
UGC 9992	May 17 2004	WIYN 3.6m/MIMO	W14	10min

Table 3.3 (cont'd)

Galaxy	Date	Telescope/Instrument	Band	Exp.Time
	May 17 2004	WIYN 3.6m/MIMO	W15	30min
UGC 10310	May 18 2004	WIYN 3.6m/MIMO	W14	10min
	May 18 2004	WIYN 3.6m/MIMO	W15	30min
UGC 11454	Nov 19 2003	WIYN 3.6m/MIMO	W14	10min
	Nov 19 2003	WIYN 3.6m/MIMO	KP1566	30min
UGC 11557	Nov 20 2003	WIYN 3.6m/MIMO	W14	10 min
	Nov 20 2003	WIYN 3.6m/MIMO	W15	30 min
UGC 11583	Nov 19 2003	WIYN 3.6m/MIMO	W14	10min
	Nov 19 2003	WIYN 3.6m/MIMO	W15	30min
UGC 11616	Nov 20 2003	WIYN 3.6m/MIMO	W14	10 min
	Nov 20 2003	WIYN 3.6m/MIMO	KP1566	30 min
UGC 11648	Nov 20 2003	WIYN 3.6m/MIMO	W14	10 min
	Nov 20 2003	WIYN 3.6m/MIMO	W16	30 min
UGC 11748	Nov 19 2003	WIYN 3.6m/MIMO	W14	10min
	Nov 19 2003	WIYN 3.6m/MIMO	KP1566	30min
UGC 11819	Nov 20 2003	WIYN 3.6m/MIMO	W14	10 min
	Nov 20 2003	WIYN 3.6m/MIMO	KP1565	30 min
UGC 11820	May 17 2004	WIYN 3.6m/MIMO	W14	10min
	May 17 2004	WIYN 3.6m/MIMO	W15	30min
	May 18 2004	WIYN 3.6m/MIMO	W14	5min
	May 18 2004	WIYN 3.6m/MIMO	W15	15min
UGC 11944	May 19 2004	WIYN 3.6m/MIMO	W14	10min
	May 19 2004	WIYN 3.6m/MIMO	W16	30min
UGC 12695	Nov 19 2003	WIYN 3.6m/MIMO	W14	10min
	Nov 19 2003	WIYN 3.6m/MIMO	KP1566	30min

3.2.2 Data Reduction

Data reduction for these Hα photometry followed standard procedures using IRAF, except preparatory procedures to eliminate known bad lines on CCD chips. These procedures are provided in Interactive Data Language (hereafter, IDL) codes provided by Dr. Abhijit Saha (ftp://taurus.tuc.noao.edu/pub/saha/MIMOfixes). These pre-procedures also flag saturated pixels to set up master bad pixel masks.

After processing images with these IDL codes, bias and dark current subtraction followed before flat fielding with dome flat frames is executed.

3.2.3 Astrometric Calibration

Astrometric calibration is performed by MSCGETCAT and MSCCMATCH tasks, which are included in MSCRED package for IRAF. However, MIMO images have a known error in WCS parameters of their headers. These images simply have 180-degree rotated WCS values. This can be corrected with a simple MSCWCS task execution. After MSCWCS runs, MSCGETCAT and MSCCMATCH tasks followed.

3.2.4 Photometric Calibration

Spectrophotometric standard stars are available in the literatures (e.g.Massey et al. 1988; Oke 1974; Stone 1996). We chose several standard stars which were above the horizon at acquisition time.

We measure zeropoints for each exposure and plot for each observing night, standard star, and filter. There is not much variation, or trend between each filter, even for WIYN-14. Each night gives pretty consistent zeropoints as well, except May 17 2004, which is the first night of the run.

Although these measurements provide consistent zeropoints, we decided not to use extinction coefficients. Very well-defined photometric correlation of airmass for May 2004 run, shows reverse correlations (zeropoints increasing with increasing airmass), while November 2003 run has a too steep slope (Fig.3.1).

Although it actually shows very reasonable fit (Fig.3.1 (c)) by combining two sets of photometric zeropoints, we decided to use averages of zeropoints separately, since the observing runs happened to be too far apart.

Therefore, spectrophotometric calibration relations are;

$$M_\nu - m_\nu \quad = \quad 22.674 \pm 0.216 \tag{3.1}$$

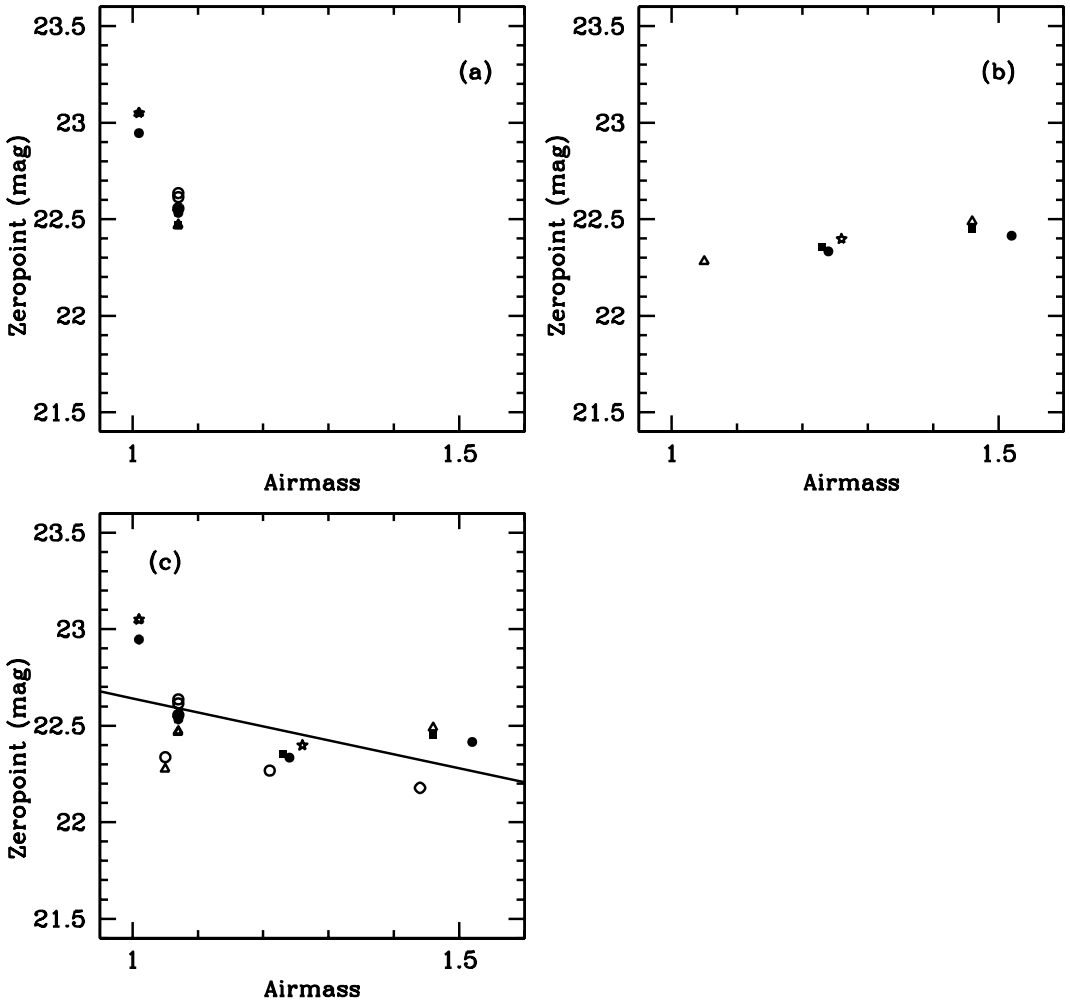

Figure 3.1: Plots for photometric calibration of Hα observation.
(a) Photometric zeropoints versus airmass for November 2003
(b) Photometric zeropoints versus airmass for May 2004
(c) Combined zeropoints from two runs.
Each symbol represent a filter as follows: empty circle W14, empty triangle W15, filled square W16, empty star KP 1565, filled circle Kp1566.

for November 2003 run, and

$$M_\nu - m_\nu \quad = \quad 22.349 \pm 0.088 \tag{3.2}$$

for May 2004 run, respectively.

The conversion of these magnitudes to flux units is given as

$$m_\nu \quad = \quad -2.5 log f_\nu - 48.59, \tag{3.3}$$

where f_ν is in units of ergs cm^{-2} s^{-1} Hz^{-1} (Oke 1974). This conversion is based on the Hayes & Latham (1975) calibration with the magnitude of Vega being 0.04 at 5556 $\AA$.

3.2.5 Continuum Subtraction

As mentioned in 3.2.1, we chose WIYN-14 Hα continuum filter to subtract continuum from narrow band images. In order to scale the flux of the much broader continuum filter to that of the narrow band Hα filter, we picked about 20 stars from each galaxy image. Generally we picked stars throughout two amplifiers around target galaxies, so that each amplifier has about 10 stars each.

Using a basic photometry IRAF task, namely, PHOT, we measured flux of those stars for narrow band images and continuum images. We used 3$''$ aperture, which corresponds to 21 pixel aperture. We applied the aperture correction, which we acquired from curves of growth for standard stars.

After we calculated ratios between two fluxes of each star, we picked a median of those values to scale the continuum images. After the sky levels were subtracted from narrow band images and continuum images, narrow band images were subtracted by scaled continuum images. This matches the continuum level, but the line emission contamination is still a concern, since the Hα emission line does fall within the

bandpass of the continuum filter. In order to solve this, we adapted the recursive technique used by Schmitt et al. (2006). A subtraction of simple scaled continuum image from the line image will underestimate the total Hα flux, since the broad filter images are contaminated by line emission.

The recursive subtraction was done as follows. The narrow band image is subtracted by the scaled continuum image first. Then, in order to eliminate contribution from the emission line to the continuum image, the resulting line image was scaled and subtracted from the continuum image. The corrected continuum image was subtracted from the original line image.

This process was repeated a few times, until the Hα and continuum fluxes varied less than 0.5% between consecutive iterations. Like Schmitt et al. (2006), generally, 2-3 iterations sufficed to reach this goal.

3.3 Results

3.3.1 Hα Photometry

Contamination by [NII] λ6548, 6584 is also a concern for our measurement of Hα flux. There is no [NII]/Hα ratio available from spectroscopy for our sample galaxies. Still, there is a correction relationship derived by Jansen et al. (2000), and reconfirmed by Helmboldt et al. (2004):

$$log\frac{[NII]}{H\alpha} = [-0.13 \pm 0.035]M_R + [-3.2 \pm 0.90], \quad (3.4)$$

where M_R is the absolute magnitude in the R-band.

Hα extinction correction is also available using the equation used by Helmboldt et al. (2004):

$$log(H\alpha)_{int} = [-0.12 \pm 0.048]M_R + [-2.5 \pm 0.96]. \quad (3.5)$$

However, there are sample galaxies which do not have R-band photometry data available. For these galaxies, we simply used the observed ratio from the spectra of similar LSBGs inde Naray et al. (2004) which is [NII]/H$\alpha \sim 0.1$. We found that [NII]/Hα values calculated by Eq.3.4 are generally [NII]/H$\alpha \approx 0.1$.

3.3.2 Star Formation Rates

The most commonly used conversion between Hα luminosity and star formation rate is given by, Kennicutt et al. (1994):

$$SFR(M_{\odot} yr^{-1}) \quad = \quad 7.937 \times 10^{-42} L(H\alpha), \tag{3.6}$$

assuming a Salpeter initial mass function (IMF) (Salpeter 1955) and solar abundances, where L(Hα) is in the unit of erg s^{-1}. Additionally, Kennicutt et al. (1994) provides conversion factors using different IMFs, such as Kennicutt (1983) and Kroupa et al. (1993) IMFs. Kennicutt et al. (1994) shows that the Kennicutt (1983) IMF or a Salpeter IMF provide reasonable fits to its observed EW-color relation.

However, Bell et al. (2003) claims that a Salpeter IMF is too rich in low mass stars, resulting in higher mass-to-light (M/L) ratio at a given color and adopted a "diet" Salpeter IMF that has the same colors and luminosity as a normal Salpeter IMF, but with only 70% of the mass due to a lower number of faint low-mass stars.

Therefore, we should be aware of the difference of IMFs while comparing SFRs and stellar masses. We provide SFRs converted by Eq. 3.6 for this Chapter.

For 19 sample galaxies, the average Hα luminosity is 1.75×10^{42} erg s^{-1}. This is severely skewed due to a couple of galaxies, namely UGC 2885 and UGC 6614. Both galaxies are fairly large galaxies in terms of exponential disk profiles. UGC 2885 also has an intermediate surface brightness and does not fit into the definition of LSBGs. The median Hα luminosity is 4×10^{40} erg s^{-1}. This corresponds to the star formation rate of 0.30 M$_{\odot}$ yr^{-1}.

Table 3.4. Results of Hα Photometry

Galaxy	Hα Flux (10^{-13} ergs cm^{-2} s^{-1})	Hα Flux$_c^{\dagger}$	Hα Luminosity ($10^{38} ergs^{-1}$)	SFR‡ ($M_\odot$ yr^{-1})	Eq.Width§ Å	B (mag)	B-V (mag)	K_s (mag)
D512-2	0.77	0.70	11±30	0.009±0.026	2±9			-18.67
D570-4	0.41	0.37	9.5±1.7	0.008±0.0009	1.5±15			
D584-2	1.62	1.47	235±42	0.19±0.034	7±2	-16.10	0.1	-17.78
F568-1	0.11	0.09	93±185	0.07±0.14	4±9	-18.31	0.6	-21.68
F577-V1	3.3	2.9	4005±465	3.18±0.37	17±5	-17.97	0.11	-17.26
NGC 4455	54.7	49.7	460±50	0.37±0.04	21±5	-18.44	0.1	-24.67
UGC 128	37.1	30.3	14340±1300	11.4±1.1	4±2	-18.84	0.66	-22.70
UGC 334	0.06	0.05	24±2	0.02±0.002	5±4	-18.64	0.7	-23.45
UGC 731	22.8	20.7	196±25	0.16±0.02	9±5	-17.12	0.34	-19.55
UGC 1230	50.3	45.7	15500±165	12.3±1.3	11±5	-17.49	0.54	-21.04
UGC 2259	53.8	48.8	383±35	0.30±0.03	22±3	-15.70		-20.41
UGC 2885	375	341	261000±2500	210.4±21.1	17±5	-22.80	0.47	-26.26
UGC 6614	34.0	24.6	22870±2400	18.2±1.9	5±1	-19.92	1.38	-23.99
UGC 8837	109.3	99.4	172±12	0.14±0.01	15±5	-14.46	0.43	-17.28
UGC 9992	8.7	7.9	74±7	0.06±0.006	10±3	-15.02	0.37	-17.08
UGC 10310	84.0	76.4	896±55	0.711±0.07	27±3	-17.20	0.38	-19.27
UGC 11557	77.6	70.5	3140±250	2.5±0.2	29±5	-19.71		-21.69
UGC 11820	3.4	3.1	86±50	0.07±0.04	12±5	-17.70	0.5	-18.70
UGC 12695	11.6	10.6	9340±1000	7.4±0.8	19±3	-17.27	0.25	-22.17

Note. — † : [NII] emission and Hα intrinsic extinction corrected. ‡ : Based on Salpeter IMF only. § : The ratio of total Hα flux to Hα subtracted continuum

The basic results of Hα photometry is given in Table. 3.4.

3.3.3 Luminosity Dependence of Star Formation Rate

Generally, there is no strong correlation between galaxy luminosity and star formation rate (Figs.3.2 (a) and (b)). Both B-band and K_S-band magnitude do not dominate any trend in star formation rate, although the two galaxies with high star formation rate are luminous in the B-band. However, this trend is more of the obvious fact that large galaxies are luminous.

Still, F577-v1 is surprisingly dim in the K_S-band. Although this galaxy is obviously detected, its well recognized features in optical bands are not seen in the K_S-band. Therefore, it is plausible that the outside structure of F577-v1 fall below detection limit of K_s-band observation and was lost.

3.3.4 Color Dependence of Star Formation Rate

The star formation rate does not show any strong correlation with color for our sample galaxies (Figs.3.2 (c) and (d)). Other than formerly mentioned galaxies, F577-v1 and UGC 6614, there is not a unique feature along their relationships.

It is easy to presume that young (blue) galaxies produce more young stars, which is not the case with our sample, although it is possible that low metallicity causes the small B-K_S color generally forming fewer stars.

On the other hand, UGC 6614 is obviously red, both in optical color and near-infrared combined color. This galaxy is forming stars with a surprisingly high rate for a large LSBG, which are considered to be old and a little different from classical LSBGs. Actually, UGC 6614 has a higher star formation rate than every large LSBGs measured for star formation rate by O'Neil et al. (2007b). Since there is no distinctive characteristic of UGC 6614 from surface brightness analysis, which is different from those sample galaxies of O'Neil et al. (2007b), there should be some other physical factors in driving its star formation.

3.3.5 Structure Parameters and Star Formation Rate

Structure parameters, such as central surface brightness and exponential disk scale length, do not govern star formation rate, either. While gas mass density has a strong correlation with the star forming process and its efficiency (O'Neil et al. 1998), visible light representing formed stars seem to have a weak correlation with current star formation rate.

Table 3.5. Correlation Matrix of SFR

	M_B	M_V	B-V	B-K_s	mu_B	μ_{Ks}	h_B	h_{Ks}
SFR	-0.63	-0.52	0.21	0.15	-0.62	-0.42	0.48	0.57

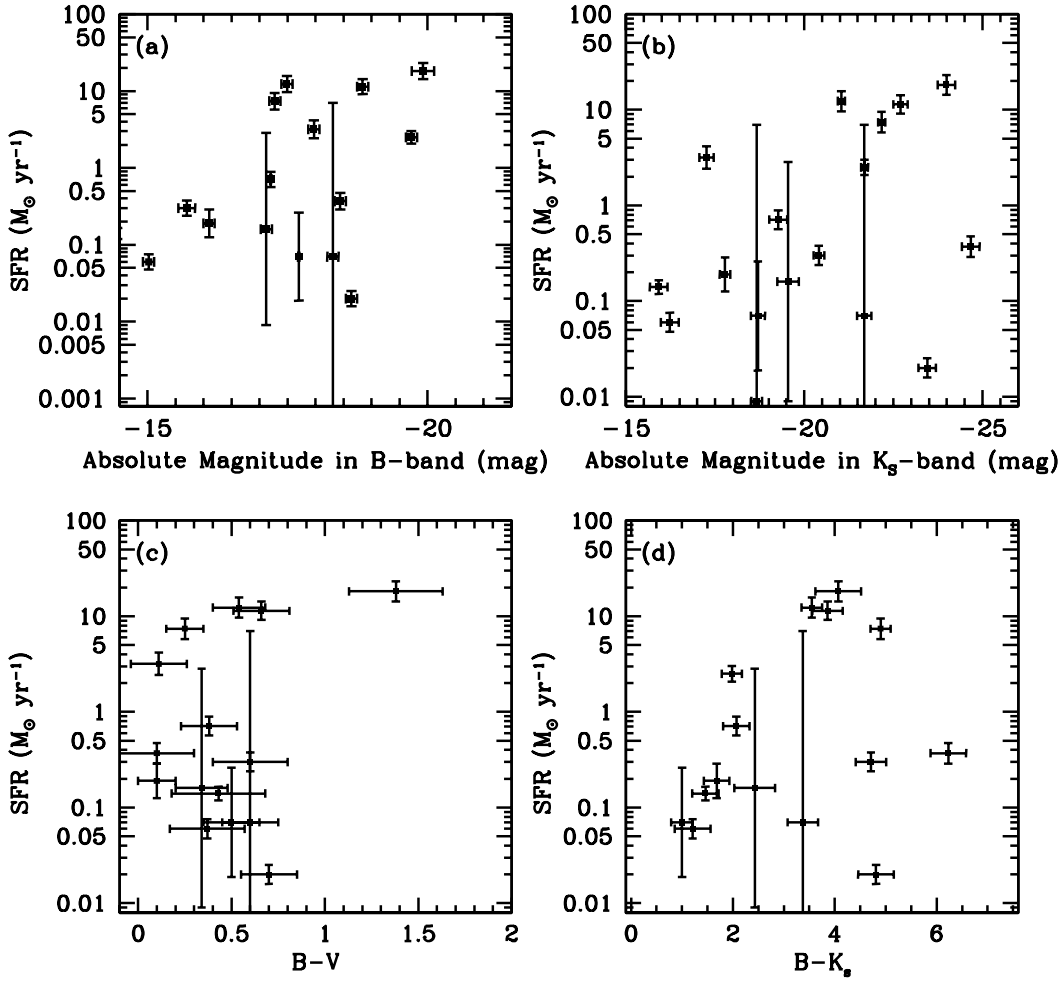

Figure 3.2: Star formation rate versus luminosity and colors. (a) B-band luminosity versus SFR (b) K_s-band luminosity versus SFR (c) B-V versus SFR (d) B-K_s versus SFR.

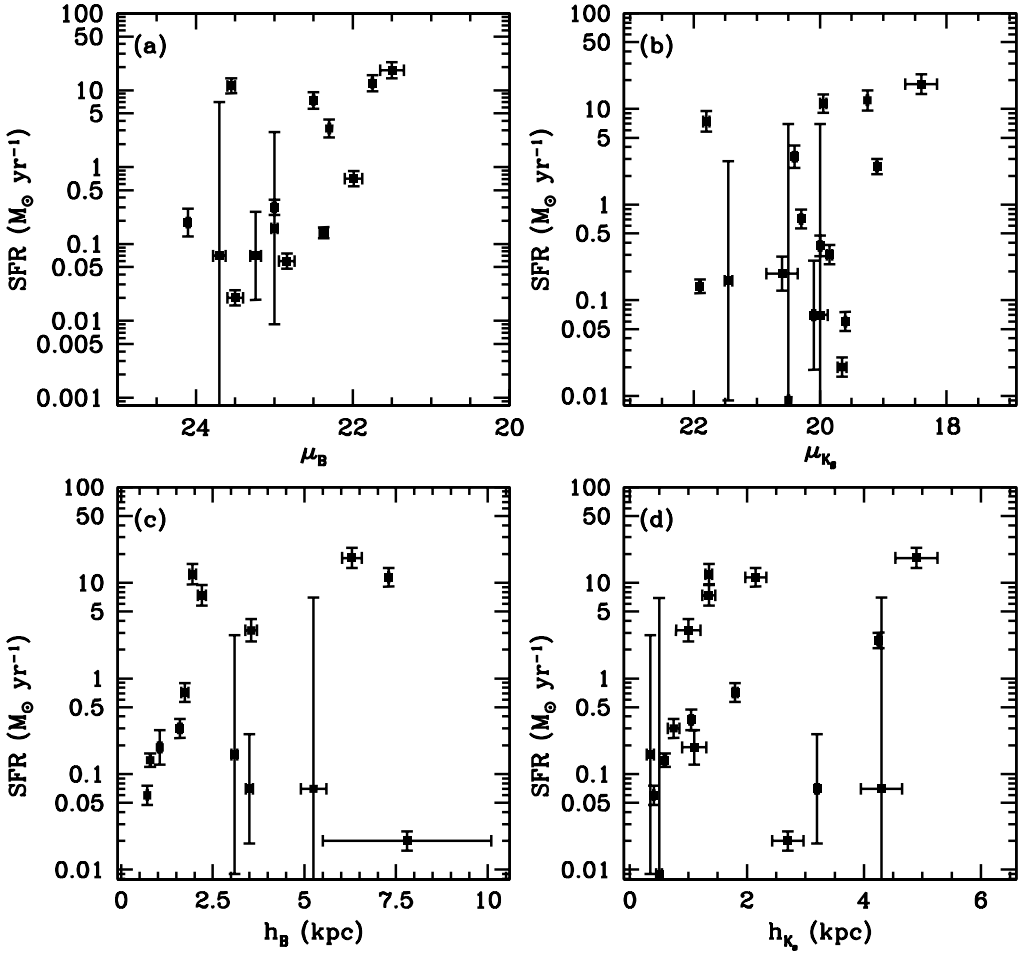

Figure 3.3: Structural parameters versus SFR. Left panels are for B-band parameters and right panels are for K_s-band parameters.
(a) B-band central surface brightness versus SFR (b) K_s-band central surface brightness versus SFR (c) B-band disk scale length versus SFR (d) K_s-band disk scale length versus SFR.

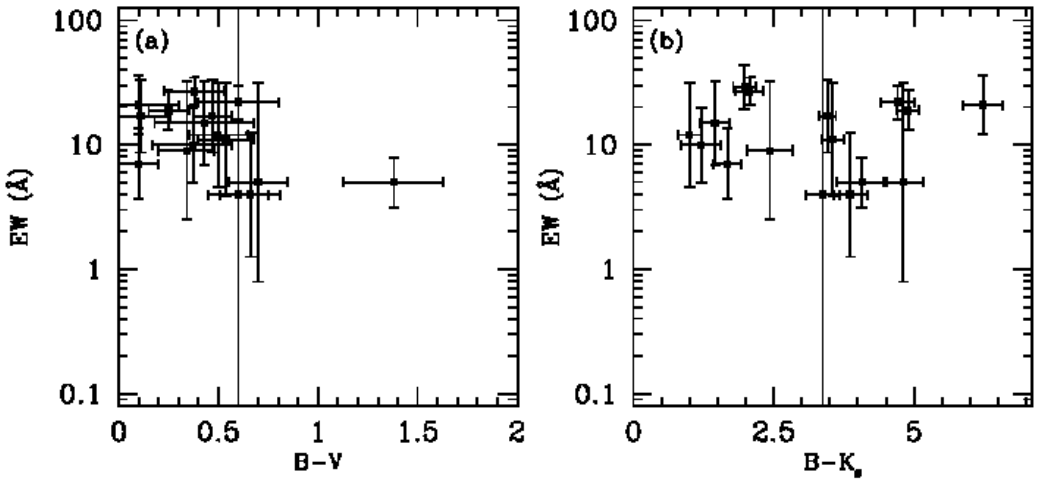

Figure 3.4: Equivalent width versus color plots for sample galaxies.
(a) EW versus B-V (b) EW versus B-K_s

3.3.6 Equivalent Width-Color Relationship

Our equivalent width (EW) is simply the ratio of the total Hα flux to total scaled continuum flux within narrow-band image. Generally our sample LSBGs have pretty low equivalent width values. The average equivalent value is 12.5Å. Our sample galaxies do not show any strong trend between their equivalent widths and other physical parameters, such as luminosity, colors, SFRs and so on (Figs.3.4).

The H EW and color can be used to measure the ratio of the current SFR to the average past SFR, the Scalo b parameter Kennicutt et al. (1994). O'Neil et al. (2007a) also showed that their large LSBG disks do not show strong correlations with colors, or absolute magnitude.

3.3.7 HII Region Luminosity Function

The HII region luminosity function (LF) is an important diagnostic of star formation properties of galaxies, since HII regions are a primary indicator of high-mass star formation. The differential HII LF is parameterized as a power law:

$$N(L)dL \;\; = \;\; AL^{-a}dL, \tag{3.7}$$

where $N(L)dL$ is the number of the nebulae with luminosities in the range L to $L + dL$. The form of HII LFs have been linked to various properties of massive star formation in galaxies. For example, many galaxies show a break in slope of their HII LFs (Kennicutt et al. 1989; Rand 1992; Walterbos & Braun 1992), which has been suggested to be caused by a transition between normal HII regions and the super giant HII regions. Typically this break is around $L(H\alpha) = 38.6$ dex (Kennicutt et al. 1989), below which slope is flatter. On the other hand, the difference in slope for arm versus interarm HII regions, and among Hubble types has been attributed to different gasdynamics and molecular cloud mass spectrum (Kennicutt et al. 1989; Rand 1992). Therefore it is interesting to see if HII LFs of LSBGs look similar to those of normal galaxies.

However, out of 19 sample galaxies, only UGC 11557 has about 50 HII regions and only four other galaxies have more than ten distinctive HII regions. They are NGC 4455, UGC 2259, UGC 8837, UGC 10310, and UGC 11557. It is difficult to derive LFs of HII regions for individual galaxies when they have only a handful of HII regions. Therefore we present a composite HII region LF (Fig.3.5). This histogram consists of HII regions from our entire sample galaxies. The shaded histogram only represents HII regions of UGC 11557 which has the most HII regions.

We found that our HII region LF has slope similar to the typical value of a$\sim$2 for the higher luminosity end. However, our break occurs at higher luminosity ($\sim 5\times10^{39}$

erg s^{-1}) than the typical observed values. The lower end of the LF lacks HII regions and flattens. These findings can be attributed to a couple explanations.

First of all, we simply miss out many less luminous HII regions. Generally, typical observed HII LFs reach into L = 10^{37} erg s−1. We do not have any HII region which has luminosity reaching the range. Our sample LSBGs have a wide range of distances making the limiting flux correspond to a wide range of H luminosities. We do not have complete HII regions between $10^{37} \sim 10^{38}$ erg s^{-1}. Secondly, LSBGs may have a different evolution of the ionizing stars in the clusters. Oey & Clarke (1998) show that stellar mass ranges, and possibly slopes of IMFs changes breaks of HII LFs. They also claimed that stellar parameters within the sparse cluster will result in more substantial variations of the form of the HII LFs. In particular, for "unsaturated population" for which small number statistics determine the relative ionizing contribution of different stellar masses, the HII LF slopes tend to be flatter, while do not fully reflect the parent slope in IMFs (McKee & Williams 1997). These factors mitigate against a clear distinction between the LSB HII LF and that of brighter galaxies. The observed difference may be real, but it seems plausibly explained by a combination of sample in completeness and LSBGs sporadically sampling the parent HII LF. Bear in mind, after all, that our LF is the composite of many LSBGs, some of which have many HII regions, but most of which have only one or a few.

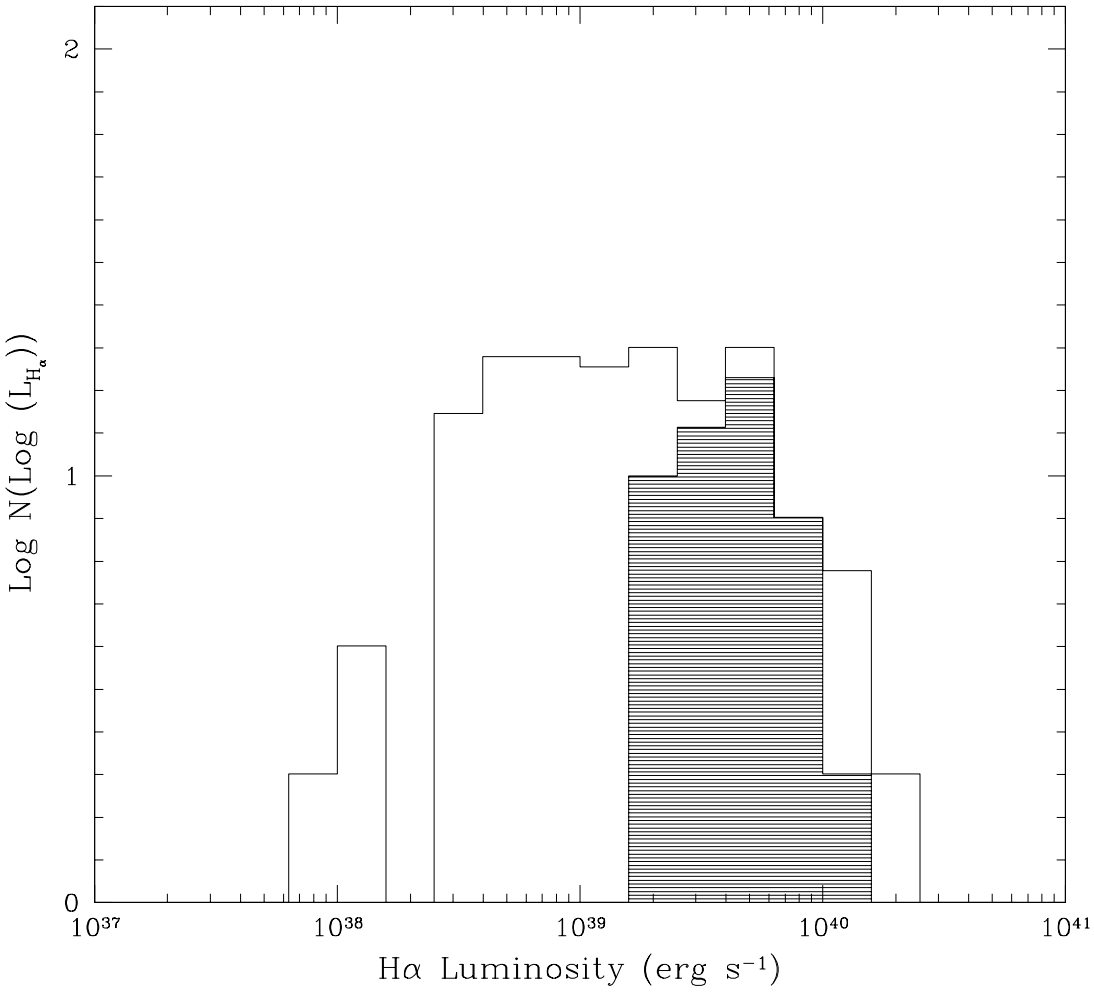

Figure 3.5: A composite luminosity function of HII regions from the entire sample. A shaded histogram represents HII regions from UGC 11557 which has most HII regions among our sample galaxies. Notice that our break ($\sim 10^{40}$) is higher than that of HII LF for normal galaxies.

3.4 Morphology of Hα Emission

We present the Hα images of sample galaxies along with available multicolor optical CCD images.

D512-2

Blocked by a foreground star, this galaxy still has diffuse Hα emission around its central region (Figs.3.6 (a),(b), and (c)). Considering its elongated shape from optical broadband images, its Hα emission comes from a very small area.

D570-4

This amorphous galaxy shows very weak diffuse Hα emission, but has an HII region which is southeast to the center (Figs.3.6 (d),(e), and (f)).

D584-2

This small irregular galaxy has Hα knots throughout its central region (Figs.3.6 (g),(h), and (i)). As mentioned before, this galaxy can be an example of low surface brightness spiral galaxies, which are hidden below sky noise. From optical broadband images, it is easy to recognize a spiral-like feature onto northeastward, which has some Hα emission along it.

F568-1

A very similar case to D584-2, this galaxy has even lower surface brightness than the former one (Figs.3.7 (a),(b), and (c)). It has very weak diffuse Hα emission around its central region. Due to its fairly large distance, error on its flux measurement is big. Therefore this value should be only considered as a higher limit of Hα flux of this galaxy.

F577-V1

This very dim galaxy, hinting a bar feature and spiral arms, has two obvious star forming regions, one in its center, and the other, where its bar-like feature and a spiral arm meet (Figs.3.7 (d),(e), and (f)). There are also some hints for HII regions on the spiral arm. Wich continuum subtracted, this galaxy looks to have a star forming ring with strong star forming activity in its center. As one of more distant galaxies ($\sim$ 100 Mpc), even deeper and higher resolution data would be desirable.

NGC 4455

Throughout its body, this galaxy has a lot of Hα knots and diffuse emission (Figs.3.7 (g),(h), and (i)). Due to its short distance, it also shows many distinctive HII regions unlike other sample galaxies. Interestingly, HII regions and diffuse emission are not concentrated around its center, rather scattered around a rim around the center. Note that this is a high surface brightness galaxy for comparison.

It also shows a feature, which it shows in other optical broadband images. There is a distinctive gap between outer southwest disk and the rest of disk. Even diffuse emission almost disappears in the gap. There is no apparent companion for this galaxy, therefore the mechanism should have arisen within the galaxy. Kinematics information should provide more physical background to this phenomenon.

UGC 128

Star formation is concentrated around its center (Figs.3.8 (a),(b), and (c)). It has one distinctive HII region which is located on a spiral arm right north to its center.

UGC 334

Hα is almost nonexistent, although it shows a little bit of hint at its nucleus region (Figs.3.9 (a),(b), and (c)). Among 19 galaxies presented in this chapter, this galaxy has a lowest level of Hα flux. Considering its small nucleus, a bar-like feature, and loose spiral arms, this is a bit surprising. It may be attributed to its distance.

UGC 731

UGC 731 has a weak asymmetric structure with its spiral arms, although its bar stands out (Figs.3.8 (g),(h), and (i)). There is no eminent Hα detection on the bar. All distinctive HII regions are located on its eastern spiral arm, in particular where the spiral arms meets the bar.

UGC 1230

UGC 1230 does not show any interesting feature in its continuum image (Figs.3.9 (d),(e), and (f)). Once continuum subtracted, even its central region does not have strong Hα emission. However, three very bright HII regions stand out. They are not associated with any particular feature of UGC 1230, since its structure is simply too ambiguous to perceive. Two HII regions are northeast to its center and the other is south to the center.

UGC 2259

HII regions are abundant in UGC 2259 (Figs.3.9 (g),(h), and (i)). However, there is little star formation in interarm regions, although continuum and narrow-band images show diffuse in these regions. HII regions are distributed evenly along its spiral arms.

UGC 2885

A SAc-type galaxy is an intermediate surface brightness galaxy which has a moderate size of bulge and shows dust lane features in its interarm regions (Figs.3.8 (d),(e), and (f)). It has a bright foreground star sitting on its northeast edge of spiral pattern.

It has massive star forming going on its spiral arms. Even with its large distance ($\sim$ 80 Mpc), it does show lots of distinctive star forming regions along its spiral pattern. They appear to be avoiding dust lanes.

UGC 6614

As one of the biggest low surface brightness disk galaxies, this one is relatively red in optical colors ($B - V > 1$) (Figs.3.10 (a),(b), and (c)). Still, it shows very impressive Hα features. First of all, prominent Hα emission only appear in its center and its ring-like feature, which encircles its center with a radius of $50''$. This radius corresponds to 22 kpc at the distance assumed.

Das et al. (2006) detected weaks CO signal on its disk and this detection was made about $40''$ west to the nucleus. Since the signal was weak and it is still slightly inside the ring, we can not confirm that the ring is associated with this dection.

Its very transparent disk, and its spiral arms do not show any Hα emission. Also, its large bulge only has very compact Hα emission area considering the size of its

bulge.

UGC 8837

This amorphous LSB galaxy has HII regions throughout its body, like NGC 4455 (Figs.3.10 (d),(e), and (f)). The difference between these two galaxies is the lack of diffuse emission for UGC 8837. Still like NGC 4455, UGC 8837 has its HII regions around outer disk-like feature, not around its central region. Including a big blob in its northeastern wing, this galaxy has more than 10 HII regions.

UGC 9992

With asymmetric spiral arms, this galaxy does not show strong concentration of Hα emission (Figs.3.10 (g),(h), and (i)). Eminent blobs along northwest and southeast spiral arms in the K_s- band image, which look like HII regions, disappears quickly in the Hα image. Most Hα flux comes from diffuse emission around its central region.

UGC 10310

With continuum subtracted, this galaxy looks more like a bar galaxy compared to its optical broadband images (Figs.3.11 (a),(b), and (c)). It has many distinctive Hα emission blobs along its central bar-like feature and its two spiral arms. Still its HII regions are more prominent along its spiral arms than around its center. In particular there is a huge Hα blob southeast of its central region.

UGC 11557

UGC 11557 has an intermediate size bulge which looks elongated a little (Figs.3.11 (d),(e), and (f)). HII regions are located across its disk. Their distribution does not show any trend favoring any angle or radius, although slightly larger HII regions are located around its edge of disk. It does not have any strong Hα emission from its center.

UGC 11820

This amorphous dwarf galaxy has a few Hα emitting feature hidden in its body, although they are weak and vague (Figs.3.11 (g),(h), and (i)).

UGC 12695

Probably the most peculiar galaxy among sample galaxies, UGC 12695 also has a very unique star forming feature (Figs.3.12 (a),(b), and (c)). Around its distorted center, there is diffuse structure. This structure looks like very dim spiral arms. However certainly there is no Hα emission coming out of these regions. About 35$''$ apart from its center, there are several Hα knots both east and west to the center. Overall, it resembles a butterfly which has stars forming on its wingtips.

Interestingly, but surely coincidingly, there is a background galaxy in each direction around those Hα knots.

3.5 Discussion

We have presented results from Hα photometry of 19 LSBGs. Although they have very low Hα luminosity and consequently very low star formation rates, there are several sample LSBGs which have relatively higher values, as much as their higher surface brightness counterparts. Unfortunately, those galaxies with higher Hα luminosity do not posses lots of common characteristists. Their optical and NIR luminosities along with colors and sizes do not control current star forming activity of LSBGs. Therefore, we have to wonder what causes them to have higher star forming rate than other LSBGs and still have low surface brightness? Furthermore, have they been sustaining this star forming rates which are similar to those of high surface brightness galaxies over long periods?

These questions are not easy to answer given the wide range of physical parameters of sample galaxies. Here, rather than giving definite answers to these questions, we will simply elaborate questions a little further.

LSBGs are known to have high gas mass fraction (de Blok et al. 1996; McGaugh & de Blok 1997), which means that they have large amounts of gas to turn into stars intact. However, if those LSBGs with SFRs similar to HSBGs had had extended star forming activity while sustaining low surface brightness and blue colors, they should have consumed decent amounts of gas and turned them into stars. It is not evident, at least, from our sample galaxies. Those galaxies with high SFRS also have higher gas mass fractions.

Therefore, it is likely that these LSBGs have episodic star formation histories (SFHs). During the recent past, these galaxies have had lapses between bursty, or nonbursty star formation events after they have had long quiescent periods. We also have tools to look into this question a little bit further. With optical and NIR

photometry and colors available, we can constrain old stellar masses which have been assemble over the Hubble time. We will talk about it in Chap.4.

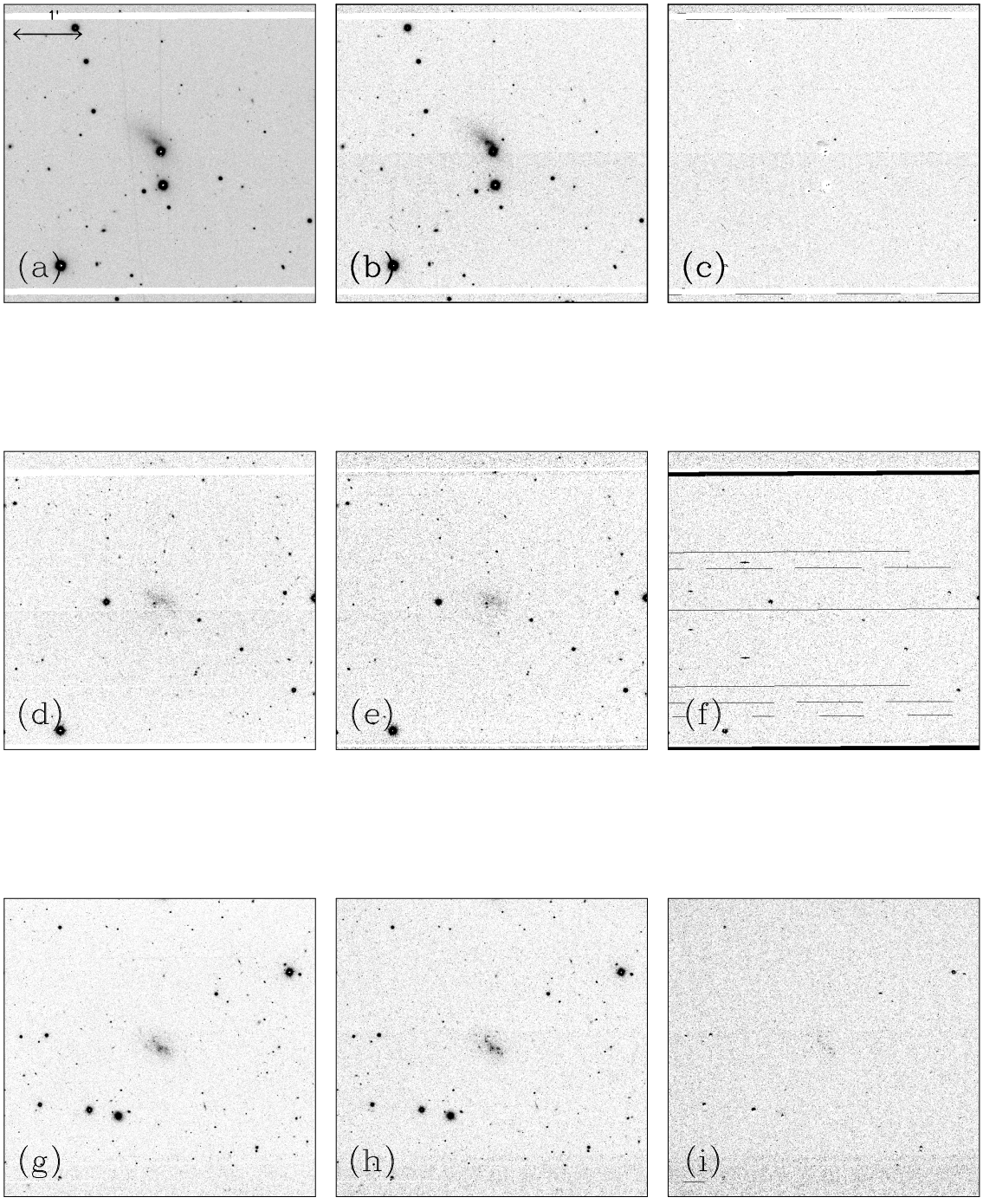

Figure 3.6: Hα images of D512-2, D570-4, and D584-2. North is up and East is left. Intensity levels are adjusted arbitrarily in order to show the galaxy best. The bar on the upper left corner in (a) frame shows $1'$.
Images in the same line are for a same galaxy. The first column is for continuum image, the second column is for Hα narrow band image before continuum subtraction. continuum subtraction.
(a) D512-2 continuum (b) D512-2 Hα (c) D512-2 Hα after continuum subtraction
(d) D570-4 continuum (e) D570-4 Hα (f) D570-4 Hα after continuum subtraction
(g) D584-2 continuum (h) D584-2 Hα (i) D584-2 Hα after continuum subtraction.

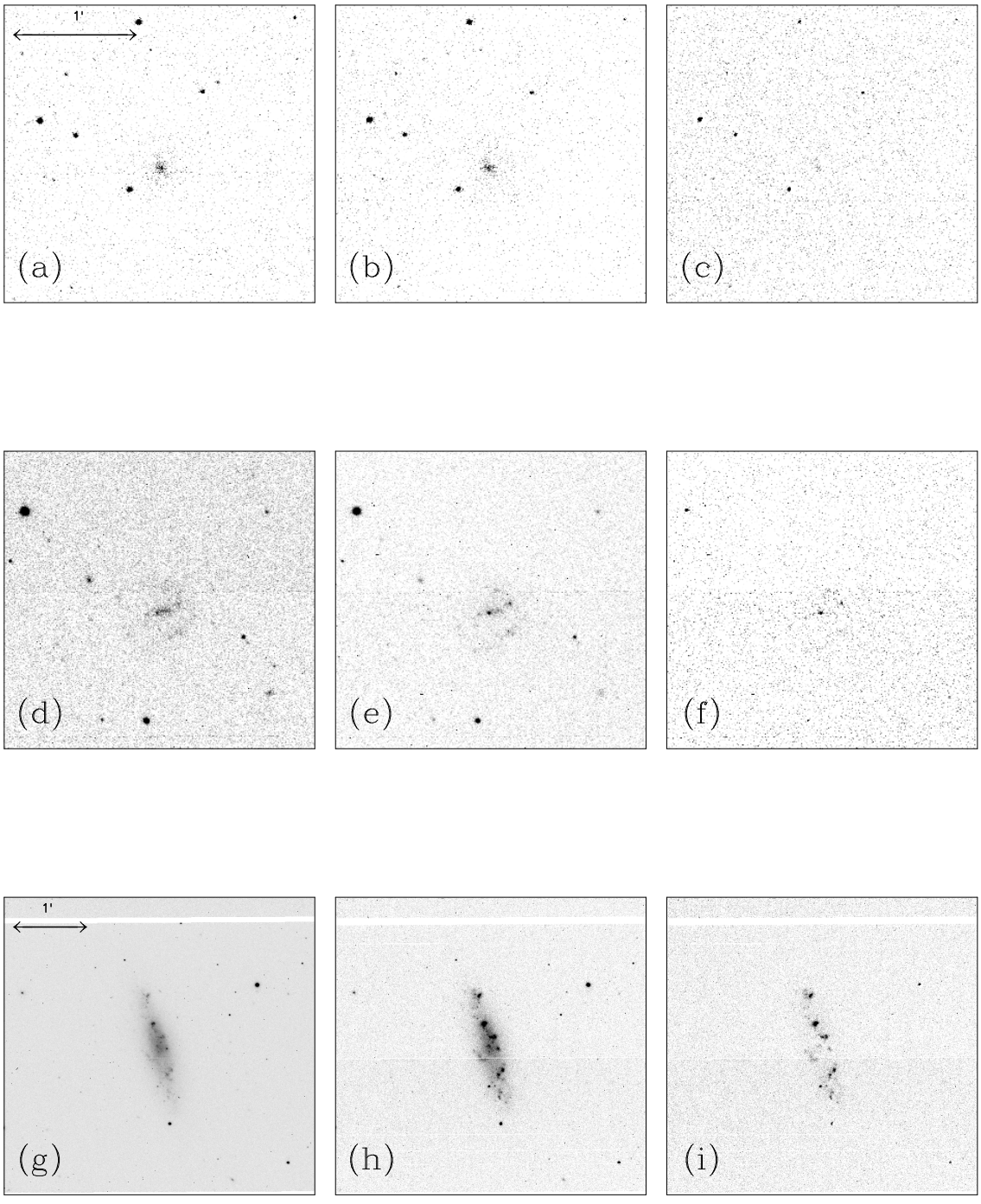

Figure 3.7: Hα images of F568-1, F577-v1, and NGC 4455. North is up and East is left. Intensity levels are adjusted arbitrarily in order to show the galaxy best. The bars on the upper left corner in (a) frame and (g) frame show $1'$.
Images are in the same order as Fig. 3.6
(a) F568-1 continuum (b) F568-1 Hα (c) F568-1 Hα after continuum subtraction (d) F577-v1 continuum (e) F577-v1 Hα (f) F577-v1 Hα after continuum subtraction (g) NGC 4455 continuum (h) NGC 4455 Hα (i) NGC 4455 Hα after continuum subtraction.

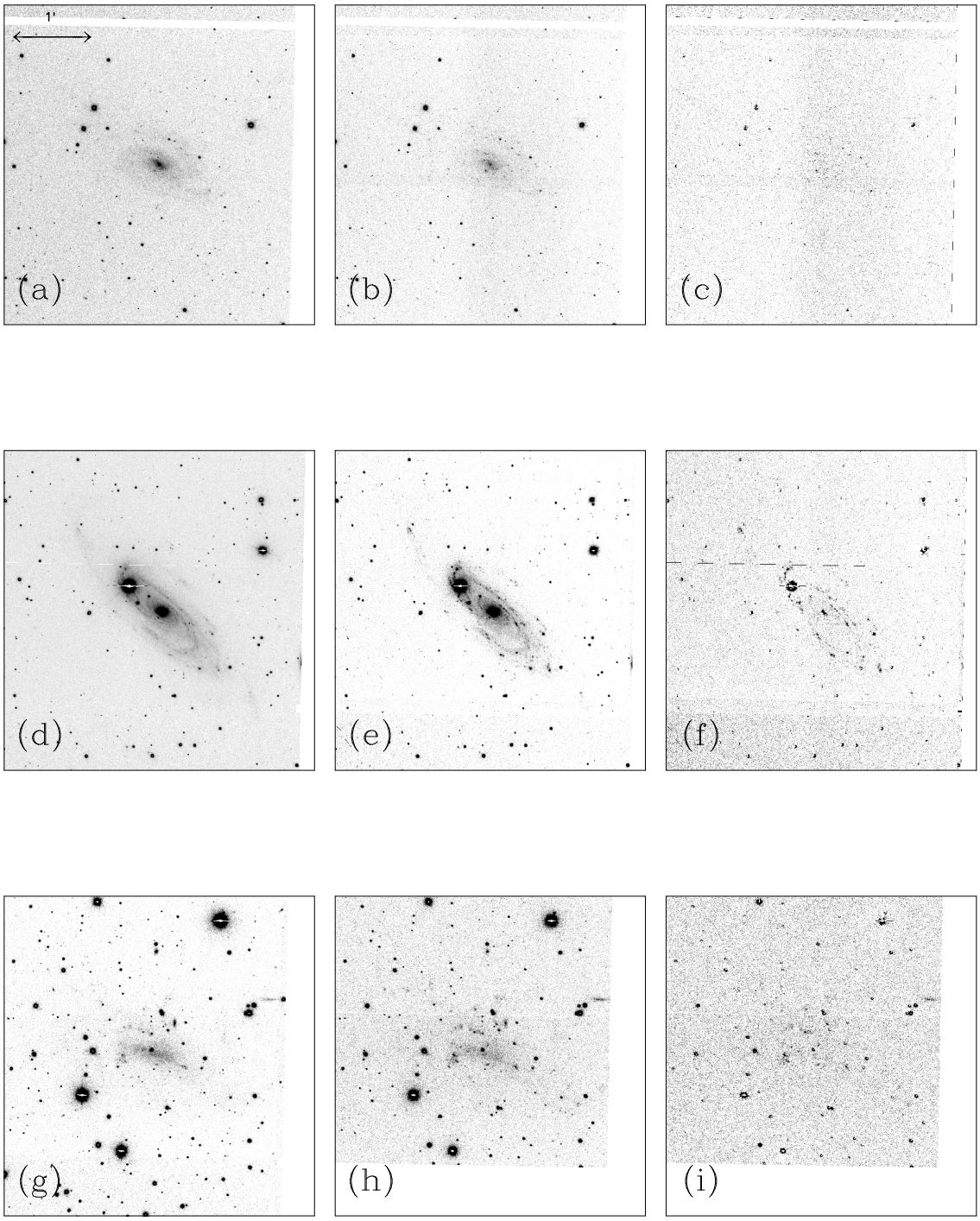

Figure 3.8: Hα images of UGC 128, UGC 2885, and UGC 731. North is up and East is left. Intensity levels are adjusted arbitrarily in order to show the galaxy best. The bar on the upper left corner in (a) frame shows $1'$.
Images are in the same order as Fig. 3.6
(a) UGC 128 continuum (b) UGC 128 Hα (c) UGC 128 Hα after continuum subtraction (d) UGC 2885 continuum (e) UGC 2885 Hα (f) UGC 2885 Hα after continuum subtraction (g) UGC 731 continuum (h) UGC 731 Hα (i) UGC 731 Hα after continuum subtraction.

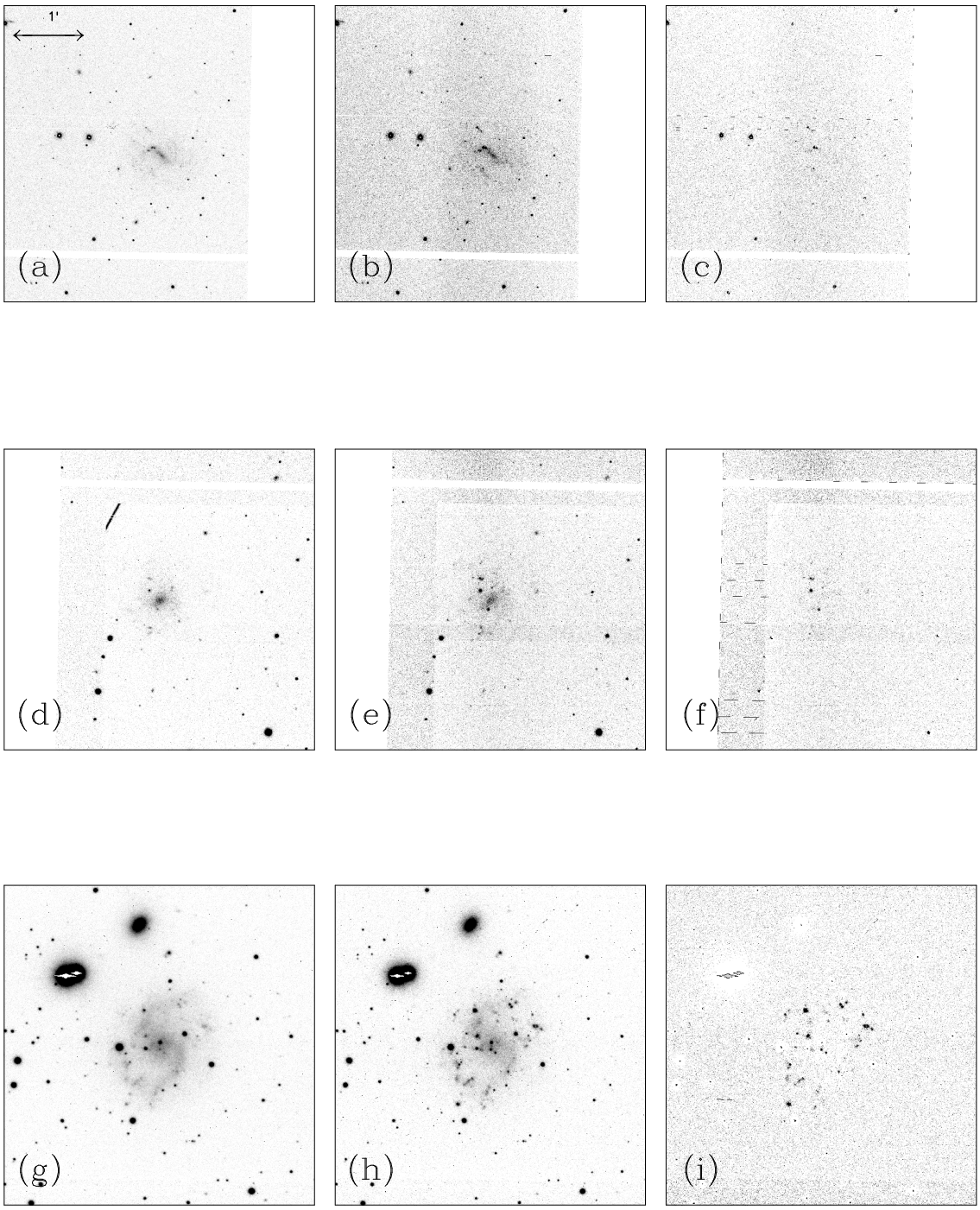

Figure 3.9: Hα images of UGC 334, UGC 1230, and UGC 2259. North is up and East is left. Intensity levels are adjusted arbitrarily in order to show the galaxy best. The bar on the upper left corner in (a) frame shows $1'$.
Images are in the same order as Fig. 3.6
(a) UGC 334 continuum (b) UGC 334 Hα (c) UGC 334 Hα after continuum subtraction (d) UGC 1230 continuum (e) UGC 1230 Hα (f) UGC 1230 Hα after continuum subtraction (g) UGC 2259 continuum (h) UGC 2259 Hα (i) UGC 2259 Hα after continuum subtraction.

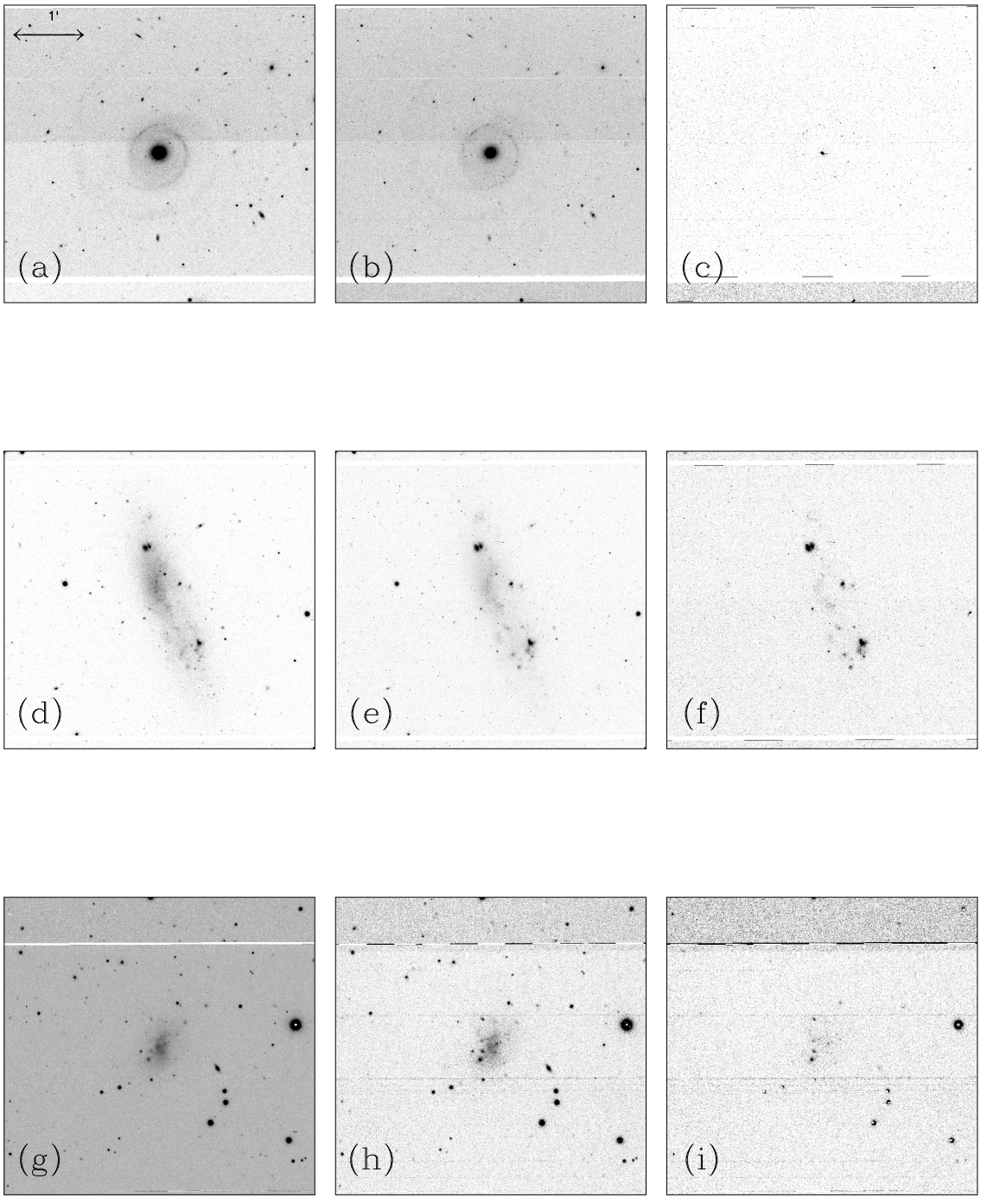

Figure 3.10: Hα images of UGC 6614, UGC 8837, and UGC 9992. North is up and East is left. Intensity levels are adjusted arbitrarily in order to show the galaxy best. The bar on the upper left corner in (a) frame shows $1'$.
Images are in the same order as Fig. 3.6
(a) UGC 6614 continuum (b) UGC 6614 Hα (c) UGC 6614 Hα after continuum subtraction (d) UGC 8837 continuum (e) UGC 8837 Hα (f) UGC 8837 Hα after continuum subtraction (g) UGC 9992 continuum (h) UGC 9992 Hα (i) UGC 9992 Hα after continuum subtraction.

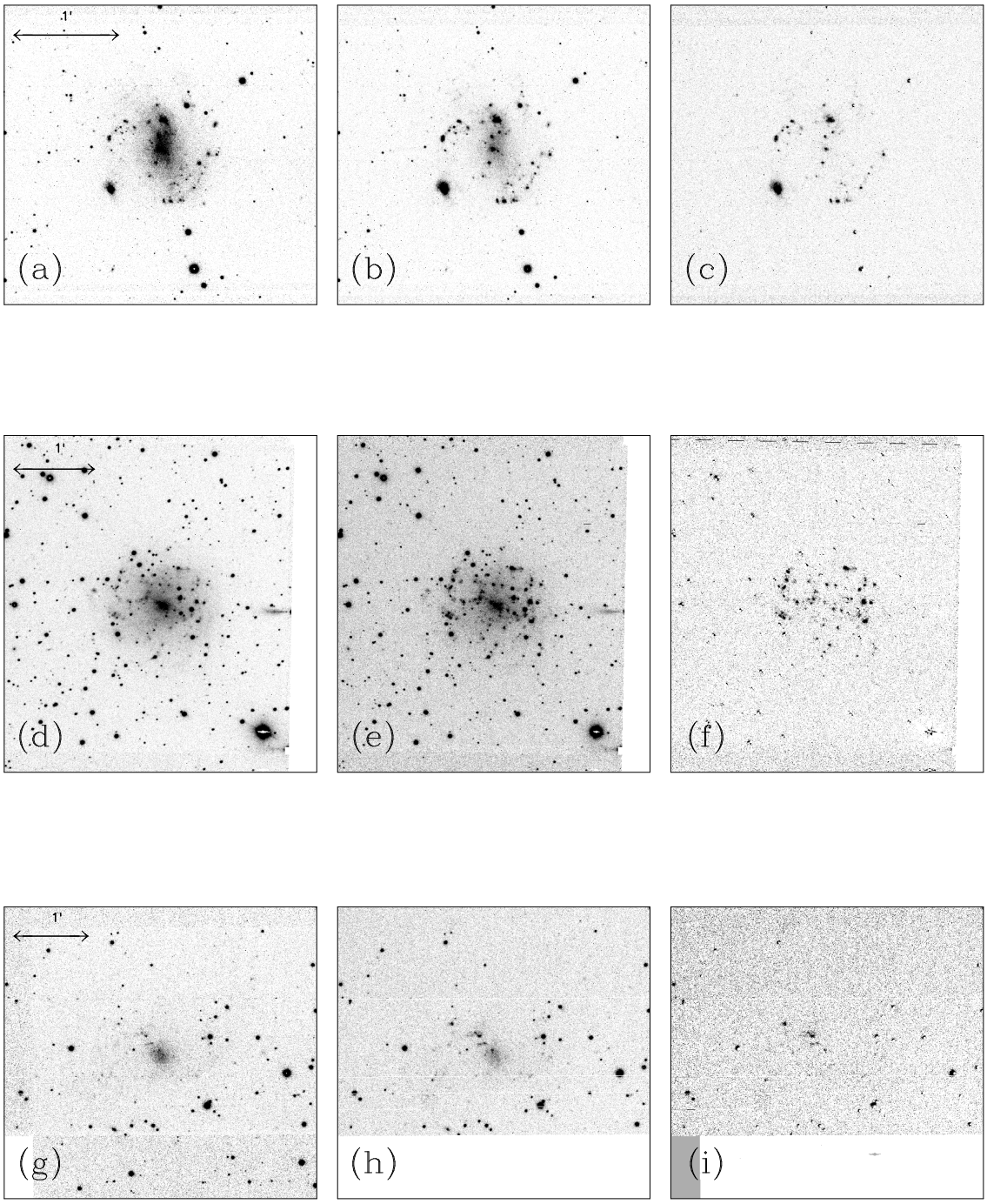

Figure 3.11: Hα images of UGC 10310, UGC 11557, and UGC 11820. North is up and East is left. Intensity levels are adjusted arbitrarily in order to show the galaxy best. The bars on the upper left corners of left column frames show 1$'$. Images are in the same order as Fig. 3.6
(a) UGC 10310 continuum (b) UGC 10310 Hα (c) UGC 10310 Hα after continuum subtraction. (d) UGC 11557 continuum (e) UGC 11557 Hα (f) UGC 11557 Hα after continuum subtraction (g) UGC 11820 continuum (h) UGC 11820 Hα (i) UGC 11820 Hα after continuum subtraction.

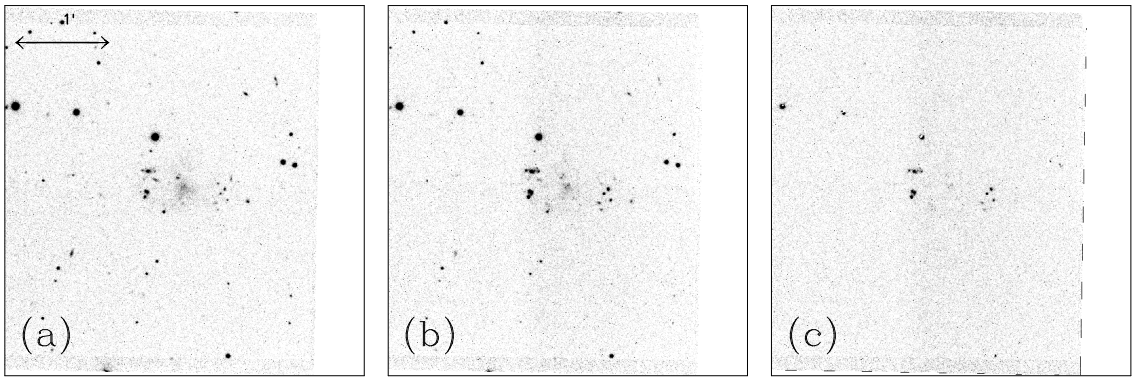

Figure 3.12: Hα images of UGC 12695. North is up and East is left. Intensity levels are adjusted arbitrarily in order to show the galaxy best. The bar on the upper left corners of (a) frame shows $1'$.
(a) UGC 12695 continuum (b) UGC 12695 Hα (c) UGC 12695 Hα after continuum subtraction.

Chapter 4

Gas, Stars and the Evolution of Low Surface Brightness Galaxies

4.1 Introduction

Gas and stars are two major components of galaxies which show the evolutionary paths of galaxies. In particular, the gas mass fraction, f_g, which represents balance between gaseous and stellar components is the primary parameter to quantify the evolutionary state of a galaxy.

Historically, low surface brightness galaxies (LSBGs) have been known to be gas-rich, albeit only with neutral hydrogen (de Blok et al. 1996; van der Hulst et al. 1993a). The general consensus on these objects is that they have had very low star formation rates (SFRs) in the past and still remain so. In Chapter 3, we showed that generally LSBGs have low star formation rates although some relatively red LSBGs have higher than other LSBGs. McGaugh & de Blok (1997) confirmed that LSBGs are rich in gas compared to their stellar mass and have the potential to become very bright systems if certain process ignites their star formation efficiency. They also

found that there is a strong correlation between a galaxy's gas supply and its stellar density, such that galaxies which have lower surface brightness tend to have larger M_{HI}/L and f_g ratios (McGaugh & de Blok 1997).

Understanding the distribution of galaxy luminosity and stellar masses is also very important with respect to studying impacts of gaseous and stellar components of a galaxy on its evolution. As pointed out by McGaugh & de Blok (1997), stellar mass-to-light (M/L), which is estimated by population synthesis models, have big uncertainties and depends on many factors, such as the initial mass function (IMF), metallicity, gas-recycling, and star formation history. Bell & de Jong (2001) claim that near-infrared (NIR) luminosities are better probes as the stellar M/L ratios vary only by a factor of 2 or less across a wide range of star formation histories. Based on this result, Bell et al. (2003) provide formulas to calculate stellar M/L ratios as functions of color.

In this chapter, we investigate correlations between the gas mass fraction of LSBGs and evolutionary parameters of them. In particular, we want to study if the gas mass fraction has any impact on star forming efficiency of LSBGs and its change over the Hubble time. In section 4.2, we discuss our methodology to calculate stellar component masses of our sample galaxies and gas mass fractions consequently. In particular, we explain formulas to calculate stellar M/L ratios in detail. In section 4.3, we explain our parameters which we adopt to investigate star formation histories (SFHs) of LSBGs and discuss correlations between them. In section 4.4, we summarize.

4.2 Stellar and Gaseous Components of LSBGs

4.2.1 Stellar Mass of LSBGs

Stellar Mass to Light Ratio

Bell et al. (2003) formulates relationships between broadband luminosities and stellar mass-to-light (M/L) ratios depending on broadband colors of galaxies. They used a large sample of galaxies from the Two Micron All Sky Survey (2MASS; Skrutskie et al. 1997) and the Sloan Digital Sky Survey (SDSS; York et al. 2000) to estimate present-day stellar mass-to-light ratios, as well as corrections for galaxy evolution and passband shifting between classical Johnson broadband filters and SDSS *ugriz* filters.

Realizing that the main source of uncertainty in stellar M/L ratios is the stellar IMF, Bell et al. (2003) claim that the traditional Salpeter IMR is too rich in low mass stars, resulting in higher mass-to-light (M/L) ratio at a given color. Therefore, they used the "diet" Salpeter IMF, which is devised to satisfy a "maximum-disk" constraint by Bell & de Jong (2001). This is based on the assumption that all disks are maximal. However, Bottema (1993, 1997, 1999) argued that generally disks are not maximal, but rather submaximal. In particular, slow rotating galaxies are substantially submaximal. Therefore, using formulae based on the "diet" Salpeter IMF may not be appropriate.

Hence, we decide to adapt both formulae based on the "diet" Salpeter IMF, Kennicutt IMF (Kennicutt 1983) (hereafter, K83) and Kroupa IMF (Kroupa et al. 1993) (hereafter, KTG93) and compare them, while using Table 7 of Bell et al. (2003) to calculate stellar masses from luminosities of our sample galaxies.

Bell et al. (2003) provides stellar M/L ratios as a function of color. For a Salpeter

IMF,

$$log_{10}(M/L_K) = -0.206 + (0.135 \times (B-V)) \quad (4.1)$$

$$log_{10}(M/L_K) = -0.264 + (0.138 \times (B-R)) \quad (4.2)$$

$$log_{10}(M/L_B) = -0.942 + (1.737 \times (B-V)), \quad (4.3)$$

where the M/L ratio is given in solar units, and luminosities are in Vega magnitudes, instead of in AB magnitudes. For a K83 IMF, or KGT93 IMF, 0.15 dex should be subtracted from the above zero points.

Mainly, we have K_s-band magnitudes available for our galaxies, therefore we convert this K_s-band luminosity into stellar mass. However, for galaxies without K_s-band photometry, we use either our optical broadband photometry results, mainly B-band magnitude, or available photometry information from literature.

We include photometry data which we use in Table. 4.1. Detail information about photometry results are listed in Table. 2.4.

Stellar Mass

Results of calculated stellar mass are given in Table. 4.1. For our sample galaxies, stellar mass has very strong relationships with various parameters from K_s-band data. As given in Table 7 from Bell et al. (2003), M/L ratio in K_s-band is the least sensitive to color variation (the color dependence term is 0.135 as opposed to 1.737 in B-band). K_s-band structure parameters show strong relationships with stellar mass (Fig.4.1 (a) and (b)). Although it is natural to see a strong correlation between disk scale length and stellar mass, since our sample is basically surface brightness limited, a relation between central surface brightness and stellar mass is stronger than one between disk scale length and stellar mass.

Sample galaxies do not show strong relationships between central surface brightness and stellar mass in the other bands. Considering that there is a weak correlation

between central surface brightness and disk scale length, it is strongly noticeable how the K_s-band luminosity depends strongly on its central surface brightness, leading to conclusion that stellar mass of LSBGs depending on the K_s-band central surface brightness.

However, it is likely that central surface brightness is not a cause, but an effect. Although there is a fairly strong relationship between central surface brightness and gas mass fraction (Fig.4.3 (d)), it is weaker than the one between surface brightness and stellar mass. Also Galaz et al. (2002) argues that they do not see a strong relation between them, albeit within the J-band. Colors do not have strong relations with stellar mass, either (Fig.4.1 (c) and (d)).

4.2.2 Gas Mass Fraction

The baryonic gas mass fraction is

$$f_g = \frac{M_g}{M_g + M_*}, \tag{4.4}$$

where M_g is the total mass in the form of gas, and M_* is the total mass in the form of stars. We measure M_* from K_s-band data, and therefore need M_g. To have M_g, we need to know the amount of gas represented by neutral hydrogen ($M_g = \eta M_{HI}$). η should be corrected for both the hydrogen mass fraction X and the phase of gas other than atomic hydrogen.

Following McGaugh & de Blok (1997); Schombert et al. (2001), we adapt a solar hydrogen mass fraction, giving $\eta = X_\odot^{-1} = 1.4$. Generally, this is due to primordial helium and does not vary more than 10% due to variation in helium and metal content. Ionized gas in HII regions and hotter plasma is of negligible mass in spiral galaxies. Moreover, there has been no detectable CO emission in LSBGs, except some large, red ones (Das et al. 2006; Schombert et al. 1990): the total gas mass

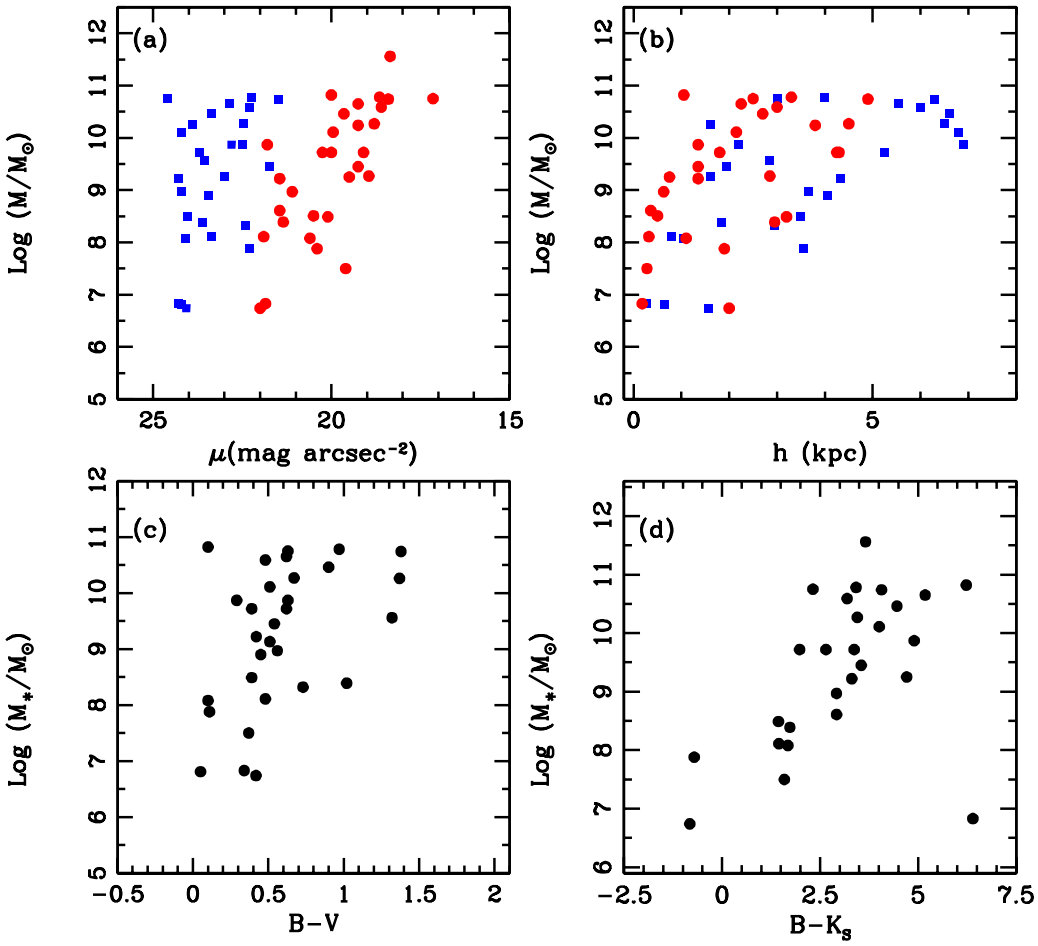

Figure 4.1: Dependence of stellar mass on structural parameters and colors. For upper panels, blue squares represent B-band parameters and red circles represent K_s-band paramters (a) central surface brightness versus stellar mass (b) disk scale length versus stellar mass (c) B-V versus stellar mass (d) B-K_s versus stellar mass.

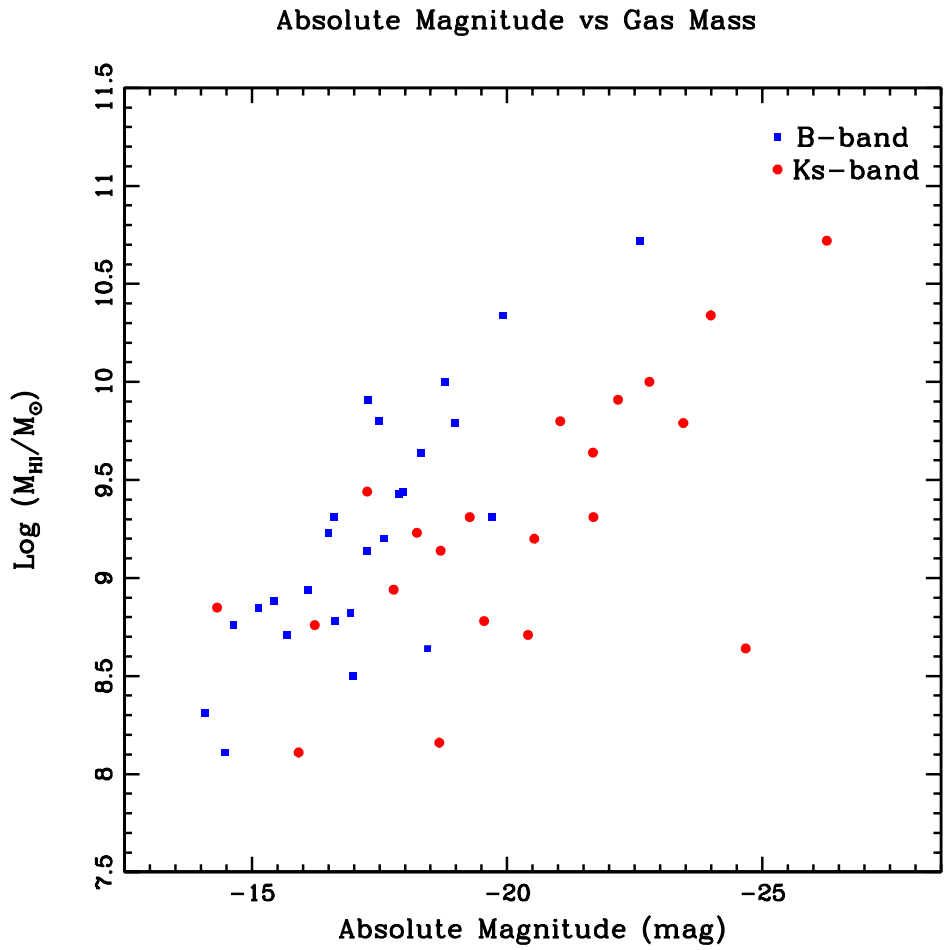

Figure 4.2: Absolute magnitude versus gas mass. Blue squares represent B-band luminosity and red circles represent K_s-band luminosity. Gas mass is HI only.

in the molecular phase appears to be a small fraction of that in the atomic phase in these galaxies. We obtained neutral hydrogen masses from various literature sources. We list them in Table 4.1. There are relatively strong relations between luminosity and gas mass (Fig.4.2). This simply shows that generally galaxies with high gas mass are good reservoirs for star formation, regardless of their star forming efficiency.

4.2.3 The Relations between Properties

The gas mass fractions calculated as described above are listed in Table. 4.1 as well as other inputs and stellar components. The gas mass fraction shows strong relationships with luminosity, stellar mass, and central surface brightness, although only K_s-band has an evident correlation with central surface brightness (Fig.4.4,4.3). It is relatively obvious that those parameters have strong relations with the gas mass fraction.

While luminosity represents stellar mass depending on colors, the gas mass fraction represents how efficiently a galaxy turns gas into stars. Therefore, a galaxy with higher star forming efficiency should have generally higher stellar mass and higher luminosity. Since LSBGs have a range of exponential disk scale lengths, galaxies with high star forming efficiency have higher disk surface brightness on average.

Colors display rather interesting relationships with gas mass fraction (Figs.4.4 (c) and (d)). As shown by Bell & de Jong (2000), optical colors represent exponential folding time of SFH, while combined colors of optical and NIR bands represent metallicity. In both B-V and B-Ks colors, bluer galaxies have higher gas mass fraction.

On the other hand, bluer galaxies in B-Ks band are low metallicity galaxies. The simplest interpretation is that a galaxy which turns its gaseous component into stars tends to have high metallicity, while a galaxy which is slow to turn its gas into stars tends to have low metallicity. This seems natural enough, as gas fraction should be directly related to metallicity in closed box chemical evolution models: high metallicity occurs, after the gas is mostly consumed. Correlation coefficients of gas mass fraction with other parameters are listed in Table 4.3.

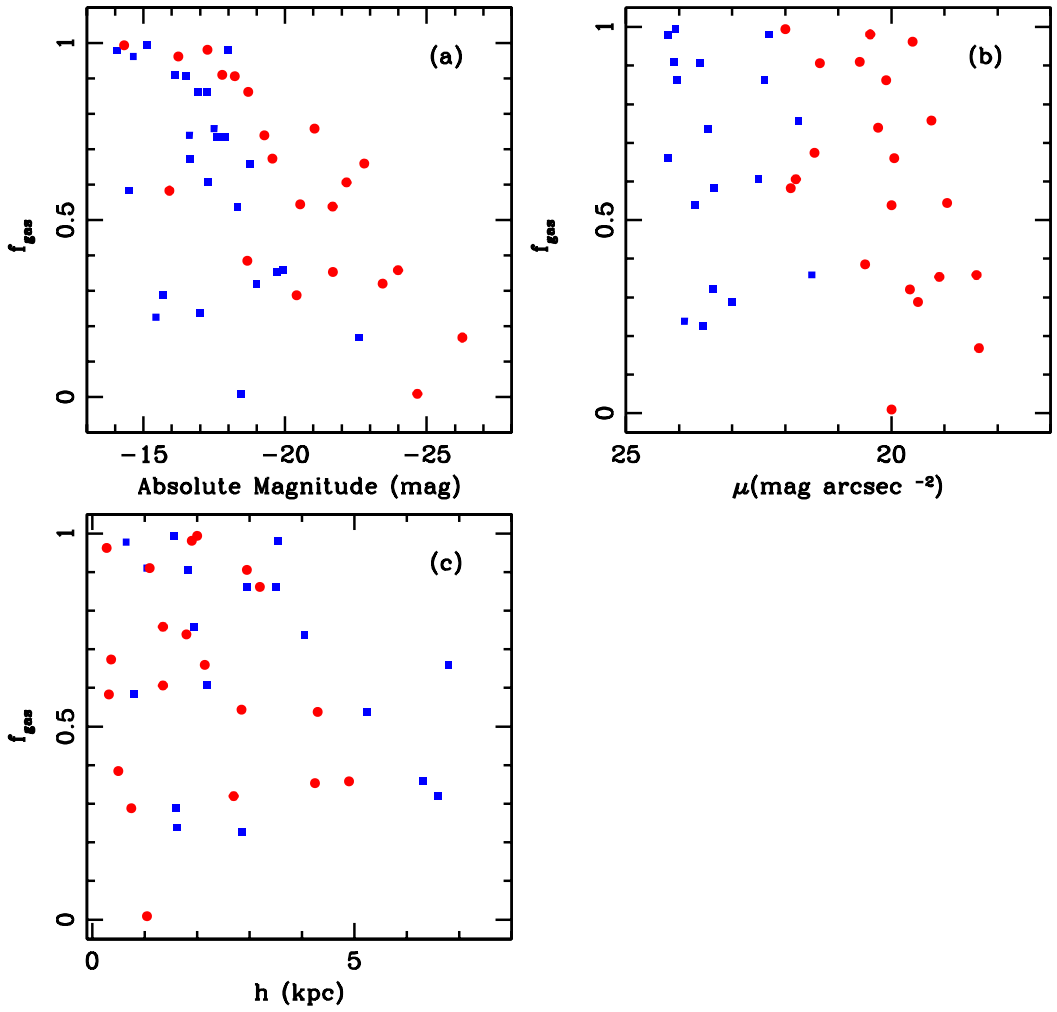

Figure 4.3: Correlations between gas mass fraction and other parameters. Like previous figures in this chapter, blue squares represent B-band parameters and red circles represent K_s-band parameters. (a) Total magnitude versus gas mass fraction (b) central surface brightness versus gas mass fraction (c) disk scale length versus gas mass fraction.

Table 4.1. Stellar and Gaseous Components of Sample Galaxies

Galaxy	Color	M_T (mag)	log ($M_*/M_\odot$) Salpeter†	Log($M_{HI}/M_\odot$)§	f_g Salpeter†	References
512-2	0.6[a]	-18.67	8.66	8.16	0.385	2
D575-2	0.42[b]	-14.32	6.89	8.85	0.994	2
D584-2	0.10	-17.78	8.23	8.94	0.910	2
D646-5	0.05	-14.08[c]	6.96	8.31	0.978	2
D721-5	1.02	-18.23	8.54	9.23	0.906	2
F561-1	0.45	-17.59[c]	9.05	9.20	0.736	4
F563-V1	1.32	-15.44[c]	9.71	8.88	0.226	2
F563-V2	0.73	-16.93[c]	9.28	9.58	0.798	2
F565-V2	0.53[b]	-15.41[c]	8.32	8.82	0.862	4
F568-1	0.62[b]	-21.68	9.87	9.64	0.538	4
F568-V1	0.51	-17.88[c]	9.28	9.43	0.736	4
F571-8	0.7[a]	-20.53	9.42	9.20	0.544	4
F577-V1	0.11	-17.26	8.03	9.44	0.981	4
F611-1	1.37	-16.99[c]	10.416	8.50	0.238	5
F730-V1	0.63	-19.22[c]	10.02			
NGC 4455	0.1[b]	-24.67	11.002	8.64	0.009	3
UGC 128	0.51[b]	-22.70	10.261	10.0	0.660	7
UGC 334	0.90[b]	-23.45	10.616	9.79	0.320	8
UGC 628	0.62[b]	-24.01	10.805			
UGC 731	0.34[b]	-19.55	8.76	8.78	0.674	3
UGC 1230	0.54	-21.04	9.60	9.45	0.758	8
UGC 2259*	1.32[d]	-20.41	9.40	8.71	>0.288	6
UGC 2885*	0.7[ab]	-26.26	11.716	10.72	>0.168	6
UGC 3371	0.56[b]	-19.84	9.12			
UGC 6614	1.38	-23.99	10.894	10.34	0.358	8
UGC 8837	0.43[b]	-15.92	8.26	8.11	0.512	3
UGC 9992	0.37[b]	-16.23	7.65	8.76	0.855	3
UGC 10310	0.39[b]	-19.27	8.87	9.01	0.739	3
UGC 11454	0.97	-24.22	10.938			
UGC 11557	0.6[a]	-21.69	9.87	9.31	0.353	3
UGC 11583	0.34	-14.553	6.98			
UGC 11616	0.48	-23.92	10.749			
UGC 11648	0.7[a]	-22.95	10.394			
UGC 11748	0.63	-24.25	10.905			
UGC 11819	0.67	-23.06	10.427			
UGC 11820	0.39[b]	-18.70	8.49	9.14	0.862	1
UGC 11944	0.42[b]	-20.50	9.22			
UGC 12695	0.29	-22.17	10.02	9.91	0.606	8

Note. — ∗ High Surface Brightness Galaxy † Based on Bell et al. (2000)'s formula for the "diet" Salpter IMF. Subtracting 0.15 dex from these values provide stellar mass based on a Kennicutt or Kroupa IMF based on Bell et al. (2000).

[a] No color available. Picked up from comparison with other colors to median sample values. [b] From literature. Refer to Table.2.4 for references. [c] Calculated using B-band luminosity instead of K_s-band luminosity.

‡ Based on Portinari et al. (2004)'s formula for a Kroup IMF.

§ Neutral hydrogen masses are from literatures. References are indicated in Column (9).

References 1. van Zee et al. (1997b) 2. Pildis et al. (1997) 3. Swaters et al. (2002) 4. de Blok et al. (1996) 5. Eder & Schombert (2000) 6. de Blok & McGaugh (1997) 7. McGaugh (2005) 8.McGaugh & de Blok (1997)

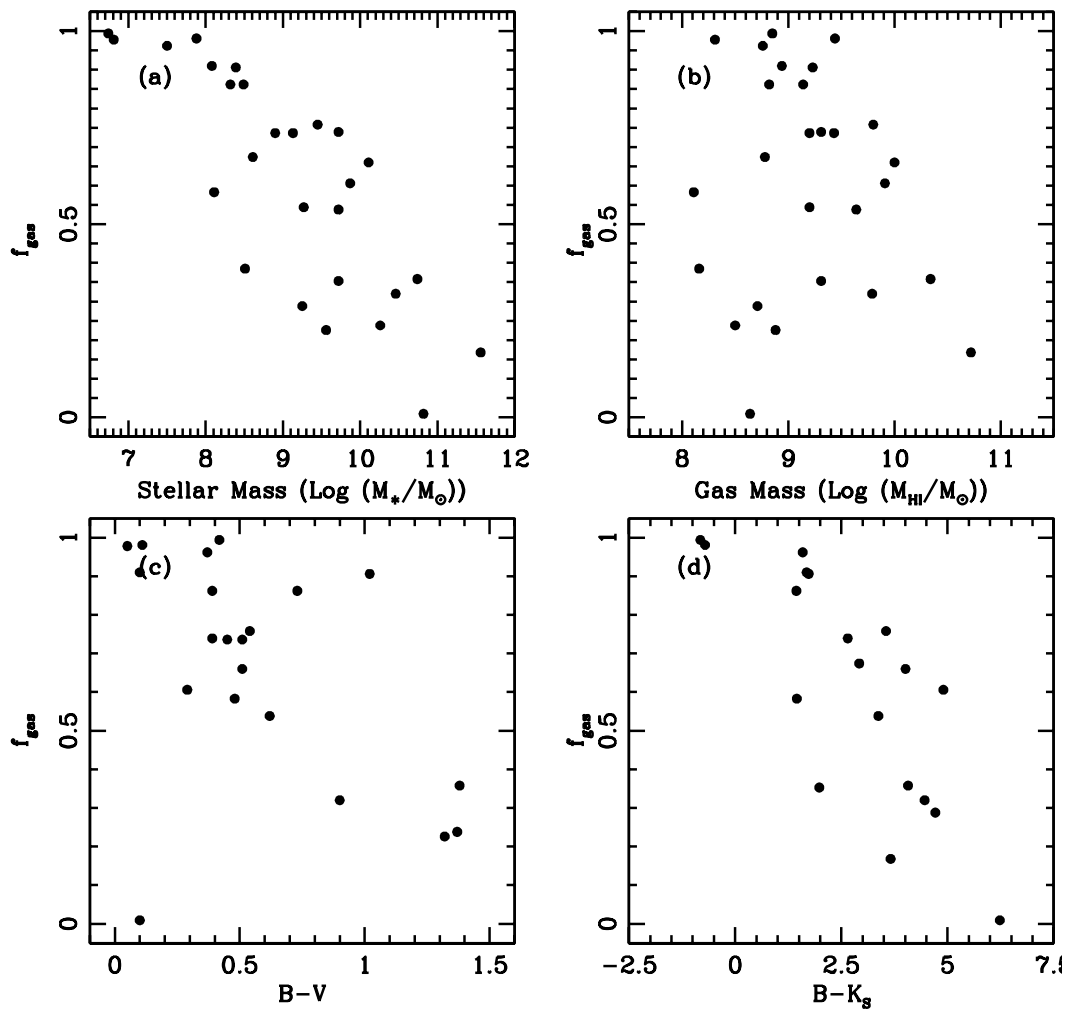

Figure 4.4: Correlations between gas mass fraction and mass components and colors. (a) Gas mass versus gas mass fraction (b) stellar mass versus gas mass fraction (c) B-V versus gas mass fraction (d) B-K_s versus gas mass fraction.

4.3 Star Formation Histories

4.3.1 Star Formation Rates

Since we adopt both M/L ratio formula for a Salpeter IMF and K83/KTG93 IMFs, we calculate star formation rates (SFRs) of our sample galaxies using conversion factors for both IMFs as well.

As mentioned in Section.3.3.2, the star formation rate is given by

$$SFR(M_{\odot}) = 7.937 \times 10^{-42} L(H\alpha), \quad (4.5)$$

for a Salpeter IMF. Then for a K83 IMF and a KTG93 IMF, it is

$$SFR(M_{\odot}) = 7.352 \times 10^{-42} L(H\alpha), \quad (4.6)$$

$$SFR(M_{\odot}) = 1.786 \times 10^{-41} L(H\alpha), \quad (4.7)$$

respectively.

Star formation rates from 19 sample galaxies do not show any strong correlation with luminosity, or other structure parameters, such as central surface brightness and disk scale length (Fig.4.6). The current SFR appears to be just that which happens to be occurring now, without regard to the global properties of the host galaxy.

4.3.2 Average Past Star Formation Rates

The average past star formation rate is derived by estimating the total stellar mass which are formed over life time of a galaxy. It can be given by a simple formula as

$$< SFR >_{past} = M_*/T_{sf}. \quad (4.8)$$

While we have well-measured stellar mass information for our sample through K_s-band photometry, the length of star formation time, T_{sf}, is relatively unconstrained, although it must not exceed the age of the universe.

Essentially all galaxies for which the necessary data can be obtained display at least some very old stars. This is consistent with the notion that galaxies formed shortly after the Big Bang. We therefore simply adopt 10 Gyr of T_{sf} for our estimation of the average star formation rate. Various inputs and results are given in Table. 4.2.

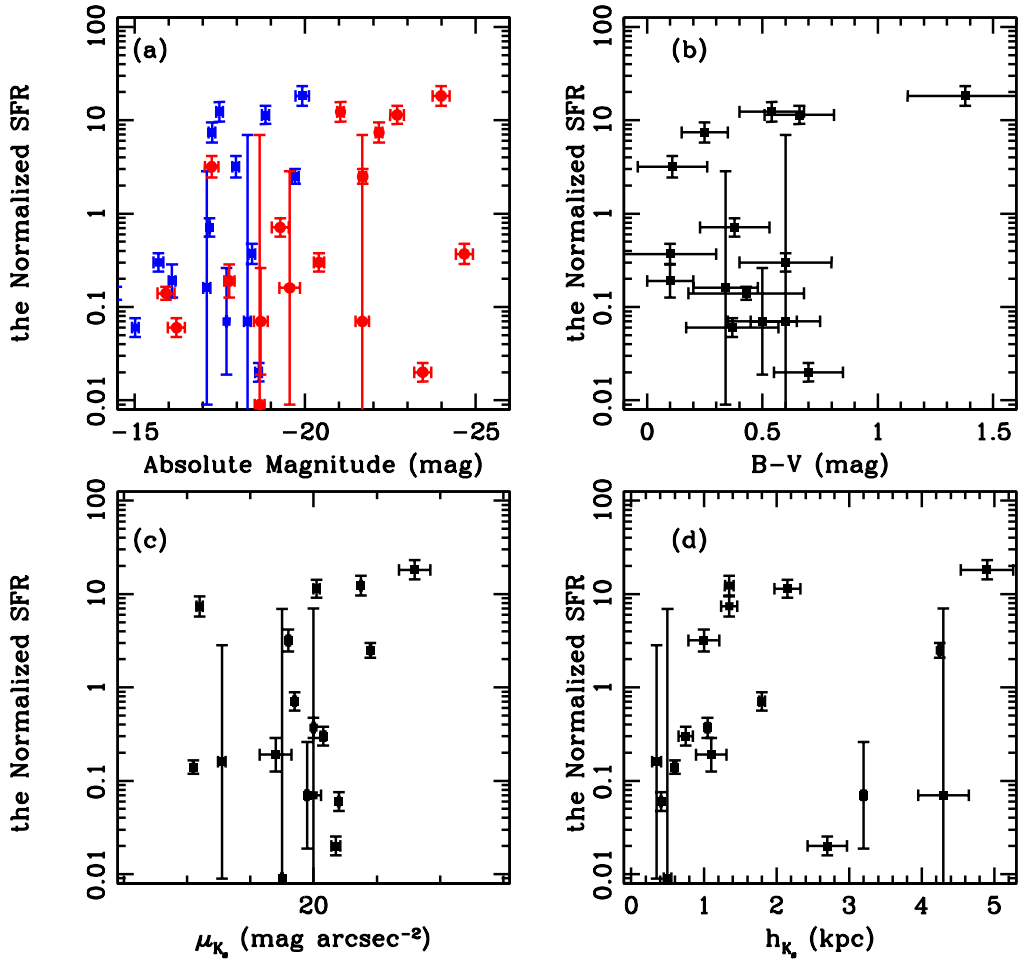

Figure 4.5: Correlation between the normalized star formation rate and other properties. The normalized star formation is the ratio of current star formation rate to average star formation rate. Average star formation rates are calculated by dividing stellar masses by 10 Gyr.
(a) Absolute magnitude versus the normalized star formation rate (b) B-V color versus the normalized star formation rate (c) B-band central surface brightness versus the normalized star formation rate (d) K_s-band central surface brightness versus the normalized star formation rate.

Although $<SFR>_{past}$ does not cover a wide range of parameter space, it does not show any strong trend either. However, the normalized SFR which is a ratio of current SFR to $<SFR>_{past}$ does show an interesting trend. First, our sample galaxies have generally higher current SFRs than $<SFR>_{past}$. Those galaxies which have lower current SFRs do not have anything in common except their relatively low gas mass fraction. The gas mass fraction has a strong relation with the normalized SFR (Fig.4.6 (a)), while stellar and gas mass do not show any trend with the normalized SFR (Figs.4.6 (c) and (d)). Moreover total baryonic mass does not have any correlation with the normalized SFR (Fig.4.6 (b)). This is quite interesting since gas mass fraction shows quite a strong correlation with luminosity and stellar mass (Figs.4.3 (a) 4.4 (a)).

Considering a relatively weaker correlation between gas mass fraction and gas mass (Fig.4.4 (b)), this shows that a galaxy which has not formed a large amount of stars out of its gas component, tends to be star-forming at the current epoch.

Another parameter which has a strong correlation with the normalized SFR is K_s-band central surface brightness, while other optical broad-bands do not show any strong correlation with it by their central surface brightness (Fig.4.7 (a) and (b)). As the K_s-band central surface brightness becomes brighter, the normalized SFR becomes smaller. This shows that galaxies with increased star forming activity have fewer old stellar populations formed so far.

It is worth noting that these correlations match well the conclusions of Bell et al. (2000). Comparing their sample colors to model grids, they concluded that the age of an LSBG stellar population is correlated with its surface density. Based on our tight relation between K_s-band luminosity, i.e. stellar mass, and its surface brightness, LSBGs with low K_s-band surface brightnesses should have increased current SFRs. Therefore, at least their mean age of stellar population should be

younger than those galaxies with high K_s-band surface brightness.

Fig.4.8 shows that colors may have the expected trends with scatter. One outlier from Fig. 4.8 (a) is UGC 6614 which is a huge "Malin"-type galaxy. While another big LSBG, F568-1 does not have an increased current SFR, UGC 6614 shows a star-forming ring around its nuclear region (Fig.3.10 (c)). On the other hand, an outlier in the opposite direction is actually NGC 4455 which is a HSBG. F577-v1, which has $B - Ks$ of -0.71, was barely detected in the K_s-band and its K_s-band luminosity may not be meaningful. Correlation coefficients from these analyses are given in Table 4.3.

4.3.3 Stellar Component Build-up Timescale

In order to estimate changes of SFHs of our sample galaxies, we calculate how long it would take for them to build up their stellar mass components with their current SFRs. We simply divide their stellar masses by their SFRs:

$$\tau_* \quad = \quad M_*/SFR. \tag{4.9}$$

The average stellar component build-up timescale is 4.5 Gyr. However, there are four galaxies whose build-up timescales are longer than the Hubble time, one of which is NGC 4455, a normal galaxy. Clearly, this means that their SFRs have decreased. Without these four galaxies, the average timescale is 1.6 Gyr which is quite short compared to the Hubble time.

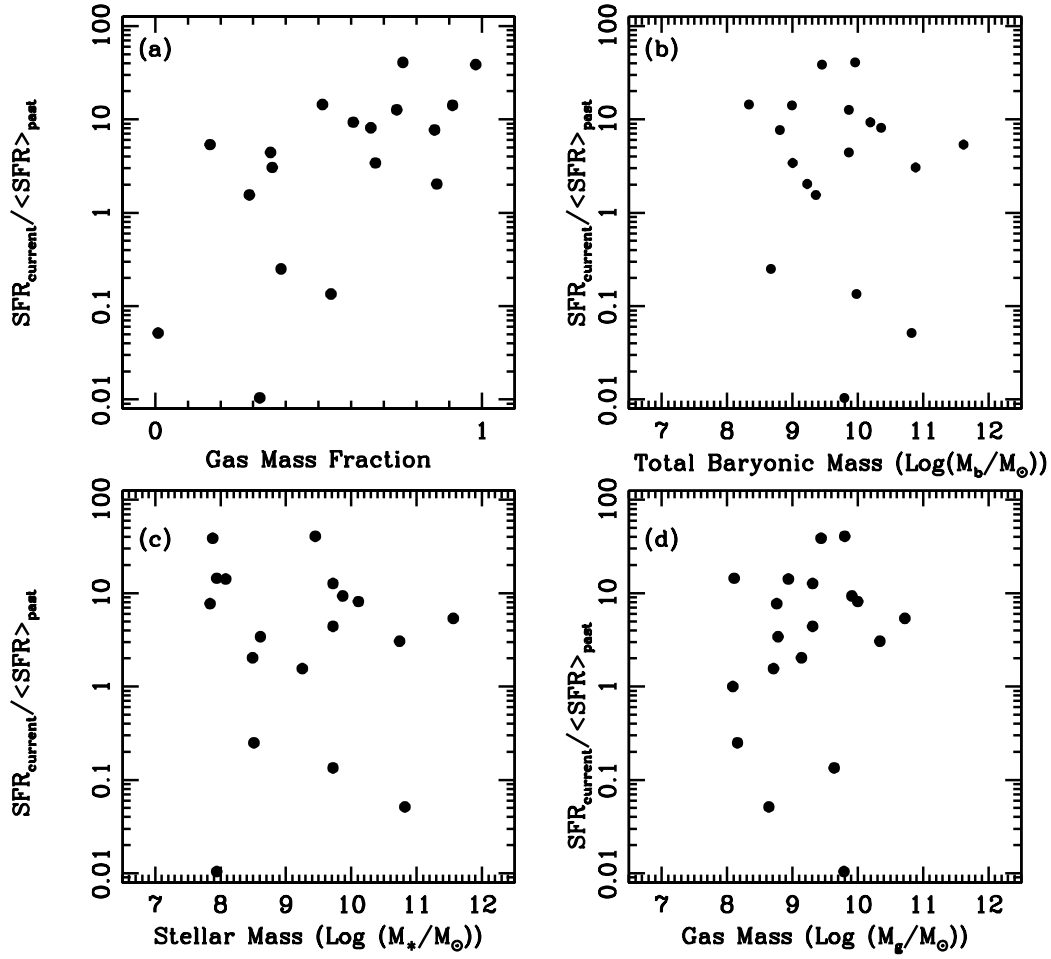

Figure 4.6: Correlation between the normalized star formation rate and mass components. The normalized star formation is the ratio of current star formation rate to average star formation rate. Average star formation rates are calculated by dividing stellar masses by 10 Gyr.
(a) Gas mass fraction versus the normalized star formation rate The dashed line represent the least-square fit for two parameters, $Log(SFR_{current}/ < SFR >_{past}) = 2.24 \times f_g - 0.823$. (b) total baryonic mass versus the normalized star formation rate (c) stellar mass versus the normalized star formation rate (d) gas mass versus the normalized star formation rate.

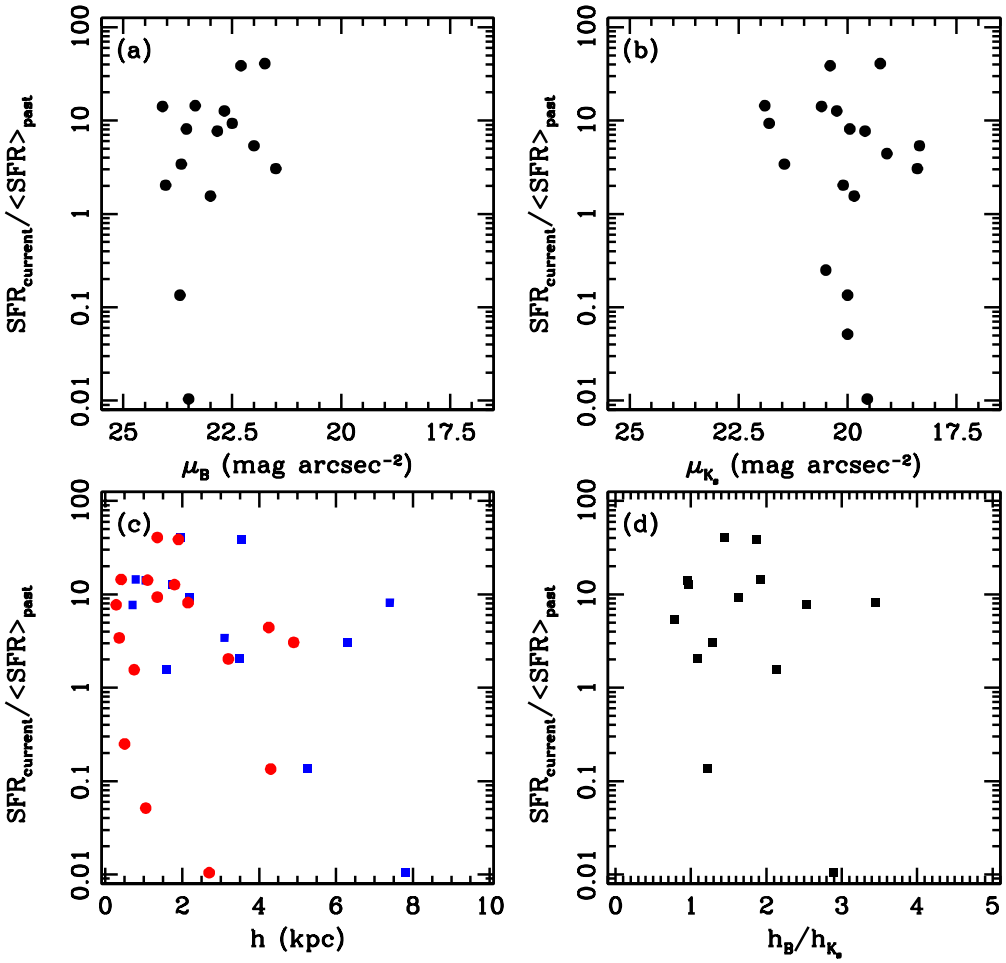

Figure 4.7: Correlation between the normalized star formation rate and structural parameters. See Fig.4.6 for a definition of the normalized star foramtion rate.
(a) B-band central surface brightness versus the normalized star formation rate
(b) K_s-band central surface brightness versus the normalized star formation rate
(a) and (b) are plotted in the same x-axis span for easy eye comparison.
(c) disk scale length versus the normalized star formation rate. Blue squares represent B-band disk scale length and red circles represent K_s-band disk scale length. (d) ratio between B-band central surface brightness and K_s-band central surface brightness versus the normalized star formation rate.

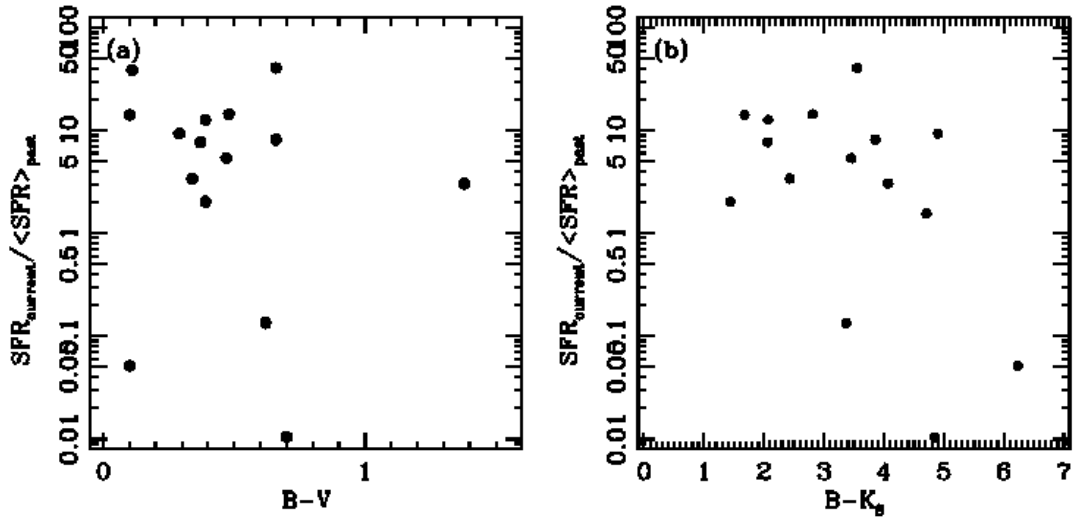

Figure 4.8: Correlation between the normalized star formation rate and colors. See Fig.4.6 for a definition of the normalized star foramtion rate. (a) B-V versus the normalized star formation rate (b) B-K$_s$ versus the normalized star formation rate.

4.3.4 Gas Depletion Timescales

Whether a galaxy can continue to sustain their current SFRs for several gigayears or not is interesting to see. The gas depletion timescale is calculated from current SFR and the neutral hydrogen mass:

$$\tau_g \;=\; \eta M_{HI}/SFR. \tag{4.10}$$

The average gas depletion timescale is also 4.5 Gyr for our sample galaxies. Five of the sample galaxies have gas depletion timescales shorter than 1 Gyr. UGC 2885, a galaxy with a huge current SFR, is one of them. For those galaxies with large amounts of gas components, it is easy to simply consider them with increasing SFRs over the Hubble time. However, three of those five galaxies have longer τ_* than their

gas depletion timescales, which simply means that their stellar components are more than their gas components.

For those four galaxies with τ_* longer than the Hubble time, they have very long gas depletion timescales as well, except NGC 4455. For example, UGC 334 whose τ_* is longer than 2000 Gyr has its gas depletion timescale of $\sim$ 200 Gyr with more than $4{\times}10^9 M_\odot$ gas available.

It must also be noted that this gas depletion time scale assumes that a galaxy can consume all of the available gas turning it into stars. The distribution of neutral hydrogen generally extends well beyond its optical counterpart. It is unknown if galaxies can convert their extended neutral hydrogen into stellar component. On the one hand, a gradual extension of the stellar disk into the larger HI disk seems consistent with the idea that disks grow inside-out. On the other, it is not clear whether the low column densities of HI at larger radii will ever be able to sustain star formation. The availability of this reservoir for star formation thus remains in doubt.

4.4 Discussion

We have discussed stellar and gaseous components of LSBGs regarding their evolution through star formation. In this chapter, we will discuss the SFHs of LSBGs and their impact on physical properties of LSBGs.

In Section 2.5, we discussed colors of LSBGs and possible impacts of SFH on them. Simply we ruled out the initial burst scenario and the declining SFR scenario due to their broad-band colors, especially $U-B$ and $B-V$. It is difficult to conclude on when these galaxies have formed only based on their colors. Rather, it is plausible that some of LSBGs have formed at fairly recent epochs. However,

Table 4.2. Star Formation Rates and Evolutionary Time Scales of Sample Galaxies

Galaxy	log ($M_*/M_\odot$)		$<SFR>_{past}$	SFR ($M_\odot$ yr^{-1})		Log τ_*	Log (M_{HI}	Log τ_g
	Salpeter	K83/KTG94	($M_\odot$ yr^{-1})	Sal	K83	(yr)	$/M_\odot$)	(yr)
D512-2	8.66	8.51	0.032	0.009±0.026	0.008	10.66	8.16	10.31
D570-4	8.02	7.87	0.007	0.008±0.001	0.007	9.97	8.09	11.19
D575-2	6.89	6.74	0.0006				8.85	
D584-2	8.23	8.08	0.012	0.19±0.034	0.17	8.80	8.94	9.66
D646-5	6.96	6.81	0.0007				8.31	
D721-5	8.54	8.39	0.025				9.23	
F561-1	9.05	8.90	0.079				9.20	
F563-V1	9.71	9.56	0.36				8.88	
F563-V2	9.28	9.13	0.13				9.58	
F565-V2	8.32	8.17	0.18				8.82	
F568-1	9.87	9.72	0.52	0.074±0.14	0.07	11.0	9.64	10.64
F568-V1	9.28	9.13	0.135				9.43	
F571-8	9.42	9.27	0.19				9.20	
F577-V1	8.03	7.88	0.076	3.18±0.37	2.94	7.53	9.44	8.89
F611-1	10.41	10.26	1.82				8.50	
F730-V1	10.02	9.87	0.74					
NGC 4455†	11.00	10.82	6.61	0.37±0.04	0.34	11.43	8.64	9.30
UGC 128	10.26	10.11	1.29	11.4±1.1	10.5	9.21	10.0	8.98
UGC 334	10.61	10.46	2.88	0.02±0.002	0.03	12.31	9.79	11.31
UGC 628	10.80	10.65	4.47					
UGC 731	8.76	8.61	0.041	0.16±0.02	0.14	9.56	8.78	9.63
UGC 1230	9.60	9.45	0.28	12.3±1.3	11.4	8.51	9.80	8.74
UGC 2259	9.40	9.25	0.18	0.30±0.03	0.28	9.92	8.71	9.26
UGC 2885†	11.71	11.56	36.3	210.4±21.1	194.9	9.39	10.72	8.43
UGC 3371	9.12	8.97	0.093					
UGC 6614	10.89	10.74	5.50	18.15±1.90	16.81	9.63	10.34	9.73
UGC 8837	8.09	7.94.	0.009	0.14±0.014	0.13	8.94	8.11	9.51
UGC 9992	7.99	7.84	0.007	0.058±0.006	0.054	9.23	8.76	10.28
UGC 10310	8.87	8.72	0.052	0.71±0.07	0.66	8.91	9.01	9.20
UGC 11454	10.93	10.78	6.03				9.31	
UGC 11557	9.87	9.72	0.52	2.5±0.25	2.3	9.47	9.31	8.91
UGC 11583	7.98	7.83	0.0007					
UGC 11616	10.74	10.59	3.89					
UGC 11648	10.39	10.24	1.74					
UGC 11748	10.90	10.75	5.62					
UGC 11819	10.42	10.27	1.86					
UGC 11820	8.64	8.49	0.031	0.07±0.04	0.063	9.79	9.14	10.36
UGC 11944	9.37	9.22	0.17					
UGC 12695	10.02	9.87	0.74	7.4±0.8	6.9	9.15	9.91	9.07

Note. — † High Surface Brightness Galaxy

Table 4.3. Correlation Matrix

	f_g	M_*	M_{gas}	μ_B	μ_{Ks}	h_B	h_{Ks}	B-V	B-K_s
$SFR_{current}/<SFR>_{past}$	0.62	-0.06	0.13	-0.49	0.13	-0.38	-0.55	0.54	0.54
f_g		-0.80	-0.21	-0.17	-0.62	-0.20	-0.4	-0.65	-0.78
M_*			0.61	0.25	0.67	0.49	0.46	0.45	0.49

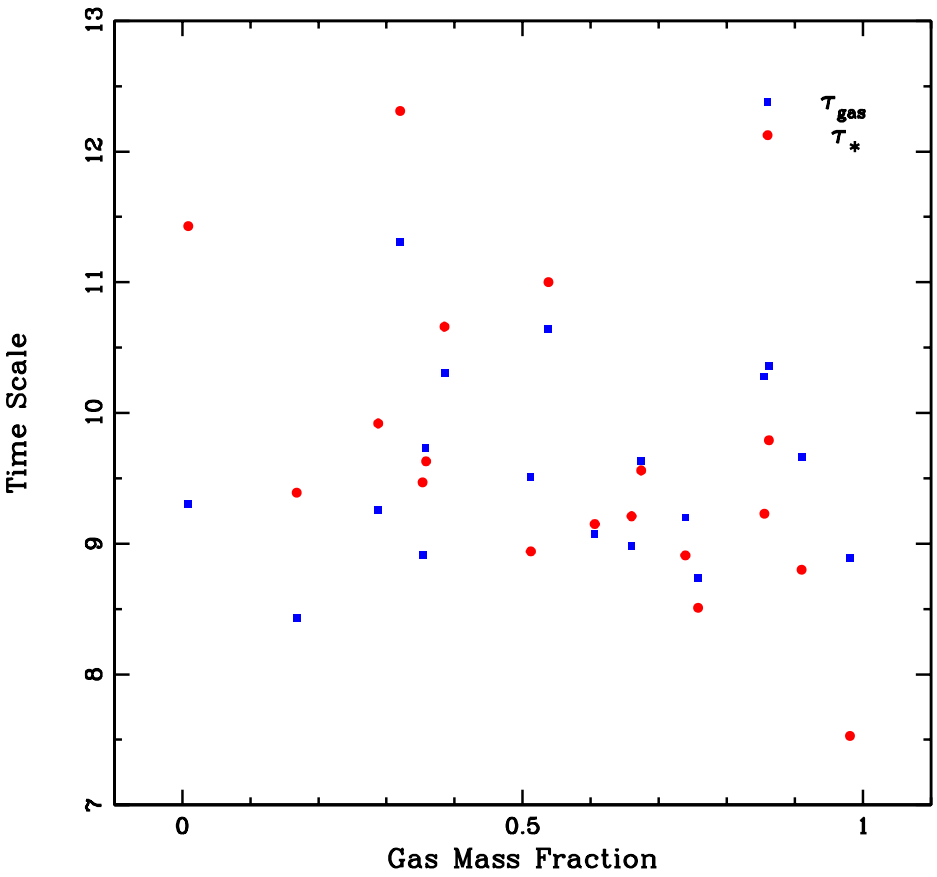

Figure 4.9: Gas mass fraction versus timescale. Filled circles represent gas depletion timescale and filled squares represent stellar component build-up timescale. Notice that there is no strong correlation between gas mass fraction and τ_{gas}.

based on K_s-band luminosity and amounts of their stellar masses, it is difficult to exclude that the star formation epochs of some LSBGs date back to shortly after the Big Bang. Their stellar component build-up timescales are generally several gigayears.

However, it is still not clear whether these galaxies have been gradually increasing their star formation rates, or kept it constant. If the SFR is gradually ramping up to the present, the normalized SFR should have a tight correlation with $B-V$ or

$B-K_s$ colors. As described in section 4.3.2, they show the trends which are required to explain colors. However, scatters are big and the gas depletion timescales range fairly big as the stellar component build-up timescales. Fig.4.9 shows that there is no strong correlation between the gas depletion time and gas mass fraction. If their SFR has been gradually increased over the Hubble time, galaxies which turned more gas into stars should have shorter gas depletion timescales. This is not shown in Fig.4.9.

Therefore, the most plausible scenario to explain properties of LSBGs is perhaps the episodic SFH with sporadic bursts, probably superimposed on either a constant SFH or a slightly increasing SFH. With a big range of current SFRs and normalized SFRs, what we are seeing now can be explained as a snapshot of sporadic SFHs. The question of why LSBGs have these sporadic SFHs is very interesting, particularly after a seemingly long hiatus of massive star formation. As mentioned, it is hard to rule out that LSBGs actually have formed late, or significantly later after the Big Bang. As shown by simulations, primordial halos with large angular momentum collapse late and LSBGs are from these halos. Large angular momentum prevents gas from falling into disks, eventually from turning into stars. If gas somehow still collapses onto stellar disks, it may explain the SFHs of LSBGs.

However, according to the CDM paradigm, smaller galaxies form early and merge into bigger ones. Surely, early formation epochs do not guarantee a large amount of old stellar populations and old mean ages of stellar components. It also involves environmental properties of galaxies to grow through the Hubble time. Still it is clear that most LSBGs are surprisingly young in terms of their stellar populations.

Chapter 5

Summary and Future Work

5.1 Summary

Little is known about the star formation history of low surface brightness galaxies These galaxies are generally blue in the optical and the near-IR. This indicates an undeveloped giant branch, which would be expected with a scenario in which they are relatively unevolved or have delayed SFHs contradicting the initial impression that they may simply be faded remnants of higher surface brightness galaxies whose star formation has finished.

We obtained optical and near-infrared broadband photometry along with Hα photometry of a large sample of low surface brightness galaxies to measure the current and the time-averaged star formation rate in order to answer the following questions:

1. When did LSBGs form? Did they form early as hierarchical galaxy formation models predict, or did they form late?

2. Why do LSBGs have such low star formation efficiencies even with large amounts of gas? Do they have a fundamentally different star formation pro-

cess?

3. What do the SFHs of LSBGs look like? Have they been decreasing, constant, or increasing?

In Chapter 2, we looked into luminosities, colors, and structural parameters of a large sample of LSBGs based on our optical and NIR observation. We presented our observation and data reduction in detail and analysis on their bulge-disk structures. Low surface brightness galaxies have a surprisingly broad range of their physical parameters; luminosity, size, gaseous and stellar mass. Still, they are generally blue in optical and NIR colors, as have been documented and do have young stellar populations. There is not a strong relation between luminosity, colors, and structure parameters and trends across optical and NIR bands. Still, exponential disk scale lengths are shorter in the K_s-band than other optical bands, which can lead into color gradient along disks. Also, galaxies with longer disk scale lengths in the K_s-band are generally redder.

In chapter 3, we presented our observation and the result from Hα photometry of 19 LSBGs. The average Hα luminosity of 19 sample galaxies is 175×10^{40} erg s^{-1}. Although this average is still low, the samples have a surprisingly wide range of SFRs. We have not found any strong trend indicating a possible high SFR for a LSBG, since those galaxies with higher Hα luminosity do not possess lots of common characteristists. We have suggested that LSBGs have episodic SFHs based on the fact that they are generally rich in their gaseous components and blue in colors regardless of their current star forming rates.

We also looked into HII regions luminosity function (LF) in chapter 3 and presented a composite LF from our entire sample. Although this LF has a slope which is similar to that of the LF from other galaxies, it has a relatively higher break for slope and flatter slope below the break. We suggested three possibilities: incom-

pleteness of lower luminous HII regions, blending in due to large distances and a different initial cluster populations for LSBGs.

In chapter 4, we investigated impacts of gas and stellar components on star formation histories of galaxies along with other parameters. First, we showed that current star formation rates of LSBGs are higher than, or comparable to the average past star formation rate. This shows that LSBGs have been slow to form stars and have formed stars continuously, or even with an increasing efficiency.

We showed that gas mass fraction has a tight relation with the normalized star formation rate, while stellar and gas mass do not show any trend with the normalized SFR. Colors do not have have a tight relation, either. K_s-band central surface brightness has strong relationships with other physical characteristics over parameter space as well. In particular, stellar mass and gas mass fraction have tight relationships with it.

We suggested that, combined with bluer colors in optical and NIR wavelengths, these correlations shows that the most plausible SFH scenario is the episodic SFH with sporadic burst. With a big range of SFRs, we possibly look into a snapshot of sporadic SFHs which combine episodic burst either with a constant SFH or a slightly increasing SFH. We also suggested that large angular momentum can explain the LSBGs. It prevents gas from falling into a dense disk, impeding SFR in stars within LSBGs. We suggest that if gas somehow still collapses onto stellar disks, it appears as episodic SFHs of LSBGs.

Based on what we have found through this work, we will try those three questions.

1. It is not obvious when LSBs form. Their populations and gas fractions are consistent with young ages, so relatively recent formation can not be excluded. Neither can one exclude the possibility that they are all ancient, in the sense

of perhaps having at least some ancient stars. However, in many cases, the bulk of the mass in stars seems to have been formed in the more recent half of the Hubble time. If all LSBGs are ancient as nominally expected in LCDM models, then we must appeal to internal evolutionary processes to delay the conversion of gas into stars.

2. There is no clear evidence that the star formation process in LSBGs differs fundamentally from that in other galaxies. Their inefficient conversion of gas into stars seems to stem from the diffuse distribution of gas, which in turn may arise from their high specific angular momenta. This much, at least, is consistent with the notion common to many LCDM galaxy formation scenarios in which LSBGs form in high spin dark matter halos.

3. LSBGs seem to have experienced a variety of SFHs as diverse as their physical properties. To the extent that a generalization can be made, it seems that many of them have experienced SFHs that increase with time, or perhaps are approximately constant with episodic increases in the SFR. There are many examples of LSBGs whose current high specific star formation rates can not have been maintained for a Hubble time.

5.2 Future Work

5.2.1 More Stellar Population

While population models predict that near-infrared bands are a much better tracer of stellar mass than optical bands, it appears that 3.6μm is even better than the K_s-band from the early SINGs results. Therefore, it would be great to have both the K_s-band and Spitzer IRAC 3.6μm-band in order to measure

stellar masses better. I plan to obtain Spitzer IRAC 3.6μm-band images for sample LSBGs with the available K_s-band images. With great sensitivity of IRAC, stellar mass library for LSBGs will expand tremendously and get more accurate.

On the other hand, having only broad-band colors still has its limitation in terms of stellar population study. Carefully designed spectroscopic study should follow up to provide more information on stellar populations on various parts of galaxies, or/and also on HII regions.

5.2.2 Test of Star Formation Laws

The gas content of disk galaxies is as fundamental as their stellar distribution. Stars are formed from gas, and the relative distributions of the two components reflect the history of the conversion of gas into stars. Understanding this evolution through the process of star formation is one of the basic goals of much of the current effort in astronomy.

While of enormous interest, the processes of star formation remain difficult to perceive. Worse, there is a great gulf between the formation of individual stars and star formation on galactic scales. However, there are two simple empirical laws to focus on.

The first is the Schmidt law (Schmidt 1959):

$$\Sigma_{SFR} \quad = \quad A\Sigma_{gas}^{N}, \tag{5.1}$$

and various mechanisms that control star formation in galaxies; gravitational instability, supersonic turbulence, magnetic fields, and rotational shear (Elmegreen

2002; Kennicutt 1989; Larson 2003; Mac Low & Klessen 2004) have been discussed and debated.

The second empirical law is star formation threshold, which also lead into various ideas about what determines the critical density of star formation. Kennicutt (1989) associates the onset of large (∼kpc) scale star formation with regions where the gas surface density exceeds that for stability according to the Toomre Q criterion (Toomre 1964) for gravitational instability. Martin & Kennicutt (2001) confirmed that Kennicutt's critical density is valid using 32 nearby spiral galaxy sample.

However, Wong & Blitz (2002) claimed that the ratio of gas surface density at the threshold to the critical density (α_Q) does not play a role for star formation, but simply is a measurement of gas fraction. Schaye (2004) suggested that the transition to the cold phase leads to gravitational instability and star formation without assuming constant velocity dispersion. Observationally, these ideas can be tested by observation of the gas. While the Kennicutt critical gas density criterion works fairly well in high surface brightness spirals (HSBGs) (Martin & Kennicutt 2001), it still has been tested only on global scales, which means that only density azimuthally averaged over the entire galaxy disc is tested for the criterion. It may not work well in different environments, especially in the inner regions of LSBGs where rotation curves rise slowly. Also, massive star formation rates in LSBGs are an order of magnitude lower than those of HSBGs (van der Hulst et al. 1993b), while these galaxies usually have fairly large gas mass fractions which sometimes approach unity despite their exceptionally low gas surface densities (de Blok et al. 1996). These physical characteristics make LSBGs an excellent testbed to investigate which parameter ignites star formation.

Bibliography

Allen, R. J. & Shu, F. H. 1979, ApJ, 227, 67

Arp, H. 1965, ApJ, 142, 402

Bell, E. F., Barnaby, D., Bower, R. G., de Jong, R. S., Harper, D. A., Hereld, M., Loewenstein, R. F., & Rauscher, B. J. 2000, MNRAS, 312, 470

Bell, E. F., Bower, R. G., de Jong, R. S., Hereld, M., & Rauscher, B. J. 1999, MNRAS, 302, L55

Bell, E. F. & de Jong, R. S. 2000, MNRAS, 312, 497

—. 2001, ApJ, 550, 212

Bell, E. F., McIntosh, D. H., Katz, N., & Weinberg, M. D. 2003, ApJS, 149, 289

Bergmann, M. P., Jørgensen, I., & Hill, G. J. 2003, AJ, 125, 116

Bergvall, N., Rönnback, J., Masegosa, J., & Östlin, G. 1999, A&A, 341, 697

Boissier, S., Monnier Ragaigne, D., Prantzos, N., van Driel, W., Balkowski, C., & O'Neil, K. 2003, MNRAS, 343, 653

Bothun, G., Impey, C., & McGaugh, S. 1997, PASP, 109, 745

Bothun, G. D., Romanishin, W., Strom, S. E., & Strom, K. M. 1984, AJ, 89, 1300

Bottema, R. 1993, A&A, 275, 16

—. 1997, A&A, 328, 517

—. 1999, A&A, 348, 77

Bruzual, A. G. & Charlot, S. 1993, ApJ, 405, 538

Canzian, B. 1993, PASP, 105, 661

Carignan, C., Sancisi, R., & van Albada, T. S. 1988, AJ, 95, 37

Chattopadhyay, T. & Chattopadhyay, A. K. 2006, AJ, 131, 2452

Das, M., O'Neil, K., Vogel, S. N., & McGaugh, S. 2006, ApJ, 651, 853

de Blok, W. J. G. & Bosma, A. 2002, A&A, 385, 816

de Blok, W. J. G. & McGaugh, S. S. 1997, MNRAS, 290, 533

de Blok, W. J. G., McGaugh, S. S., & Rubin, V. C. 2001, AJ, 122, 2396

de Blok, W. J. G., McGaugh, S. S., & van der Hulst, J. M. 1996, MNRAS, 283, 18

de Blok, W. J. G. & van der Hulst, J. M. 1998a, A&A, 335, 421

—. 1998b, A&A, 336, 49

de Blok, W. J. G., van der Hulst, J. M., & Bothun, G. D. 1995, MNRAS, 274, 235

de Jong, R. S. 1996, A&A, 313, 377

de Jong, R. S. & van der Kruit, P. C. 1994, A&AS, 106, 451

de Naray, R. K., McGaugh, S. S., & de Blok, W. J. G. 2004, MNRAS, 355, 887

de Vaucouleurs, G., de Vaucouleurs, A., Corwin, Jr., H. G., Buta, R. J., Paturel, G., & Fouque, P. 1991, Third Reference Catalogue of Bright Galaxies (Volume 1-3, XII, 2069 pp. 7 figs.. Springer-Verlag Berlin Heidelberg New York)

Disney, M. & Phillipps, S. 1983, MNRAS, 205, 1253

Disney, M. J. 1976, Nature, 263, 573

Eder, J. A. & Schombert, J. M. 2000, ApJS, 131, 47

Elmegreen, B. G. 2002, ApJ, 577, 206

Fazio, G. G., Hora, J. L., Allen, L. E., Ashby, M. L. N., Barmby, P., Deutsch, L. K., Huang, J.-S., Kleiner, S., Marengo, M., Megeath, S. T., Melnick, G. J., Pahre, M. A., Patten, B. M., Polizotti, J., Smith, H. A., Taylor, R. S., Wang, Z., Willner, S. P., Hoffmann, W. F., Pipher, J. L., Forrest, W. J., McMurty, C. W., McCreight, C. R., McKelvey, M. E., McMurray, R. E., Koch, D. G., Moseley, S. H., Arendt, R. G., Mentzell, J. E., Marx, C. T., Losch, P., Mayman, P., Eichhorn, W., Krebs, D., Jhabvala, M., Gezari, D. Y., Fixsen, D. J., Flores, J., Shakoorzadeh, K., Jungo, R., Hakun, C., Workman, L., Karpati, G., Kichak, R., Whitley, R., Mann, S., Tollestrup, E. V., Eisenhardt, P., Stern, D., Gorjian, V., Bhattacharya, B., Carey, S., Nelson, B. O., Glaccum, W. J., Lacy, M., Lowrance, P. J., Laine, S., Reach, W. T., Stauffer, J. A., Surace, J. A., Wilson, G., Wright, E. L., Hoffman, A., Domingo, G., & Cohen, M. 2004, ApJS, 154, 10

Fish, R. A. 1964, ApJ, 139, 284

Freeman, K. C. 1970, ApJ, 160, 811

Galaz, G., Dalcanton, J. J., Infante, L., & Treister, E. 2002, AJ, 124, 1360

Gerritsen, J. P. E. & de Blok, W. J. G. 1999, A&A, 342, 655

Hayes, D. S. & Latham, D. W. 1975, ApJ, 197, 593

Helmboldt, J. F., Walterbos, R. A. M., Bothun, G. D., O'Neil, K., & de Blok, W. J. G. 2004, ApJ, 613, 914

Hinz, J. L., Rieke, M. J., Rieke, G. H., Willmer, C. N. A., Misselt, K., Engelbracht, C. W., Blaylock, M., & Pickering, T. E. 2007, ApJ, 663, 895

Hunter, D. A. & Elmegreen, B. G. 2006, ApJS, 162, 49

Impey, C., Burkholder, V., & Sprayberry, D. 2001, AJ, 122, 2341

Impey, C. D., Sprayberry, D., Irwin, M. J., & Bothun, G. D. 1996, ApJS, 105, 209

Jansen, R. A., Fabricant, D., Franx, M., & Caldwell, N. 2000, ApJS, 126, 331

Kennicutt, Jr., R. C. 1983, ApJ, 272, 54

—. 1989, ApJ, 344, 685

Kennicutt, Jr., R. C., Edgar, B. K., & Hodge, P. W. 1989, ApJ, 337, 761

Kennicutt, Jr., R. C., Tamblyn, P., & Congdon, C. E. 1994, ApJ, 435, 22

Kroupa, P., Tout, C. A., & Gilmore, G. 1993, MNRAS, 262, 545

Landolt, A. U. 1992, AJ, 104, 340

Larson, R. B. 2003, Reports of Progress in Physics, 66, 1651

Lauberts, A. & Valentijn, E. A. 1989, The surface photometry catalogue of the ESO-Uppsala galaxies (Garching: European Southern Observatory, —c1989)

Mac Low, M.-M. & Klessen, R. S. 2004, Reviews of Modern Physics, 76, 125

MacArthur, L. A., Courteau, S., & Holtzman, J. A. 2003, ApJ, 582, 689

Martin, C. L. & Kennicutt, Jr., R. C. 2001, ApJ, 555, 301

Massey, P., Strobel, K., Barnes, J. V., & Anderson, E. 1988, ApJ, 328, 315

Matthews, L. D., Gao, Y., Uson, J. M., & Combes, F. 2005, AJ, 129, 1849

Matthews, L. D., van Driel, W., & Monnier-Ragaigne, D. 2001, A&A, 365, 1

McGaugh, S. S. 1992, PhD thesis, AA(Michigan Univ., Ann Arbor.)

—. 1994, ApJ, 426, 135

—. 2005, ApJ, 632, 859

McGaugh, S. S. & Bothun, G. D. 1994, AJ, 107, 530

McGaugh, S. S., Bothun, G. D., & Schombert, J. M. 1995a, AJ, 110, 573

McGaugh, S. S. & de Blok, W. J. G. 1997, ApJ, 481, 689

McGaugh, S. S., Rubin, V. C., & de Blok, W. J. G. 2001, AJ, 122, 2381

McGaugh, S. S., Schombert, J. M., & Bothun, G. D. 1995b, AJ, 109, 2019

McKee, C. F. & Williams, J. P. 1997, ApJ, 476, 144

Mihos, J. C., Spaans, M., & McGaugh, S. S. 1999, ApJ, 515, 89

Nagamine, K., Cen, R., & Ostriker, J. P. 2000, ApJ, 541, 25

Nilson, P. 1973, Nova Acta Regiae Soc. Sci. Upsaliensis Ser. V, 0

Oey, M. S. & Clarke, C. J. 1998, AJ, 115, 1543

Oke, J. B. 1974, ApJS, 27, 21

O'Neil, K., Bothun, G., van Driel, W., & Monnier Ragaigne, D. 2004, A&A, 428, 823

O'Neil, K., Bothun, G. D., & Schombert, J. 1998, AJ, 116, 2776

O'Neil, K., Bothun, G. D., Schombert, J., Cornell, M. E., & Impey, C. D. 1997, AJ, 114, 2448

O'Neil, K., Oey, M. S., & Bothun, G. 2007a, AJ, 134, 547

—. 2007b, AJ, 134, 547

Peletier, R. F., Valentijn, E. A., Moorwood, A. F. M., & Freudling, W. 1994, A&AS, 108, 621

Persson, S. E., Murphy, D. C., Krzeminski, W., Roth, M., & Rieke, M. J. 1998, AJ, 116, 2475

Phillipps, S. & Disney, M. 1985, MNRAS, 217, 435

Pildis, R. A., Schombert, J. M., & Eder, J. A. 1997, ApJ, 481, 157

Portinari, L., Sommer-Larsen, J., & Tantalo, R. 2004, MNRAS, 347, 691

Rahman, N., Howell, J. H., Helou, G., Mazzarella, J. M., & Buckalew, B. 2007, ApJ, 663, 908

Rand, R. J. 1992, AJ, 103, 815

Rieke, G. H., Young, E. T., Engelbracht, C. W., Kelly, D. M., Low, F. J.,

Haller, E. E., Beeman, J. W., Gordon, K. D., Stansberry, J. A., Misselt, K. A., Cadien, J., Morrison, J. E., Rivlis, G., Latter, W. B., Noriega-Crespo, A., Padgett, D. L., Stapelfeldt, K. R., Hines, D. C., Egami, E., Muzerolle, J., Alonso-Herrero, A., Blaylock, M., Dole, H., Hinz, J. L., Le Floc'h, E., Papovich, C., Pérez-González, P. G., Smith, P. S., Su, K. Y. L., Bennett, L., Frayer, D. T., Henderson, D., Lu, N., Masci, F., Pesenson, M., Rebull, L., Rho, J., Keene, J., Stolovy, S., Wachter, S., Wheaton, W., Werner, M. W., & Richards, P. L. 2004, ApJS, 154, 25

Romanishin, W., Krumm, N., Salpeter, E., Knapp, G., Strom, K. M., & Strom, S. E. 1982, ApJ, 263, 94

Salpeter, E. E. 1955, ApJ, 121, 161

Salzer, J. J., di Serego Alighieri, S., Matteucci, F., Giovanelli, R., & Haynes, M. P. 1991, AJ, 101, 1258

Schaye, J. 2004, ApJ, 609, 667

Schlegel, D. J., Finkbeiner, D. P., & Davis, M. 1998, ApJ, 500, 525

Schmidt, M. 1959, ApJ, 129, 243

Schmitt, H. R., Calzetti, D., Armus, L., Giavalisco, M., Heckman, T. M., Kennicutt, Jr., R. C., Leitherer, C., & Meurer, G. R. 2006, ApJS, 164, 52

Schombert, J. 2007, ARCHANGEL Galaxy Photometry System

Schombert, J. M. & Bothun, G. D. 1988, AJ, 95, 1389

Schombert, J. M., Bothun, G. D., Impey, C. D., & Mundy, L. G. 1990, AJ, 100, 1523

Schombert, J. M., Bothun, G. D., Schneider, S. E., & McGaugh, S. S. 1992, AJ, 103, 1107

Schombert, J. M., McGaugh, S. S., & Eder, J. A. 2001, AJ, 121, 2420

Schombert, J. M., Pildis, R. A., & Eder, J. A. 1997, ApJS, 111, 233

Skrutskie, M. F., Schneider, S. E., Stiening, R., Strom, S. E., Weinberg, M. D., Beichman, C., Chester, T., Cutri, R., Lonsdale, C., Elias, J., Elston, R., Capps, R., Carpenter, J., Huchra, J., Liebert, J., Monet, D., Price, S., & Seitzer, P. F. Garzon, N. EpchteinA. OmontB. Burton & P. Persi, 25–+

Sprayberry, D., Impey, C. D., Bothun, G. D., & Irwin, M. J. 1995, AJ, 109, 558

Stone, R. P. S. 1996, ApJS, 107, 423

Swaters, R. A., Madore, B. F., & van den Bosch, F. C. andBalcells, M. 2003, ApJ, 583, 732

Swaters, R. A., van Albada, T. S., van der Hulst, J. M., & Sancisi, R. 2002, A&A, 390, 829

Toomre, A. 1964, ApJ, 139, 1217

Tully, R. B., Verheijen, M. A. W., Pierce, M. J., Huang, J.-S., & Wainscoat, R. J. 1996, AJ, 112, 2471

van den Hoek, L. B., de Blok, W. J. G., van der Hulst, J. M., & de Jong, T. 2000, A&A, 357, 397

van der Hulst, J. M., Skillman, E. D., Smith, T. R., Bothun, G. D., McGaugh, S. S., & de Blok, W. J. G. 1993a, AJ, 106, 548

—. 1993b, AJ, 106, 548

van Zee, L. 2001, AJ, 121, 2003

van Zee, L., Haynes, M. P., & Salzer, J. J. 1997a, AJ, 114, 2497

—. 1997b, AJ, 114, 2479

Walterbos, R. A. M. & Braun, R. 1992, A&AS, 92, 625

Wong, T. & Blitz, L. 2002, ApJ, 569, 157

Worthey, G. 1994, ApJS, 95, 107

York, D. G., Adelman, J., Anderson, Jr., J. E., Anderson, S. F., Annis, J.,

Bahcall, N. A., Bakken, J. A., Barkhouser, R., Bastian, S., Berman, E., Boroski, W. N., Bracker, S., Briegel, C., Briggs, J. W., Brinkmann, J., Brunner, R., Burles, S., Carey, L., Carr, M. A., Castander, F. J., Chen, B., Colestock, P. L., Connolly, A. J., Crocker, J. H., Csabai, I., Czarapata, P. C., Davis, J. E., Doi, M., Dombeck, T., Eisenstein, D., Ellman, N., Elms, B. R., Evans, M. L., Fan, X., Federwitz, G. R., Fiscelli, L., Friedman, S., Frieman, J. A., Fukugita, M., Gillespie, B., Gunn, J. E., Gurbani, V. K., de Haas, E., Haldeman, M., Harris, F. H., Hayes, J., Heckman, T. M., Hennessy, G. S., Hindsley, R. B., Holm, S., Holmgren, D. J., Huang, C.-h., Hull, C., Husby, D., Ichikawa, S.-I., Ichikawa, T., Ivezić, Ž., Kent, S., Kim, R. S. J., Kinney, E., Klaene, M., Kleinman, A. N., Kleinman, S., Knapp, G. R., Korienek, J., Kron, R. G., Kunszt, P. Z., Lamb, D. Q., Lee, B., Leger, R. F., Limmongkol, S., Lindenmeyer, C., Long, D. C., Loomis, C., Loveday, J., Lucinio, R., Lupton, R. H., MacKinnon, B., Mannery, E. J., Mantsch, P. M., Margon, B., McGehee, P., McKay, T. A., Meiksin, A., Merelli, A., Monet, D. G., Munn, J. A., Narayanan, V. K., Nash, T., Neilsen, E., Neswold, R., Newberg, H. J., Nichol, R. C., Nicinski, T., Nonino, M., Okada, N., Okamura, S., Ostriker, J. P., Owen, R., Pauls, A. G., Peoples, J., Peterson, R. L., Petravick, D., Pier, J. R., Pope, A., Pordes, R., Prosapio, A., Rechenmacher, R., Quinn, T. R., Richards, G. T., Richmond, M. W., Rivetta, C. H., Rockosi, C. M., Ruthmansdorfer, K., Sandford, D., Schlegel, D. J., Schneider, D. P., Sekiguchi, M., Sergey, G., Shimasaku, K., Siegmund, W. A., Smee, S., Smith, J. A., Snedden, S., Stone, R., Stoughton, C., Strauss, M. A., Stubbs, C., SubbaRao, M., Szalay, A. S., Szapudi, I., Szokoly, G. P., Thakar, A. R., Tremonti, C., Tucker, D. L., Uomoto, A., Vanden Berk, D., Vogeley, M. S., Waddell, P., Wang, S.-i., Watanabe, M.,

Weinberg, D. H., Yanny, B., & Yasuda, N. 2000, AJ, 120, 1579

Zackrisson, E., Bergvall, N., & Östlin, G. 2005, A&A, 435, 29

Zwicky, F. 1957, Morphological astronomy (Berlin: Springer, 1957)